Transformation-Superplasticity of Metals and Metal Matrix Composites

by

Peter Zwigl

M.S. Physics
Innsbruck University, 1992

SUBMITTED TO THE DEPARTMENT OF MATERIALS SCIENCE AND ENGINEERING IN PARTIAL FULFILLMENT OF THE REQUIREMENTS FOR THE DEGREE OF

DOCTOR OF PHILOSOPHY
AT THE
MASSACHUSETTS INSTITUTE OF TECHNOLOGY

FEBRUARY, 1998
[June 1998]

Signature of Author_____
Department of Materials Science and Engineering
January 9, 1998

Certified by_____
David C. Dunand
AMAX Associate Professor of Materials Engineering
Thesis Supervisor

Accepted by_____
Linn W. Hobbs
John F. Elliott Professor of Materials
Chairman, Departmental Committee on Graduate Students

Transformation-Superplasticity of Metals and Metal Matrix Composites

by

Peter Zwigl

Submitted to the Department of Materials Science and Engineering
on January 9, 1998 in Partial Fulfillment of the Requirements for the
Degree of Doctor of Philosophy in Materials Engineering

ABSTRACT

The work covers transformation superplasticity of metals, alloys and metal matrix composites. Fundamental studies of transformation superplasticity in unreinforced metals, which either deform plastically or by creep, form the basis of further investigations in metal matrix composites. Experiments and analytical modeling are complemented by numerical analysis. The transformation superplastic behavior is related to microstructure and chemical composition. Based on an existing linear theory, a non-linear model is developed and applied to the experimental data. Numerical methods are used to model the stress-, strain- and temperature evolution during the phase transformation. The results are in good agreement with the experiment and analytical predictions.

First, transformation superplasticity of iron and iron-TiC composites is demonstrated with strains of 450% and 230% respectively. The reduction of the transformation superplasticity in the composites is attributed to the dissolution of TiC in iron and effect which is shown for iron-carbon alloys. Effects of transient primary creep, ratchetting and partial transformation through the ferrite-austenite phase field are examined. Second, transformation superplasticity of zirconium is demonstrated for the first time with a strain of 270% without fracture. Partial transformation resulting from high cycle frequencies is analyzed and related to material properties and cycle characteristics. Finally, nickel aluminide with unstabilized zirconia particulates shows significant higher strain rates upon thermal cycling as compared to the unreinforced matrix. Although, the fracture strain of 23% is below the superplastic limit , the composite shows a high strain rate sensitivity of m = 0.71, which is a necessary characteristic of transformation superplasticity.

Thesis Supervisor: David C. Dunand
Title: AMAX Associate Professor of Materials Engineering

Table of Contents

List of Figures

List of Tables

Acknowledgments

I want to acknowledge:

- Dr. W.C. Simmons from the US Army Research Office for the support of this research,
- Dr. John Haygarth and Mr. Paul Danielson from Wah Chang (Albany, OR) for supplying and analyzing zirconium samples,
- the following organizations for their financial support:
  - Austrian Government
  - Austrian Chamber of Commerce
  - Landesgedächtnisstiftung des Landes Tirol
  - Eduard Wallnöfer Stiftung
  - Kammer für Arbeiter und Angestellte Zweig Innsbruck,
- the computer center of Innsbruck University on which workstations the numerical calculations were performed.

I also wish to thank:

- The technical staff at MIT
  Fred Wilson - who knows where to go and whom to ask
  Pat Kearny - for the good cutting wheels
  Yin-Lin Xie - who taught me patience during polishing
  Günther Arndt - a sketch on a paper towel - that's all he needs,
- the computer experts
  Peter Ragone (MIT) - he also knows how to use short skis
  Billi Lehar (Innsbruck University)
  - the office where the light is always on,
- the support and administrative staff at MIT, especially
  Jamie Sieger - who can get a P.O. number even on Friday afternoon
  Stacey Rochford - you are welcome
  Gloria Landhal - what can I do for you?
  Ann Jacoby - the first person I talked to at MIT
  Nancy Herron - where are my room keys?
  Bonnie Barber - for the 48 departmental newsletters,
- the Northwestern group
  Christopher Schuh - sleep is unacceptable
  Jeffrey Grabowski - who has it's own interpretation of rock and roll
  Bingqiang Han - no, I am not from Australia,
- the MIT group
  Kohta Ueno - the first engineer of "the machine"
  Shinya Myoin - hello form the rubber seals
  T.A. Venkatesh, Rajan Vadjanathan, Michael Whitney, Ann Jensen, Christian Lund and the post-docs - one more student and we declare the group meeting a conference.

Special thanks to my advisor, Prof. David C. Dunand, who did not give up to convince me to pursue a Ph.D. degree and showed me how to do good science.

I want to thank: - my mother and my sisters for their help especially when it came to food and moving; - my friends in Austria, who challenged my physical condition every time I came home;

Finally, I am grateful to my fiancée, Eveline Metzler, and that our companionship survived MIT.

Introduction

Transformation superplasticity is a deformation mechanism independent of grain size, where large strains are accumulated by superimposing an external stress to internal mismatch stresses that are reproduced by thermal cycling of a polycrystalline allotropic material about its phase transformation temperature. The internal stresses are biased by the external stress and accommodated in the weaker phase by a time-dependent or -independent plastic mechanism.

The above modern definition of transformation superplasticity (for comprehensive reviews, see Refs. [25,60,68]) has evolved from its original discovery, usually credited to Lee [51] and Sauveur [82] who reported in 1923-24 "critical plasticity" when iron or steel undergoes a phase transformation. In 1919, Tiemann [91] had mentioned a related phenomenon but did not perform a systematic study or give a scientific explanation for the phenomenon.

Later, transformation superplasticity research extended to iron-nickel alloys [83,98,99] and iron-carbon alloys [17,19,20]. Driven mainly by research on uranium, additional deformation mechanisms based on internal stress phenomena were recognized: first, irradiation swelling caused by neutron irradiation of α-uranium [77]; second, ratchetting where macroscopic thermal gradients cause plastic deformation [86]; and third, coefficient of thermal expansion mismatch plasticity caused by anisotropic coefficients of thermal expansion in α-uranium [47,103]. Based on the models developed in these fields, Greenwood and Johnson [39] proposed for phase transformation plasticity a theory (which is now well accepted) based on experimental data of U, Co, Ti, Fe and Zr [39]. Subsequent research focused mostly on steels [34,35,44,45,61,63-65,69,102] and, to a lesser extent, on titanium [9,14,26,32,88] and titanium based alloys [28,59]. Parallel to the research on

phase transformation superplasticity in steels another similar field emerged termed transformation induced plasticity (TRIP) were anisotropic strains due to the formation of martensite are a source of the mismatch and also directly contribute to macroscopic deformation [22,66,74,83,87].

In the last decade, internal stress superplasticity has been demonstrated in metal matrix composites. Using coefficient of thermal expansion mismatch between a matrix and a reinforcement, González-Doncel et. al. [38], Pickard and Derby [70,71] and Chen et. al. [15] investigated Al/SiC composites. In a similar mechanism, Huang and Daehn [42] deformed Al/SiC composites using the compressibility mismatch plasticity between matrix and reinforcement. Recently, Dunand and Bedell [9,26] studied phase transformation superplasticity in Ti-TiC composites.

Beside metals, transformation superplasticity has also been of interest in geophysical research (olivine [73]) and ceramic research (bismuth oxides [46] and zirconia [40]).

Modeling within each field of internal stress (super)plasticity is mutually applicable as the common source of the internal stress is always an internal mismatch. Table 2.1 gives examples specific to each type of mismatch (U [54], Zn [72]; Fe [17,20,39,69], Zr [39], ZrO_2 [40]; Al/SiC [15,71]; Ti/TiC [26]). Some materials show an overlap of mechanisms e.g. U and Zr are allotropic and show coefficient of thermal expansion anisotropy.

		Source of Mismatch	
		Coefficient of Thermal Expansion	Phase Transformation
Mismatching Constituents	Grains	Anisotropy U, Zn	Fe, Zr, ZrO_2
	Phases	Al/SiC	Ti/TiC NiAl/ZrO_2

Table 1: Overview of the internal stress superplastic systems.

Analytical models of phase transformation plasticity of single constituent materials are based either on continuum mechanics, using a yield criteria [39,69] or a creep law [39], or on dislocation theories [35,50,73]. Continuum mechanics is also used in the modeling of single phase and composite CTE-mismatch superplasticity, as reviewed in Ref. [27]. The modeling of phase transformation superplasticity of composites is based on (i) models of transformation superplasticity of the transforming constituent, (ii) models of coefficient of thermal expansion mismatch and the volumetric mismatch between the constituents and (iii) models of the volume fraction effect. For example, Dunand and Bedell [26] used the model by Greenwood and Johnson [39] to describe a transforming titanium matrix, together with a general model for internal stress plasticity by Sato and Kuribayashi [81], which also includes the volume fraction dependence, to incorporate the mismatch between the titanium matrix and TiC particulates.

Numerical modeling has been used mostly to describe Al/SiC composites during expansion mismatch superplasticity [105,106] and to describe transformation induced plasticity in steels [21,33,35,52,76]. However, transformation superplasticity caused by a homogeneous volumetric mismatch in either single phase or composite systems has not been numerically modeled.

Beside the scientific interest of understanding transformation superplasticity as a deformation mechanism, there is a strong technological incentive for using this phenomenon to shape metal matrix composites where traditional forming techniques, such as stamping or forging, are limited or even impossible due to the brittleness of the reinforcement or of the matrix. Furthermore, the grain-size insensitivity is also of interest for pure metals and some alloys which cannot be deformed by fine-grain superplasticity because, at the deformation temperature, their grains cannot be stabilized to the very small sizes necessary for grain-boundary sliding. However, as an emerging technology, little is known about the factors

which control transformation superplasticity in composites and even in pure metals, unlike the much better explored fine grain superplasticity.

This thesis is divided in modular chapters designed as independent studies and structured to cover a specific material or theoretical topic. While this approach results in some repetitions (in particular in the respective introductions and in some of the equations), it has the advantage of giving a focused and self-contained description.

Chapter 1 presents and experimental study of transformation superplasticity of iron and Fe/TiC composites. Iron, because of its stronger high temperature phase (austenite), shows accommodation by yield of the weaker low temperature phase (ferrite). The effect of partial transformation through the α/γ-phase field, primary creep, ratchetting and the presence of carbon are investigated and transformation superplasticity of iron and iron with 10 vol.% TiC is demonstrated.

In Chapter 2, the model of Greenwood and Johnson [39] is extended to high stresses where the stress-strain behavior becomes non-linear. The new model is applied to literature data for pure iron [17,39] and, after incorporating a strain hardening criteria, it is also applied to iron with traces of carbon investigated in Chapter 1. In addition, the non-linear theory is used to model two mechanisms of thermal expansion mismatch superplasticity found in pure metals and composites.

A numerical method is used in Chapter 3 to model transformation superplasticity of pure iron. By linking the mechanical to the thermal problem, the strain-, stress-, and temperature history of the phase transformation is obtained. Model-specific quantities are introduced which allow a quantitative comparison to the analytical predictions of Chapter 2 and literature results for pure iron.

The correlation between the thermal- and mechanical problem is used in Chapter 4 to investigate transformation superplasticity of pure zirconium. In contrast to iron,

accommodation of the internal phase transformation stresses is by creep of the high temperature β-zirconium phase. The average internal stress during the phase transformation is related to the time for transformation and the creep law of the weaker phase. For the first time, transformation superplasticity is demonstrated for zirconium for which a strain in excess of 270% is measured.

Chapter 5 explores the novel case of transformation superplasticity in a composite where the particles (ZrO_2) transform in an inert, non-allotropic matrix (NiAl). The strain rates due to thermal cycling are compared to that of unreinforced NiAl. The internal stress during the phase transformation is calculated and compared to experimental results.

In Chapter 6, transformation superplastic behavior of the NiAl/ZrO_2 composites described in Chapter 5 is analyzed numerically using a transient temperature-displacement model. The thermal problem defines the time scale of the transformation over which the internal strains and stresses develop as the particle deforms. Temperature- and strain histories as well as the spatial stress distributions are computed and compared to analytical predictions.

In the final conclusions, the major results are summarized and a synthetic overview of the connection between the different chapters is given.

In summary, this thesis is a systematic study of transformation superplasticity of metals and metal matrix composites, where both scientific and technological issues are addressed. The measurement of mechanical characteristics (such as total strains, strain to fracture, and strain rates) form the basis for predictive models based on both analytical and numerical techniques. Furthermore, the experimental results are correlated to the microstructure and composition.

Chapter 1

Transformation Superplasticity of Iron and Fe/TiC Metal Matrix Composites

Abstract

Unreinforced iron was thermally cycled around the α/γ-phase field under an externally-applied uniaxial tensile stress, resulting in strain increments which could be accumulated upon repeated cycling to a total strain of 450% without failure. In agreement with existing theory attributing transformation superplasticity to the biasing of the internal allotropic strains by the external stress, the measured strain increments were proportional to the applied stress at small stresses. However, for applied stresses higher than the nominal yield stress, strain increments increased non-linearly with stress, as a result of strain hardening due to dissolved carbon and iron oxide dispersoids. Also, the effects of transient primary creep and ratchetting on the superplastic strain increment values were examined. Finally, partial cycling within the α/γ-phase field indicated an asymmetry in the superplastic strain behavior with respect to the temperature cycling range, which is attributed to the different strengths of ferrite and austenite.

Transformation superplasticity was demonstrated in iron-matrix composites containing 10 vol.% and 20 vol.% TiC particles: strain increments proportional to the applied stress were measured and a fracture strain of 230% was reached for Fe/10TiC. However, the strain increments decreased with increasing TiC content, a result attributed to the slight dissolution of TiC particles within the matrix which raised the matrix yield stress by solid solution strengthening and by reducing the transformation temperature range.

1.1 Introduction

The addition to iron or steel of reinforcing ceramic particulates leads to composites with improved strength, stiffness and abrasion resistance. Titanium carbide (TiC) is particularly attractive, because of its high hardness and stiffness, its low density and its chemical stability with iron-based matrices [24,75]. However, the low ductility, low toughness and high hardness of Fe/TiC composites severely limit traditional forming techniques such as bending, stamping, rolling, forging or machining. Superplastic forming is thus an attractive method to fabricate objects with intricate shapes from simple composite sheets or tubes which can be produced for Fe/TiC by a near-net shape technique such as casting [49,90] or powder metallurgy [48,79]. Microstructural superplasticity is however very difficult to achieve in Fe/TiC composites, because these materials are too brittle for the thermomechanical treatment necessary to generate a fine grain size, and because ceramic reinforcement can inhibit grain boundary sliding. An alternative superplastic deformation mechanism not necessitating a fine-grain structure is transformation superplasticity which relies on internal stresses produced by repeated allotropic transformations [29,68].

Plasticity induced by a phase transformation has been extensively studied in unreinforced iron and steels, and can result from two distinct mechanisms: (i) preferential selection by the applied stress of martensite variants with a non-zero shear [22,66,74,83,87], or (ii) biasing by the applied stress of isotropic internal stresses due to the volumetric mismatch between allotropic phases during the transformation [29,39,68]. For the latter mechanism, these internal mismatch stresses are generated at each crossing of the allotropic range, so that strain increments can be accumulated after each cycle, eventually resulting in superplastic elongations (>100%) [44,64,65]. Depending on the material properties and the phase transformation homologous temperature, the internal transformation mismatch stresses can be relaxed by time-independent plastic deformation or by creep [39]. For the former case, Greenwood and Johnson [39] developed an equation for the uniaxial strain increment $\Delta\varepsilon$

accumulated after a full allotropic transformation occurring with a superimposed uniaxial biasing tensile stress σ:

$$\Delta\varepsilon = \frac{5}{6}\left|\frac{\Delta V}{V}\right|\frac{\sigma}{\sigma_Y} \qquad (1.1)$$

where $|\Delta V/V|$ is the volume mismatch between the allotropic phases and σ_Y is the yield stress of the weaker allotropic phase. Eq. 1.1 is valid for small strains only ($\Delta\varepsilon << |\Delta V/V|$) and for an ideally plastic material without strain-hardening.

While transformation superplasticity has been studied in iron and steels (and many other allotropic metals [29,39,68]), little is known about this phenomenon in metal matrix composites. Transformation superplasticity was recently demonstrated in allotropic titanium-based composites [26,28] where accommodation of internal stresses is by creep, but has never been studied in composites, such as Fe/TiC, where accommodation is by time-independent yield.

In the present chapter, we investigate transformation superplasticity of unreinforced iron and Fe/TiC composites upon thermal cycling about the α/γ-iron phase field, and examine the effect of TiC volume fraction, applied stress, as well as the temperature cycling amplitude and frequency. The superplastic behavior is demonstrated by experiments conducted up to large strains and special emphasis is put on the link between transformation superplasticity and the thermal and microstructural characteristics of the materials.

1.2 Materials and Experimental Procedures

Iron powders with a particle size of 6-10 micron and a purity of 99.5% (from Alfa Aesar, Ward Hill, MA) were mixed for 12 hours in a V-Blender with 10 vol.% and 20 vol.% of 99.5% pure TiC powders (from CERAC, Milwaukee, WI). Before blending, the as-received -325 mesh TiC had been suspended in deionized water and filtered through a

Buchner filtering funnel with a porosity of 10-20 μm to eliminate the fine particles, ensuring a final TiC size distribution between 20 μm and 45 μm. Both unblended iron powders and blended Fe/TiC powder mixtures were cold-pressed into low-carbon steel pipes (ASM 5050J steel with 25.4 mm outside diameter, 3.2 mm wall thickness and 228 mm height, welded at both ends with 1018 steel plugs), degassed under vacuum at elevated temperature, and compacted by hot isostatic pressing (HIP) for 4 hours at 1121°C under a pressure of 103 MPa (at UltraClad Andover MA).

Small samples were tested by differential thermal analysis (DTA, Perkin Elmer, Series 7) at a rate $\dot{T}$ = 10 K·min^{-1} under flowing nitrogen with alumina as reference material. Parallelepiped samples (approximately 12 mm × 3 mm × 3 mm) were studied by dilatometry (Netzsch 402 ES) with $\dot{T}$ = 10 K·min^{-1} under flowing argon. Dogbone samples with a gauge length of 35 mm and a gauge diameter of 6 mm were tested in tension in a custom designed creep apparatus allowing the application of small tensile stresses with a simultaneous rapid temperature cycling by radiant heating in an argon atmosphere. Before thermal cycling, the samples were crept isothermally until a steady-state strain-rate was reached. The deformation was measured by a linear voltage displacement transducer placed at the cold end of the lower pullrod. Under cycling conditions, the measured deformation included the thermal dilatation of the pullrods and samples and therefore did not represent the sample plastic strain. However, the strain measured under isothermal conditions or after a full temperature cycle was only due to the sample plastic deformation. The total plastic strain increment per cycle, $\Delta\varepsilon_{tot}$, was calculated as the average of 4 to 6 cycles strain values after the strain increments had reached steady-state to avoid any primary creep strain contribution. The sample stress was adjusted manually by periodically applying or removing weights. Standard deviations for stress and strain were below 5%. The temperature of the sample was controlled within ±2°C by a thermocouple (K-type or R-type) positioned at the surface of the gauge section or the pullhead and independently measured by

a second thermocouple located at the sample surface. The latter temperature varied ±15°C among different experiments due to slight variations in sample and/or thermocouple position with respect to the radiant heaters.

Densities were determined by the Archimedes method with distilled water. Metallographic preparation of undeformed and deformed samples was performed by grinding with SiC papers with 120, 500, 1200, 2400 mesh, polishing on cloths with 0.3 μm and 0.05 μm alumina and etching by swabbing for 20 seconds with a 2% Nital solution.

1.3 Results

1.3.1 Materials

Table 1.2 gives the chemical analysis of the as-received powders and the HIPed iron sample. The measured carbon content of the as-received TiC powders is close to the theoretical concentration for TiC with the highest possible carbon content (19.3 wt.% C or 48.8 at.% C)[6], indicating that the as-received TiC powder was as close to stoichiometry as thermodynamically possible. Slight carbon contamination of the iron billet (and thus most probably the composite billets) occurred during HIPing by diffusion of carbon and other alloying elements from the steel can.

Assuming that the oxygen present in the iron matrix exists in the form of iron oxides (Fe_3O_4 or Fe_2O_3) and using density values given in Ref. [53], the theoretical density of the unreinforced matrix is determined as $\rho_{matrix} = 7.83\ g \cdot cm^{-3}$, indicating that the iron sample is 99.8% dense (Table 1.3). With the theoretical density of TiC as $\rho_{TiC} = 4.92\ g \cdot cm^{-3}$ [92], similarly low porosities are calculated for the composites after HIPing and after deformation (Table 1.3).

Figures 1.1a-c and Figs. 1.1d-f show micrographs of the HIPed samples in unetched and etched conditions, respectively. The iron sample exhibits both oxides and pores (Fig.

1.1a). The unetched micrographs of the composites (Figs. 1.1b,c) show that the TiC particles are well distributed within a dense matrix. However, etching reveals other precipitates at the grain boundaries (Figs. 1.1e,f). The grain size of the iron samples, as determined by the linear intercept method, increased from 34 ± 4 μm after hot isostatic pressing (Fig. 1.1d) to 62 ± 8 μm at the pullhead and 340 ± 70 μm (Fig. 1.1g) at the gauge section after thermal cycling under stress. On the other hand, the grain size of the Fe/10TiC composite remained stable with values of 30 ± 3 μm after hot isostatic pressing (Fig. 1.1e) and 23 ± 4 μm after thermal cycling (Fig. 1.1h). Similar grain sizes were obtained for the Fe/20TiC composite (Fig. 1.1f,i). Furthermore, the same grain sizes were found in the sample heads and gauge section of the deformed composites.

The DTA curve (Fig. 1.2) and dilatometric curve (Fig. 1.3) exhibit multiple peaks corresponding to phase transformation and precipitation labeled in both figures with the same symbols.

1.3.2 Thermal Cycling of Iron

Figure 1.4 shows the total strain increment $\Delta\varepsilon_{tot}$ as a function of the applied stress σ for complete square-wave cycles between $T_l = 700°C$ and $T_u = 900°C$, with heating and cooling rates in the range $\dot{T} = 100 - 200\ K \cdot min^{-1}$ and for cycling frequencies in the range $\nu = 6 - 15\ hr^{-1}$. The data is insensitive to the cycle frequency within the experimental range used, as seen from the continuity of the results in Fig. 1.4. The strain increment increases linearly with the applied stress up to $\sigma \approx 6$ MPa and becomes non-linear for higher stresses. Within the linear range, a slope $(d\Delta\varepsilon_{tot})/d\sigma = 1.7\ GPa^{-1}$ and an intercept $\Delta\varepsilon_{tot} = -0.05\%$ for zero applied stress are found. Isothermal creep measurements were performed at the upper and lower cycling temperature before and after thermal cycling, giving stress exponents between 1 and 2. For all experiments, it was found that the isothermal strain rates caused by creep were negligible compared to the cycling strain rates. For example, at the upper cycling

temperature, the iron sample crept at $\dot{\varepsilon} = 3.3 \cdot 10^{-7}$ s^{-1} for a stress $\sigma = 4.2$ MPa, much more slowly than under cycling conditions with $\nu = 6$ hr^{-1} where the average strain rate was $d(\Delta\varepsilon_{tot})/dt = 1.3 \cdot 10^{-5}$ s^{-1} for $\sigma = 4.6$ MPa. For a higher applied stress $\sigma = 10.3$ MPa, the isothermal creep strain rate $\dot{\varepsilon} = 2 \cdot 10^{-6}$ s^{-1} was still much smaller than the average cycle strain rate $d(\Delta\varepsilon_{tot})/dt = 8.8 \cdot 10^{-5}$ s^{-1} (for frequency $\nu = 15$ hr^{-1}). In several instances the isothermal creep rates dropped after thermal cycling by factors between 2 and 5. Creep rates at the lower cycling temperature were not detectable.

Figure 1.5 shows two examples of the displacement measured over a full cycle for applied stresses of 5.2 MPa and 10.1 MPa. For these cycling conditions and sample geometry, the total strain increment per cycle is composed of equal contributions on heating and on cooling. Also visible in Fig. 1.5 are discontinuities on heating and cooling, corresponding to the phase transformations. During heating the sample superplastic strain and the thermal expansion of the load-train give contributions in the same direction, causing a discontinuity at the phase transformation temperature, whereas during cooling, the thermal contraction of the load-train opposes the sample elongation due to the superplastic strain increment, leading to a distinct phase transformation peak.

The effect of upper and lower temperature cycle amplitude on the stress-normalized strain increment $\Delta\varepsilon_{tot}/\sigma$ is shown in Fig. 1.6 for two stress levels. While keeping the lower temperature constant at $T_l = 710$°C, the upper cycle temperature was gradually increased up to $T_u = 930$°C; the symmetric experiments (constant upper temperature $T_u = 930$°C and variable lower temperature T_l) were also performed.

Finally, Fig. 1.7a shows an unfractured iron sample deformed to an engineering strain of $e_3 = 454\%$ after 242 cycles ($T_l = 700$°C, $T_u = 900$°C, $\nu = 15$ hr^{-1}) under an applied stress $\sigma = 7.2 \pm 0.2$ MPa for the first 140 cycles and a stress $\sigma = 4.9 \pm 0.3$ MPa for the last 102 cycles. Figure 1.8 shows for that sample the stress normalized strain increment per cycle $\Delta\varepsilon_{tot}/\sigma$ as a function of the number of cycles i. The discontinuities are due to adjustments of

the load to maintain an approximately constant stress. Before cycling, the sample was not crept isothermally, but was thermally cycled under a small stress of 0.4 MPa which resulted in very small negative strain increments $\Delta\varepsilon_{tot}$ = -0.04%. As shown in Fig. 1.8, the large superplastic strain increments $\Delta\varepsilon_{tot}/\sigma$ = 2.2 GPa^{-1} observed initially upon application of the stress σ = 7 MPa decrease steadily and stabilize after about 35 cycles to a value $\Delta\varepsilon_{tot}/\sigma$ = 1.15 GPa^{-1}. After 140 cycles, the stress was decreased to σ = 1.0 MPa and 1.5 MPa and negative strain increments $\Delta\varepsilon_{tot}$ = -0.05% and $\Delta\varepsilon_{tot}$ = -0.02%, respectively, were measured (these strain increments are not shown in Fig. 1.8). After cooling to room temperature, an optical inspection of the sample showed no signs of necking. The sample was heated again and subjected to low stresses σ = 1.1 MPa and σ = 1.8 MPa resulting in strain increments $\Delta\varepsilon_{tot}$ = -0.07% and +0.03%, respectively (not shown in Fig. 1.8). Upon re-application of a high stress σ = 4.9 MPa, the same value $\Delta\varepsilon_{tot}/\sigma$ = 1.13 GPa^{-1} was obtained as before the interruption. After about 220 cycles, $\Delta\varepsilon_{tot}/\sigma$ increased again, probably because the onset of necking visible in Fig. 1.8 leads to locally higher stresses. Low stress experiments at the end of the experiment again gave negative strain increments $\Delta\varepsilon_{tot}$ = -0.2% to $\Delta\varepsilon_{tot}$ = -0.37% for stresses of $\sigma \approx 0$ - 0.2 MPa.

1.3.3 Thermal Cycling of Fe/TiC Composites

Figure 1.9 shows for the composites the total strain increment as a function of the applied stress for cycles with T_l = 700°C, T_u = 900°C, $\dot{T}$ = 100-200 $K \cdot min^{-1}$ and ν = 6 - 10 hr^{-1}. The strain increments for the Fe/10TiC composite $d(\Delta\varepsilon_{tot})/d\sigma$ = 0.37 GPa^{-1} and for the Fe/20TiC composite $d(\Delta\varepsilon_{tot})/d\sigma$ = 0.20 GPa^{-1}) are much smaller than for unreinforced iron ($d(\Delta\varepsilon_{tot})/d\sigma$ = 1.7 GPa^{-1}). As for unreinforced iron, the isothermal deformation was negligible: for a stress σ = 4.5 MPa at the upper cycling temperature, Fe/10TiC crept at a rate $\dot{\varepsilon} = 1.8 \cdot 10^{-7}$ s^{-1} much lower than the corresponding average cycling strain rate $d(\Delta\varepsilon_{tot})/dt = 3.2 \cdot 10^{-6}$ s^{-1} for σ = 4.6 MPa and ν = 6 hr^{-1}. Under a stress σ = 4.2 MPa,

the Fe/20TiC composite crept isothermally at a rate $\dot{\varepsilon} = 1.0 \cdot 10^{-7}\ s^{-1}$ which was negligible as compared to the average cycling strain rate $d(\Delta\varepsilon_{tot})/dt = 1.6 \cdot 10^{-6}\ s^{-1}$ for $\nu = 6\ hr^{-1}$.

Figure 1.10 shows the stress-normalized strain increment $\Delta\varepsilon_{tot}/\sigma$ as a function of the upper cycle temperature T_u for the Fe/10TiC composite. This figure indicates that the maximum strain increment is obtained at $T_u = 840°C$ and that the contribution of isothermal creep become significant above 900°C.

As shown in Fig. 1.11, the Fe/10TiC sample thermally cycled ($T_l = 700°C$, $T_u = 880°C$) under a constant load provided strain data at increasing stress as the sample cross-section diminished; the linear part of Fig. 1.11 was obtained with $\nu = 6$ - $10\ hr^{-1}$ and the non linear part at a higher cycling frequency $\nu = 30\ hr^{-1}$. The fracture strain of this Fe/10TiC sample, shown in Fig. 1.11, was $e_f = 231\%$.

1.4 Discussion

1.4.1 Thermal Analysis

The DTA curves for unreinforced iron in Fig. 1.2 show peaks at 905°C on heating (symbol □) and 885°C on cooling (symbol ■) caused by the α/γ and γ/α-transformations which are also visible in dilatometric curves (Fig. 1.3) as contraction ($\Delta L/L = -0.52\%$) upon heating from 840°C to 890°C and expansion ($\Delta L/L = +0.37\%$) upon cooling from 870°C to 845°C. These values are comparable to the linear transformation dilatation reported for pure iron $\Delta L/L = 0.35\%$ - 0.38% [8,94] and to the allotropic α/γ-range for Fe - 0.012 wt.% C (814-908°C) [6]. The DTA of iron also reveals peaks 15°C to 20°C below the $\alpha \leftrightarrow \gamma$ temperatures (symbols ▽,▼) which may be attributed to a martensitic transformation, or to the allotropic transformation occurring over the α/γ–range with a recalescence peak (symbol ▼) on cooling. Finally, the DTA curve of iron shows the magnetic transition between

755°C and 765°C on heating (symbol △) and cooling (symbol ▲), in good agreement with the Curie temperature of 770°C [2].

Except for the magnetic transition, the composites exhibit DTA- and dilatometry curves different from those of iron. Upon heating, α/γ peaks (symbols ○ Fig. 1.2) appear around 845°C and 830°C for the 10 vol.% and 20 vol.% composite, respectively. These reactions are preceded by large endothermic peaks (symbol ◇) at 735°C within the ferrite region which correspond to the initial contraction around 700°C found by dilatometry (symbols ◇ Fig. 1.3). Equivalent peaks (symbols ●,◆) appear upon cooling at significant lower temperatures (Figs. 1.2 and 1.3). Figure 1.3 also shows that the length changes of the composites (which have the same magnitude as those of the iron sample) develop over broad temperature intervals, i.e. between 715°C and 820°C on heating (symbols ○) and between 680°C and 805°C on cooling (symbols ●). The temperatures determined by dilatometry are 15°C - 20°C below those obtained by DTA, probably because the heating rates of $\dot{T}$ = 10 K·min^{-1} induced a larger temperature lag in the 1 gram dilatometry sample than in the 0.02 gram DTA samples.

Austenite and ferrite can dissolve 660 ppm and 360 ppm equiatomic TiC at 912°C, respectively [89]. The 300 ppm difference is expected to precipitate and dissolve upon cycling, but corresponds to a volume fraction of 0.05 vol.%, too low to induce significant dilatometric or thermal peaks. Rather, the composite peaks are attributed to a pearlitic invariant reaction $\alpha+Fe_3C+TiC \leftrightarrow \alpha+\gamma+TiC$ (symbols ◇,◆) followed by an allotropic transformation $\alpha + TiC \leftrightarrow \gamma + TiC$ (symbols ○,●). This interpretation is consistent with the metastable ternary C-Fe-Ti phase diagrams [97] showing the above invariant reaction occurring at 740°C, above which a solid solution of carbon and titanium in ferrite transforms continuously to a solid solution of austenite. The higher content of cementite found for the Fe/20TiC composite (Fig. 1.1f,i) is also expected from the higher volume fraction of TiC. The dilatometry results of the composites (Fig. 1.3) are furthermore

consistent with temperature-strain curves for Fe-0.2C samples exhibiting a pearlitic reaction given by Ref. [20]. Thus, we conclude that the precipitates in Figs. 1.1e,f,h,i are cementite (with possibly very small quantities of TiC), as confirmed by their lack of contrast prior to etching, unlike TiC which is visible without etching.

1.4.2 Transformation Superplasticity of Iron

The linear relation given by Eq. 1.1, can be generalized for the case of a continuous phase transformation:

$$d\left(\frac{\Delta\varepsilon}{\sigma}\right) = \frac{5}{6} d\left(\zeta \frac{\Delta V}{V} \frac{1}{\sigma_Y}\right) \tag{1.2}$$

where $\zeta(T,t)$ is the volume fraction of the new allotropic phase dependent on temperature T and time t, and where the yield stress $\sigma_Y[T, c(T,t)]$ is a function of the temperature T and the carbon concentration c(T,t). Even if assuming that the phase transformation is limited by heat transfer, rather than transformation kinetics or diffusion, the right-hand side of Eq. 2 depends on the ratio $\zeta(T)/\sigma_Y(T)$, which cannot be evaluated without detailed knowledge of these variables. Instead Eq. 1.2 can be approximated by using effective values for the yield stress $\sigma_{Y,eff}$ and the volume fraction ζ_{eff}:

$$\Delta\varepsilon = \frac{5}{6} \zeta_{eff} \frac{\Delta V}{V} \frac{\sigma}{\sigma_{Y,eff}} \tag{1.3}$$

The effective quantities also depend on undercooling, which is itself coupled to cycle characteristics, e.g. temperature amplitudes, heating rates and heat flux conditions. Since isothermal creep outside the transformation range was negligible, the measured strain increment $\Delta\varepsilon_{tot}$ accumulated after a full cycle can be directly compared to the superplastic strain increment $\Delta\varepsilon$ predicted by Eq. 1.3. Because the measured strain increments were identical on heating and on cooling (Fig. 1.5), the stress-normalized superplastic strain

increment is $d(\Delta\varepsilon)/d\sigma = d(\Delta\varepsilon_{tot})/(2d\sigma) = 0.85\ GPa^{-1}$. With this experimental value for $d(\Delta\varepsilon)/d\sigma$ and the α/γ-volume mismatch $\Delta V/V = 3(\Delta L/L) = 1.1\%$ [8,94], an effective yield stress $\sigma_{Y,eff} = 10.8$ MPa is obtained from Eq. 1.3. While this value fits the low-stress data in Fig. 1.4, the ideal plastic model predicts infinite strain increments when the applied stress reaches the yield value of 10.8 MPa, much below the stresses of about 16 MPa where finite strain increments are still observed in Fig. 1.4. This can be explained if the yield stress increases from a value of 10.8 MPa at low applied stresses to a value of about 16 MPa at large applied stresses due to strain-hardening when large strain increments are produced. This hypothesis is supported by the high oxygen content of 0.3 wt.% (originating from the fabrication of the iron powders), which corresponds to a volume fraction of 1.5 vol.% of Fe_3O_4 (or 1.6 vol.% of Fe_2O_3), sufficient for significant dispersion strain-hardening.

Both the smaller creep rates observed after cycling, during which the grain size increased by one order of magnitude, and the low stress exponents measured in isothermal experiments indicate that iron deforms by diffusional creep outside the allotropic range. While pure iron is expected to deform by low-temperature power-law creep with a stress exponent of 6.9 within the stress range of interest [31], the observed diffusional creep is attributed to the strengthening effect of carbon and oxide dispersoids which can lower or, respectively, fully inhibit dislocation creep [5], but have little effect on diffusional creep. Also, the change of grain size did not affect the superplastic behavior, which confirms that transformation superplasticity occurs by plastic yield and not by diffusional creep (as for microstructural superplasticity).

The dependence of the transformation superplastic strain $\Delta\varepsilon$ from the temperature cycle amplitudes within the non-linear regions (Fig. 1.6) can only be described qualitatively based on results obtained from the DTA and dilatometry measurements, since the temperature dependence of the ratio $\zeta(T)/\sigma_Y(T)$ is unknown. Dilatometry (Fig. 1.3) indicates that the heating and cooling kinetics of the phase transformation are different, as the $\alpha \rightarrow \gamma$

transformation occurs over a temperature interval ranging from 840°C to 890°C whereas the $\gamma \rightarrow \alpha$ transformation takes place between 870°C and 845°C. This 20°C undercooling for the onset of the $\gamma \rightarrow \alpha$ transformation is consistent with the 20°C shift in the $\gamma \leftrightarrow \alpha$ DTA peaks (Fig. 1.2). Upon partial cyclic transformation from the ferrite to austenite, i.e. variation of the upper cycling temperature, strain increments are expected to appear as soon as the upper cycling temperature exceeds 840°C and to increase until 890°C where $\zeta_{eff} = 1$ (Fig. 1.6); the increase is probably near linear with temperature, based on the near linear dilatometric expansion and contraction (Fig. 1.3). On cycling from, and to, the austenitic state a critical temperature amplitude is necessary to induce transformation superplastic strains (Fig. 1.6), similar to observations made in CTE-mismatch superplasticity of Al/SiC [71]. This temperature threshold can be explained by two phenomena. First, the $\gamma \rightarrow \alpha$ transformation is undercooled by 20°C, as discussed above. Second, because of the high strength of austenite, the initial transformation mismatch can be accommodated elastically, so that ferrite has to form a continuous network before plastic strain can be observed. However, once the temperature threshold (estimated as $\Delta T = 40$ K in Fig. 1.6) is exceeded, a steep increase of the partial transformation strains is expected according to the $\gamma \rightarrow \alpha$ transformation shown from dilatometry and DTA (Fig. 1.3).

The ratio $d(\Delta\varepsilon_{tot})/d\sigma = 1.7$ GPa^{-1} measured for iron is significantly smaller than the values of 2.5 - 2.6 GPa^{-1} reported by Refs. [17,20,39] but comparable to the value of 1.5 - 1.7 GPa^{-1} given in Ref. [69] (Table 1.4). As shown in Fig. 1.12, there is a strong decrease of $\Delta\varepsilon_{tot}/\sigma$ (or $d(\Delta\varepsilon_{tot})/d\sigma$) with increasing carbon concentration, and our data fall within the region where the ratio $\Delta\varepsilon_{tot}/\sigma$ is very sensitive to the presence of carbon. This is due to the strengthening effect of carbon, which increases the yield stress of the ferrite and thus decreases the value of the superplastic strain increment $\Delta\varepsilon$ (Eq. 1.3). Also, we find the same strain increments on heating and on cooling (Fig. 1.5), whereas unequal strain increments have been reported in the literature (Table 1.4). This may be due to unequal

creep contributions outside the transformation range (ferrite creeps faster than austenite for pure iron), to differences in heating and cooling transformation temperatures (affecting the yield stress), or to different heating and cooling rates (leading to variable ratchetting). The latter mechanism is discussed in more detail in the following.

Figures 1.13a and 1.13b show the evolution with increasing cycle number of the stress-normalized superplastic strain increment with and without isothermal creep prior to thermal cycling. In the former case, the sample is first loaded until a steady-state creep rate is reached, and then thermally cycled. Steady-state strain increments are obtained quickly after about 4 complete cycles (Fig. 1.13a). Since the strain is determined from the total load train displacement undergoing thermal expansion and contraction during cycling, the convergence behavior in Fig. 1.13a reflects the establishment of the dynamic thermal steady-state in the sample and the pullrods due to thermal cycling. When the stress was changed during thermal cycling, steady-state increments were obtained after completion of a single cycle. Thus, the establishment of an equilibrium dislocation structure after a changes in stress, which is responsible for primary creep, is very rapid upon phase transformation cycling conditions, and primary creep does not contribute significantly to the measured strain, provided the sample was prestrained.

On the other hand, if a sample is first thermally cycled at a small stress to establish thermal equilibrium, and then loaded to a high stress without prestraining, steady-state strain increments are obtained only after 35 cycles (Fig. 1.13b). This long initial transient is attributed to primary creep which decreases over time. At steady-state, the stress normalized strain increment (1.15 GPa^{-1}) is however lower than that obtained from Fig. 1.13a (1.67 GPa^{-1}). This result is attributed to ratchetting which induces plastic deformation under no or little applied stress as a result of a macroscopic strain gradient traveling through the sample, due to a sharp phase front produced by a steep temperature gradient [86]. In the case of iron where the stronger phase (γ-Fe) is denser than the weaker phase (α-Fe), ratchetting causes a

contraction perpendicular to the propagation direction of the phase front [86], i.e. in the axial direction of the radially heated samples.

The presence of ratchetting was confirmed by the following experiments. When a thin, 1.6 mm in diameter, grounded K-type thermocouple with a fast response was used to control the sample surface temperature, no ratchetting was observed since the stress normalized strain increment $\Delta\varepsilon_{tot}/\sigma$ = 1.67 GPa^{-1} (Fig. 1.13a) was identical to the differential slope $(d\Delta\varepsilon_{tot})/d\sigma$ = 1.7 GPa^{-1} (Fig. 1.4). In this case, the macroscopic phase front is diffuse as the surface temperature measured by the thermocouple accurately reflects the sample temperature. However, when a thick, 3.2 mm in diameter, ungrounded R-type thermocouple was used to control the surface temperature, a much higher heat flux was delivered by the furnaces due to the slow response of the thermocouple, leading to a sharper transformation front. As expected, ratchetting was then observed as a decrease of the stress-normalized strain increments $\Delta\varepsilon_{tot}/\sigma$ = 1.2 GPa^{-1} (Fig. 1.13b) after 35 cycles.

The average ratchetting strain $\Delta\varepsilon_{tot,0}$ can be estimated, from the difference between the slope in Fig. 1.4 ($(d\Delta\varepsilon_{tot})/d\sigma$ = 1.7 GPa^{-1}) and the above stress-normalized strain increments $\Delta\varepsilon_{tot}/\sigma$:

$$\Delta\varepsilon_{tot,0} = \left(\frac{d(\Delta\varepsilon_{tot})}{d\sigma} - \left. \frac{\Delta\varepsilon_{tot}}{\sigma} \right|_{\sigma} \right)\sigma \qquad (1.4)$$

With σ = 7.2 MPa (Fig. 1.13b), Eq. (1.4) gives $\Delta\varepsilon_{tot,0}$ = 0.40% and with $\Delta\varepsilon_{tot}/\sigma$ = 1.13 at σ = 4.9 MPa (Fig. 1.8, $\Delta\varepsilon_{tot,0}$ = 0.28% is obtained. Considering the case of a phase transformation front traveling radially in a cylindrical specimen consisting of a rigid phase and a perfectly plastic phase with low yield stress, an estimate for the ratchetting strain is $\Delta\varepsilon_{tot,0} = (2/3)|\Delta V/V|$ = 0.70% for a full cycle encompassing two allotropic transformations. This estimate is reasonably close to the values obtained from Eq. 1.4 and the low-stress measurements giving $\Delta\varepsilon_{tot}$ = -0.2% to -0.37%.

Finally, ratchetting is not constant in the long-term experiment (Fig. 1.8), where the magnitude of the measured negative ratchetting strains was significantly larger at the end of the experiment. A possible explanation is that the decreased cross-sectional area increased the net energy flux from the furnace and thus sharpened the transformation front. As for the decreasing primary creep contribution, this effect results in a continuously decreasing value of $\Delta\varepsilon_{tot}/\sigma$.

1.4.3 Transformation Superplasticity of Fe/TiC Composites

In contrast to titanium containing 10 vol.% TiC particles which exhibited a significantly higher value of $d(\Delta\varepsilon_{tot})/d\sigma$ as compared to unreinforced titanium [26], the iron-based composites in the present investigation display values of $d(\Delta\varepsilon_{tot})/d\sigma$ substantially lower than the unreinforced matrix. This discrepancy can be explained by two major differences existing between these systems. First, the titanium composites relaxed internal allotropic stresses by power-law creep. Unlike time-independent plasticity by yield for the present iron-based composites, the creep strain-rate of the titanium system is very stress-sensitive, so that stress concentration due to mismatch between the elastic reinforcement and the transforming matrix induce large strains. Second, it is apparent from the metallographic sections (Figs. 1.1d-i) and the thermal analysis (Figs. 1.2 and 1.3) that the matrices of the composites are different from the unreinforced iron sample and from each other, due to the slight solubility of TiC in iron, increasing both substitutional (Ti) and interstitial (C) content in the matrix, and leading to cementite precipitation below 740°C, as discussed earlier. As shown in Fig. 1.12, both substitutional alloying elements and carbon result in lowered superplastic strains. The slight dissolution of TiC into iron thus leads to a matrix with a substantially higher intrinsic strength and lower transformation temperatures, so that the compositional differences between the three types of samples overwhelm any effects due to reinforcement volume fraction.

In allotropic composites, two additional sources of mismatch between matrix and reinforcement exist if the interface between the reinforcement and the matrix is well bonded, as in Fe/TiC where the reinforcement shows some solubility in the matrix (but unlike an insoluble, weakly-bonded systems such as Fe/Al_2O_3, where interface fracture occurs upon phase transformation [10]). First, if the two phases have different coefficients of thermal expansion (CTE), thermal mismatch stresses occur during a thermal excursion ΔT, which can lead to superplastic strain increments as observed in Al/SiC composites upon repeated thermal cycling [27]. Second, if the matrix is allotropic, its transformation in the presence of non-transforming particulates also induces mismatch stresses and a corresponding superplastic strain increment, as recently observed in the Ti/TiC system [26]. Assuming that these contribution occur independently, an effective mismatch $(V/V)_{eff}$ can be defined with the rule of mixture:

$$\left(\frac{\Delta V}{V}\right)_{eff} = (1-f)\left|\frac{\Delta V}{V}\right| + f\left|\frac{\Delta V}{V} + 3\Delta\alpha\Delta T\right| \qquad (1.5)$$

where f is the volume fraction of reinforcement and $\Delta\alpha$ is the difference between the reinforcement CTE and the average matrix CTE (all CTE are assumed isotropic) over the temperature interval ΔT. In Eq. 1.5, the first term, $(1\text{-}f)|\Delta V/V|$, is the transformation mismatch within the matrix and the second term, $f|\Delta V/V+3\Delta\alpha\Delta T|$, is the composite mismatch between the matrix and the reinforcement, consisting of both transformation and thermal expansion.

In the Fe/TiC system, the thermal and allotropic mismatch strains have opposite signs, i.e. on heating the thermal expansion mismatch between iron and TiC partially offsets the contraction due to the α/γ-phase transformation of iron. Neglecting the small thermal expansion mismatch outside the transformation range (which is assumed to be elastically accommodated), we consider only the mismatch within the interval $\Delta T = +130$ K where the phase transformation (including the pearlitic reaction) occurs for the composites (Fig. 1.3).

We take for TiC a CTE value $\alpha = 8.0 \cdot 10^{-6}$ K^{-1} [92] and for the matrix an average of the CTE for ferrite $\alpha = 16.6 \cdot 10^{-6}$ K^{-1} [94] and for austenite $\alpha = 23.3 \cdot 10^{-6}$ K^{-1} [94]. With a maximum thermal mismatch $3\Delta\alpha\Delta T = +0.47\%$ and an allotropic mismatch $\Delta V/V = -1.1\%$ [8,94], the effective mismatch given by Eq. 1.5, which reduces for the present case to $|\Delta V/V+3f\Delta\alpha\Delta T| = 1.05\%$ for Fe/10TiC and $|\Delta V/V+3f\Delta\alpha\Delta T| = 1.01$ for Fe/20TiC. Effective yield stresses of 47 MPa and 84 MPa, respectively, are then calculated from Eq. 1.3 for the ferritic matrices of the composites. While these values are much higher than for the unreinforced iron specimen, they are within a physically plausible range. They cannot however be directly compared to a yield stress experimentally determined by tensile testing, as they correspond to an average over the transformation range of the yield stress, as discussed earlier. Introducing the above effective yield stress values and the allotropic matrix mismatch $|\Delta V/V| = 1.1\%$ in Eq. 1.3, we get $d(2\Delta\varepsilon)/d\sigma = 0.39$ GPa^{-1} and 0.22 GPa^{-1} for the unreinforced matrices, which is within the range of values observed in Fig. 1.12 for carbon-containing alloyed steel.

Finally, the Fe/10TiC fracture experiment demonstrates that superplastic strains (e_f = 231%, Fig. 1.11) can be reached in tension in these composites, despite their room-temperature brittleness and hardness. The experiment also illustrates that rapid strain rates can be obtained: for a strain increment of 2.4% per cycle (applied stress of 35 MPa, Fig. 1.11) and a cycling frequency of 30 hr^{-1}, the measured average strain rate of $d(\Delta\varepsilon_{tot})/dt = 2 \cdot 10^{-4}$ s^{-1} is well within the range used for commercial superplastic forming.

1.5 Conclusions

Transformation superplasticity was studied in iron samples subjected to temperature cycling through the α/γ-phase field with a superimposed external uniaxial stress.

1. Within the stress range of interest, deformation by steady-state creep is insignificant as compared to transformation superplastic deformation. If the materials is not crept prior to cycling, primary creep can however contribute to the measured transformation superplastic strains, but this contribution diminishes with time. Also, thermal ratchetting is observed under high heat flux conditions where a sharp transformation front is created; the observed contraction of 0.3% is in agreement with existing ratchetting models.
2. When ratchetting and primary creep are eliminated, equal strain contributions result from the α/γ and γ/α transformations. The strain per cycle is linearly proportional to the applied stress ($\Delta\varepsilon_{tot}/\sigma = 1.7\ GPa^{-1}$) for stresses up to 6 MPa, but increases non-linearly for higher stresses.
3. By considering effective quantities for the yield stress and the volume mismatch, the yield model of Greenwood and Johnson [39] can be adapted to describe the present case of a phase transformation through a two-phase field were the above properties are temperature and/or concentration dependent. The effective yield stress determined within the linear range (10.8 MPa) is significantly smaller than the effective yield stress deduced from the non-linear divergence (16 MPa). This is attributed to strain hardening caused by dissolved carbon and iron-oxide dispersoids.
4. When partially cycling from the austenite field, superplastic strains are initially smaller than when partially cycling from the ferrite field. This behavior is explained by undercooling of the transformation and by elastic accommodation of mismatch stresses in the strong austenite.

Transformation superplasticity was investigated in iron-matrix composites containing 10 vol.% and 20 vol.% TiC particulates.

1. Superplastic behavior was demonstrated for the Fe/10TiC composite which showed a total tensile fracture strain of 231%, which was however smaller than the strain of 454% achieved without failure in unreinforced iron. Average strain rates of $2 \cdot 10^{-4}$ s^{-1} can be achieved in that composite, comparable to those used in commercial superplastic operations.
2. Composites show transformation superplastic strain increments ($\Delta\varepsilon_{tot}/\sigma$ = 0.37 GPa^{-1} for Fe/10TiC and $\Delta\varepsilon_{tot}/\sigma$ = 0.20 GPa^{-1} for Fe/20TiC) which are lower than for unreinforced iron. This is attributed to the slight dissolution of TiC in the matrix, which increases its yield strength by solid solution strengthening and by reducing the transformation temperature range (as also observed by dilatometry and calorimetry).
3. The yield model of Greenwood and Johnson [39] predicts effective matrix yield stresses of 47 MPa for Fe/10TiC and 84 MPa for Fe/20TiC. The composite superplastic strains are comparable to literature data for unreinforced steels which also show decreasing transformation superplastic strains with increasing carbon content.
4. Calorimetry and dilatometry show that the α/γ allotropic transformation followed by cementite precipitation occurs over a broad temperature interval of 130°C. Strains produced by partial transformation through this phase field increase linearly with the temperature excursion, in agreement with the expected mismatch evolution determined by dilatometry.

Figures of Chapter 1

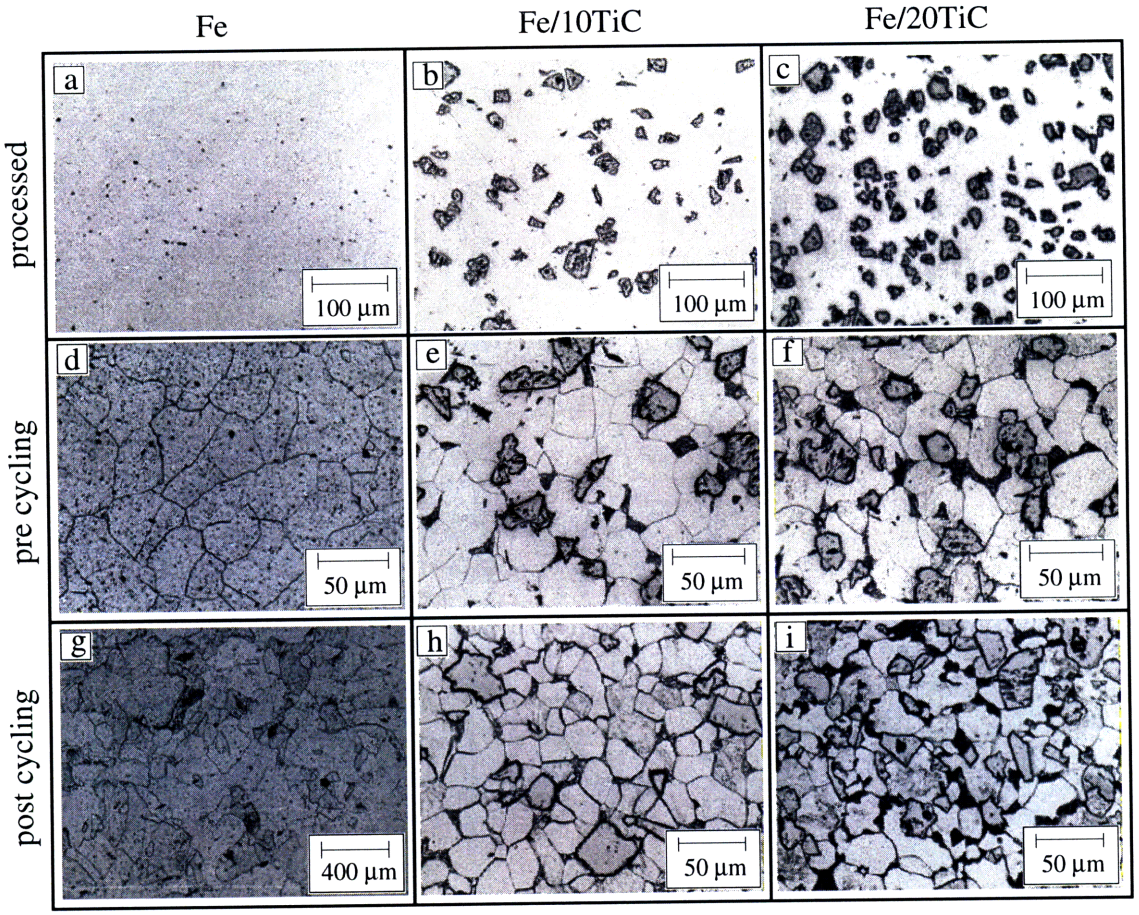

Figure 1.1: Micrographs of iron, Fe/10TiC and Fe/20TiC samples before thermal cycling (unetched), before thermal cycling (etched) and after thermal cycling (etched).

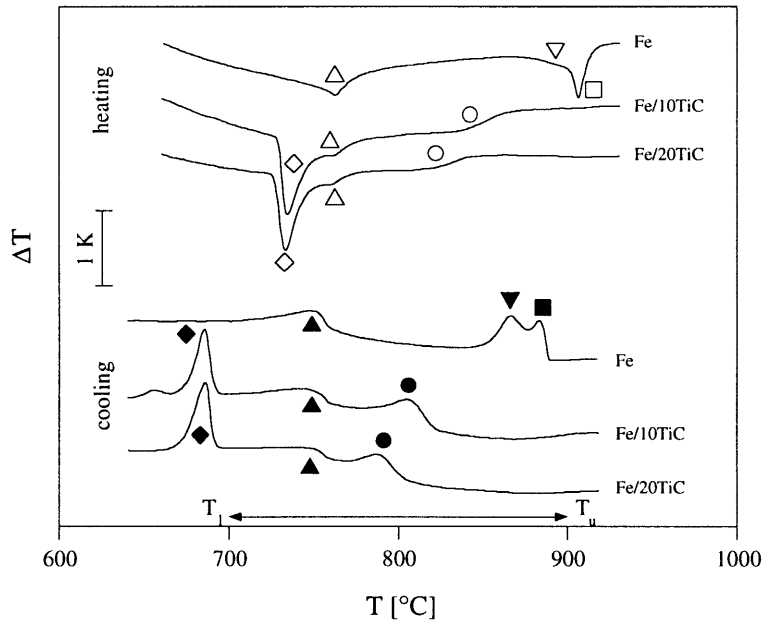

Figure 1.2: Differential thermal analysis of iron and Fe/TiC composites with $\dot{T}$ = 10 K·min^{-1}; $\alpha \leftrightarrow \gamma$ transformation □,■; martensite reactions or $\alpha \leftrightarrow \gamma$ recalescence peak ▽,▼; magnetic transition △,▲; α+TiC $\leftrightarrow$ γ+TiC transformation ○,●; Fe_3C+TiC+$\alpha \leftrightarrow \alpha+\gamma$+TiC reaction ◇,◆.

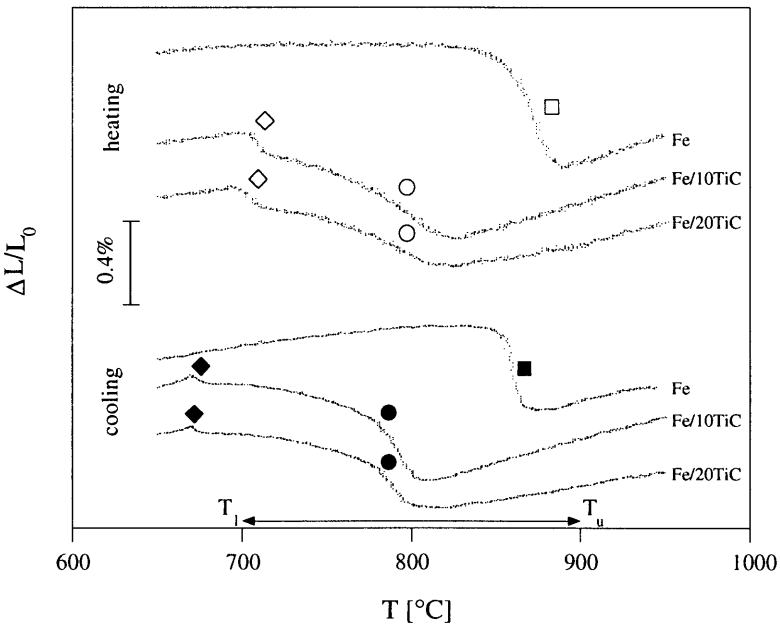

Figure 1.3: Dilatometry of Iron and Fe/TiC composites with $\dot{T}$ = 10 K·min^{-1} (same symbols as in Figure 1.2).

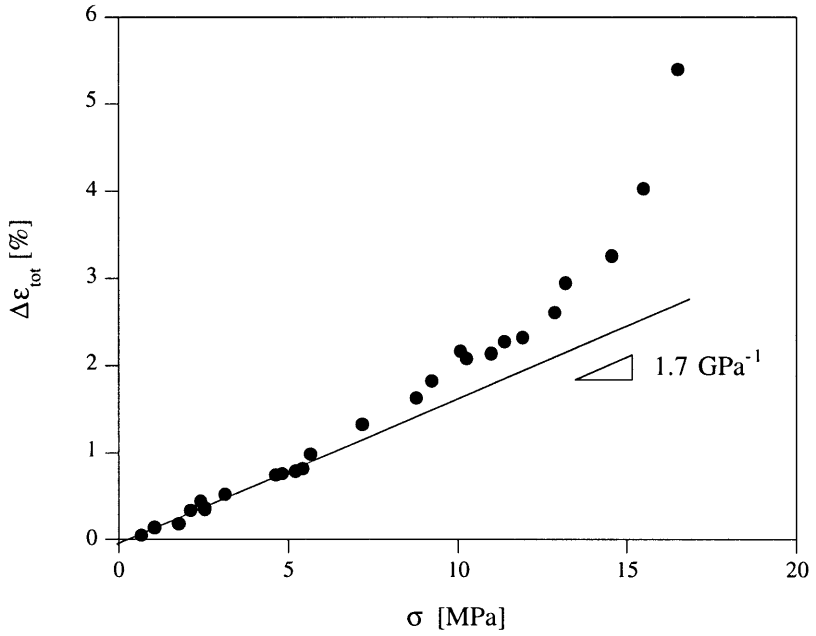

Figure 1.4: Strain increment per cycle as a function of the applied stress for iron (T_l = 700°C, T_u = 900°C, ν = 6 - 10 hr^{-1}).

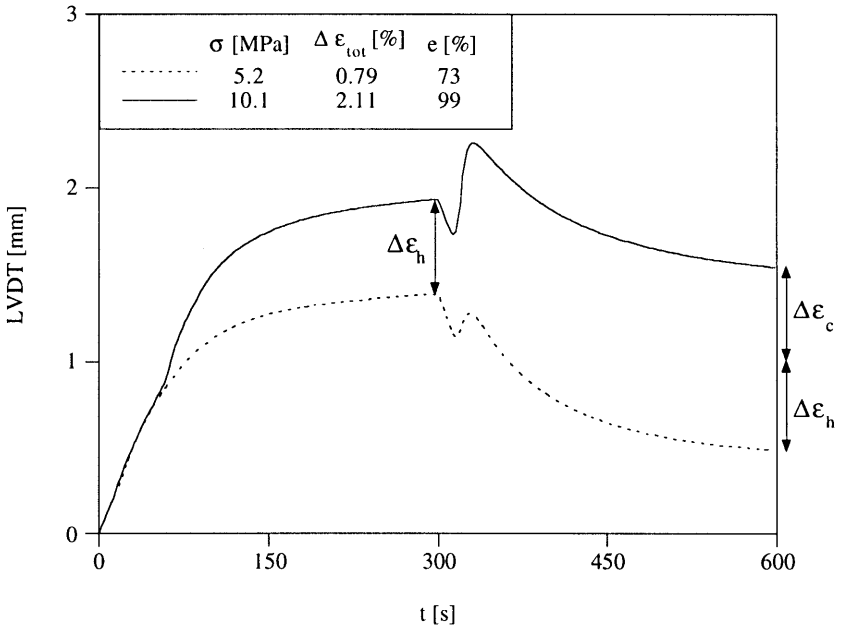

Figure 1.5: Total deformation of two cycles with two different stress levels for iron.

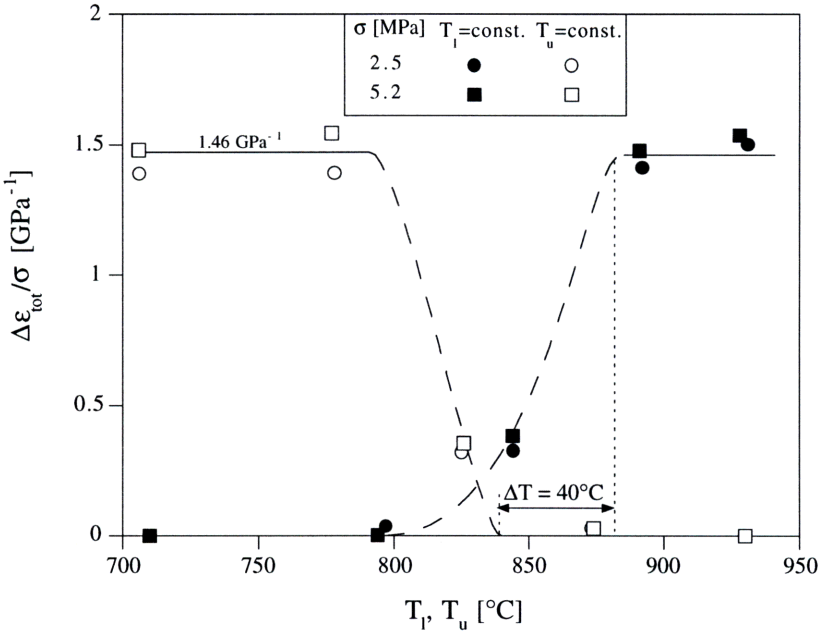

Figure 1.6: Stress-normalized strain increment for iron as a function of the upper temperature for cycles with a constant lower temperature T_l = 710°C and as a function of the lower temperature for cycles with a constant upper temperature T_u = 930°C; (ν = 10 hr^{-1}, σ = 2.5 MPa, 5.2 MPa).

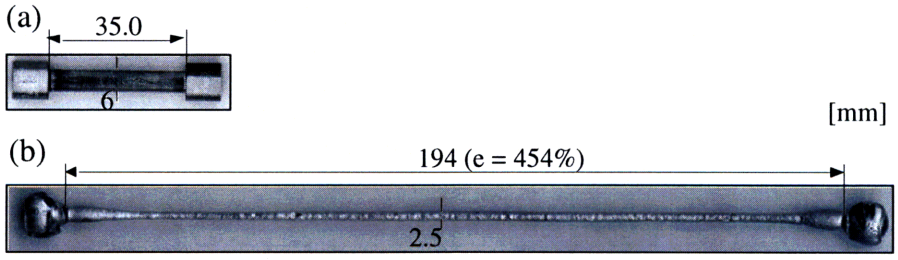

Figure 1.7: Iron sample (a) undeformed, (b) deformed at constant stress for 242 (σ = 7.2 for 140 cycles and σ = 4.9 for 102 cycles) for cycles between 700°C and 900°C (ν = 15 hr^{-1}).

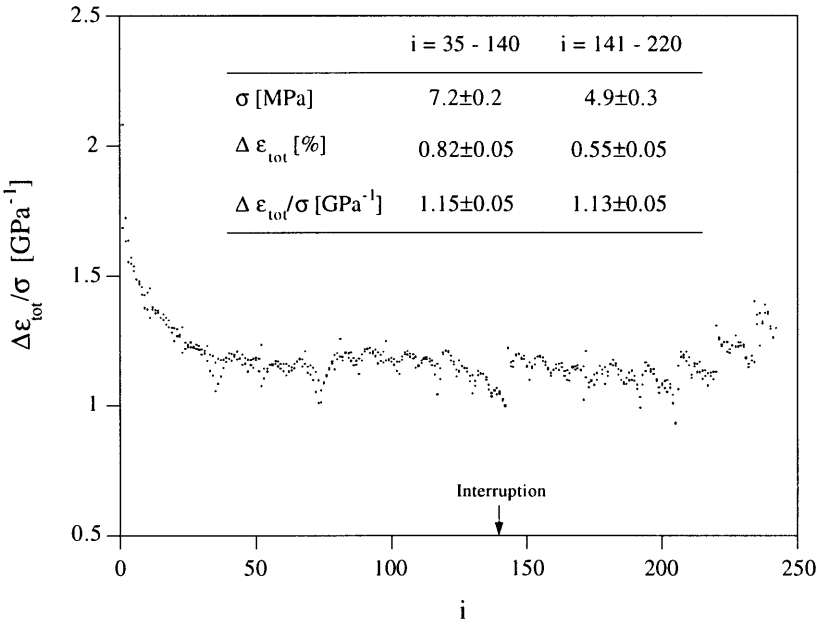

Figure 1.8: Stress-normalized strain increment as a function of the number of cycles for iron; no isothermal pre-creep prior to thermal cycling (T_l = 700°C, T_u = 900°C, ν = 15 hr^{-1}).

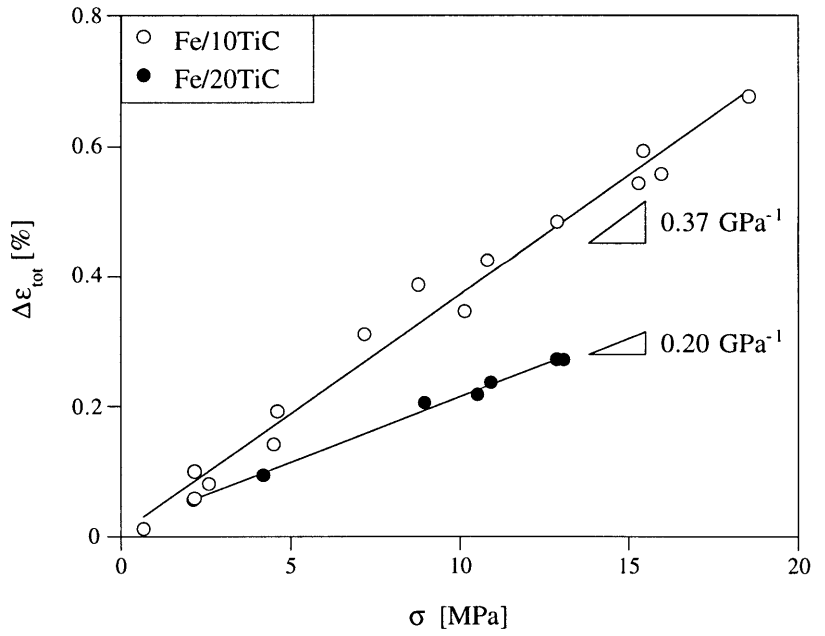

Figure 1.9: Strain increment per cycle as a function of the applied stress for Fe/10TiC and Fe/20TiC composites (T_l = 700°C, T_u = 900°C, ν = 6 - 10 hr^{-1}).

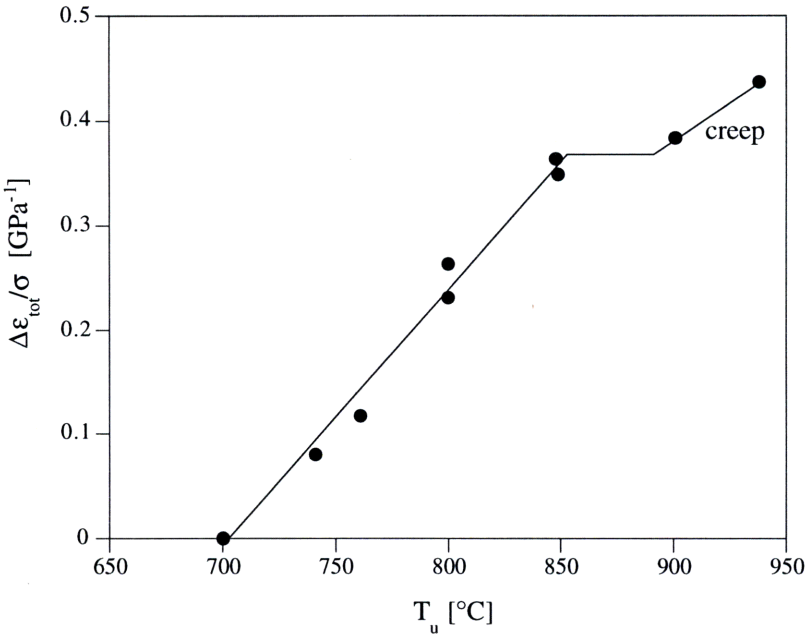

Figure 1.10: Stress-normalized strain increment as a function of the upper cycling temperature for cycles with constant lower temperature $T_l = 700°C$ ($\nu = 6$ hr^{-1}, $\sigma = 14.4$ - 15.6 MPa).

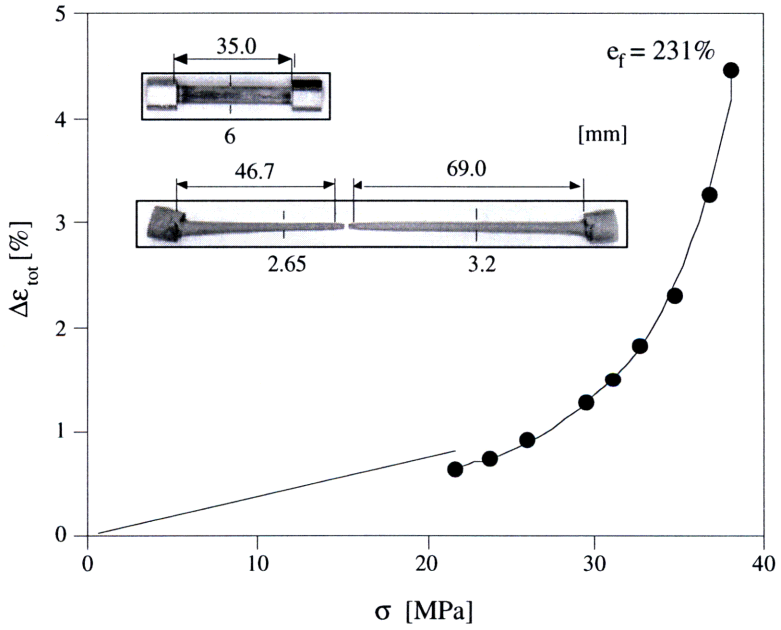

Figure 1.11: Total strain increment per cycle as a function of the applied stress for Fe/10TiC deformed until fracture at constant load ($T_l = 730°C$, $T_u = 880°C$, $\nu = 30$ hr^{-1}); the line for $\sigma < 21$ MPa is taken from Fig. 1.9; in inset are pictures of the sample before and after deformation.

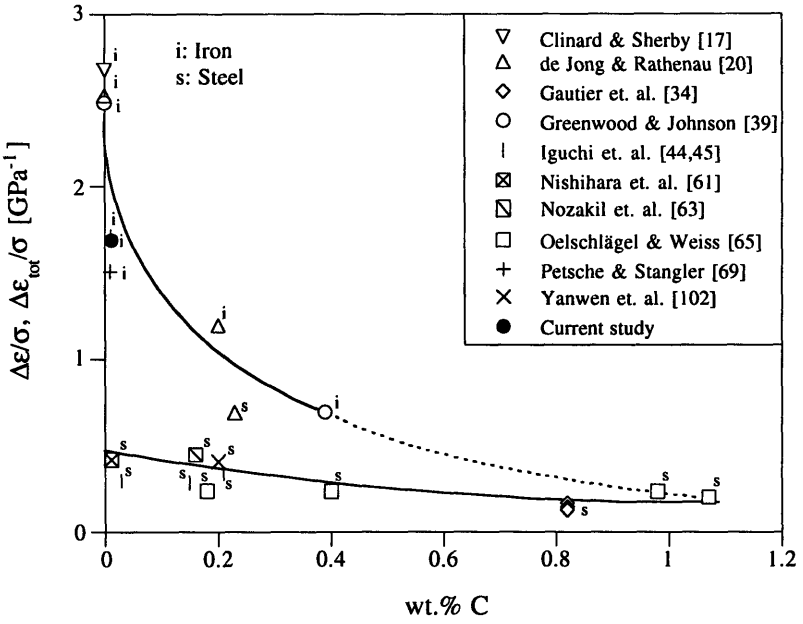

Figure 1.12: Effect of the carbon content of iron and steel on the stress-normalized total strain per cycle (Table 1.4).

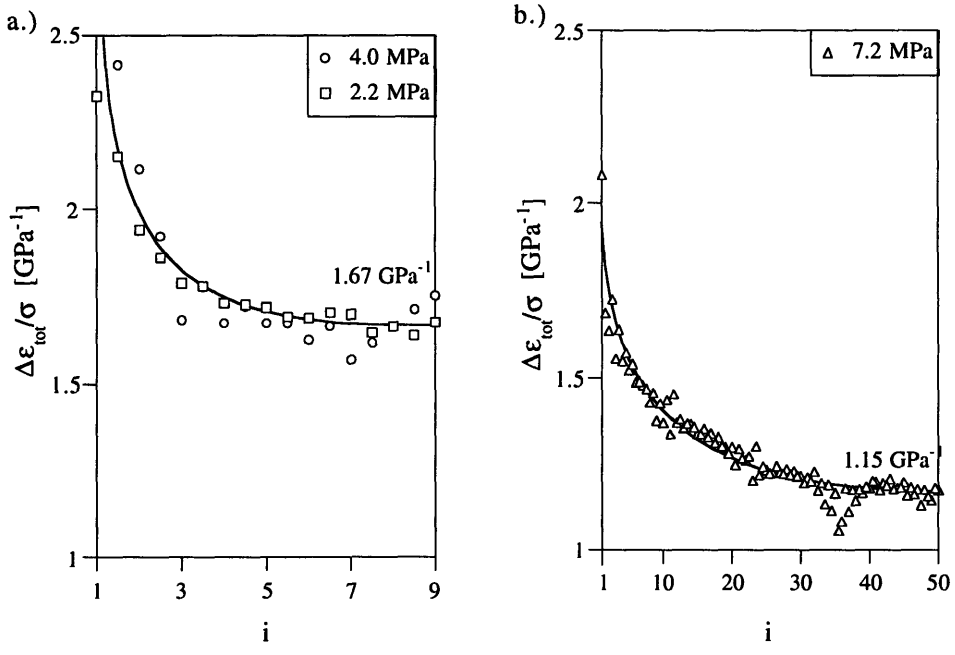

Figure 1.13: Convergence behavior of the stress-normalized strain increments as a function of the number of cycles for iron: (a) with isothermal creep prior to thermal cycling and with a fast response thermocouple; (b) without isothermal creep prior to thermal cycling (promoting primary creep) and with a slow-response thermocouple (promoting ratchetting).

Tables of Chapter 1

Table 1.2: Chemical compositions.

Material	Carbon [wt.%]	Other Elements [wt.%]	Analysis
Fe (as received)	0.009	0.003 N 0.28 O	Alfa Aesar, MA
Fe (HIPed)	0.012	0.018 Si 0.019 Mn	Luvak, MA
TiC (as-received)	19.6±0.1		Massachusetts Materials Research, MA

Table 1.3: Porosity (v) and density (ρ) for iron and Fe/TiC MMCs after cold-pressing, HIPing and deformation to strain e_3.

Material	After cold-pressing	After HIPing		After deformation		
	v_1 [vol.%]	ρ_2 [g·cm^{-3}]	v_2 [vol.%]	ρ_3 [g·cm^{-3}]	v_3 [vol.%]	e_3 [%]
Fe	48.0	7.81	0.2	7.82	0.2	172
Fe/10TiC	44.9	7.54	0.0	7.54	0.0	51
Fe/20TiC	41.4	7.24	0.1	7.25	0.0	2

Table 1.4: Composition, stress-normalized strain increment and elongation to fracture found in literature for transformation superplasticity of iron and steel.

Material*	Carbon wt.%]	Other Elements [wt.%]	$\Delta\varepsilon_{tot}/\sigma$ or $(d\Delta\varepsilon_{tot})/d\sigma$ heating [GPa^{-1}]	cooling	total	Elong. [%]	Ref.
Iron	---	---			2.5		[39]
Iron	0.39	---			0.7		
Iron	---	(0.008 N)			2.5		[20]
Iron	0.2	---			1.2		
Steel	0.23	0.49			0.70		
Iron	0.02	(0.15)	1.6	1.0	2.6		[17]
Iron	0.01	(traces)			1.5		[69]
Iron	0.011	(0.03)			1.7		
Steel AISI 1095	0.98	0.58	0.13	0.11	0.24	580	[65]
Steel AISI 1045	0.40	0.97	0.13	0.11	0.24	500	
Steel AISI 1018	0.18	0.84	0.13	0.11	0.24	515	
Steel AISI 52100	1.07	2.17	0.12	0.09	0.21	720	
Steel	0.82	1.13			0.15		[34]
Iron	0.2	---			0.41		[102]
Steel	0.03	0.49	0.19	0.13	0.32	92	[44]
Steel SS41	0.15	0.46	0.19	0.09	0.28		[45]
Steel S20C	0.21	0.58	0.17	0.17	0.34		
Steel S15CK	0.16	1.06	heat > cool		0.45	> 500	[64]
Steel	0.012	0.30	0.16	0.26	0.42		[61]
Steel SK5	0.90	0.77		0.08			
Steel SS41	0.15	0.53		0.10			
Iron	0.012	(0.04) 0.28 O	0.85	0.85	1.7	> 454	present study

* labeled "Iron", if no significant alloying elements other than carbon are present, "Steel" otherwise.

Chapter 2

A Non-Linear Model for Internal Stress Superplasticity

Abstract

Current theoretical models of internal-stress superplasticity predict a linear relationship between the applied stress and the plastic strain per cycle, and are only valid at low applied stresses. In the present chapter, we extend the original linear theory of phase transformation superplasticity by Greenwood and Johnson [39] and derive a non-linear closed-form solution valid over the whole range of stresses, from the low-stress regime (where a linear relationship between strain and stress is predicted in agreement with the model by Greenwood and Johnson [39], to the high-stress regime (where the strain increases non-linearly as the applied stress approaches the yield stress of the weakest phase). The model is found to be in agreement with literature data on transformation superplasticity of iron spanning both stress regimes. Furthermore, the model is adapted to the case where internal stresses are produced by thermal expansion mismatch: it is compared to experimental literature data for metals with anisotropic thermal expansion (Zn and U) and for metal matrix composites with inhomogeneous thermal expansion (Al/SiC).

2.1 Introduction

Internal stress superplasticity in polycrystalline materials can be induced upon biasing of internal mismatch stresses or strains, that are produced during a thermal excursion, by an externally applied stress. This thermal mismatch can occur (i) between grains with anisotropic coefficients of thermal expansion (CTE), e.g., in zinc [72,101] and uranium [54,101]; (ii) between phases with different CTE, e.g., in Al/SiC [15,27,71]; or (iii) between grains during a phase transformation exhibiting two allotropes with different densities, e.g., in iron [17,20,39,108] and titanium [14,26,39]. Upon repeated thermal cycling, plastic increments can be accumulated to give large total strains 100 without failure, a mechanism called CTE-mismatch superplasticity or transformation mismatch superplasticity, respectively. Depending on the homologous temperature and the nature of the material, internal stresses are relaxed either by a time-dependent mechanism at high homologous temperatures, i.e., creep, or by a time-independent mechanism at low homologous temperatures, i.e., yield. Assuming an ideally plastic material undergoing a phase transformation, Greenwood and Johnson [39] derived an approximate analytical solution for the strain per transformation (e.g., either α-Fe to γ-Fe or γ-Fe to α-Fe) as a function of the volume mismatch $\Delta V/V$ between the two allotropic phases, the externally applied uniaxial stress σ and the yield stress σ_Y of the weaker phase:

$$\varepsilon \sim \frac{5}{6}\frac{\Delta V}{V}\frac{\sigma}{\sigma_y} \tag{2.1}$$

Petsche and Stangler [69] extended the model by Greenwood and Johnson [39] qualitatively to include temperature cycle characteristics, e.g., cycle amplitude and frequency. Diani et. al. [22] and Sato and Kuribayashi [81] developed complex theoretical models based on continuum micromechanics for transformation induced plasticity and internal stress superplasticity, respectively. Applying these models to a phase transformation with a volume mismatch under a uniaxial external stress gives linear relations between the plastic

strain and the applied stress similar to Eq. 2.1. Kot and Weiss [50] developed a dislocation based model and derived an equation similar to Eq. 2.1 except that the yield stress is replaced by the internal stress due to the transformation. Poirier [73] also derived a dislocation based model and showed that the result can be reduced to Eq. 2.1. That model was extended by Gautier et. al. [35] to include the kinetics of the phase transformation, also showing a linear relationship between plastic strain and applied stress. Other authors have treated the case of CTE-mismatch superplasticity in a similar manner, as reviewed in Ref. [27].

In summary, all existing models for low-temperature phase transformation plasticity predict a linear relationship between $\Delta\varepsilon$ and σ as shown in Eq. 2.1. However, the derivation by Greenwood and Johnson [39] (summarized in App. A) uses assumptions which limit the validity of Eq. 2.1 to small strains, i.e., $\varepsilon << \Delta V/V$ or, equivalently, to small applied stresses, i.e., $\sigma << \sigma_Y$. Greenwood and Johnson's model was tested experimentally by many investigators for allotropic metals such as iron [17,20,39,69,108], cobalt [39,104], uranium [39], titanium [14,26,39], and zirconium [39]. The first three of these metals are most appropriate for comparison to Eq. 2.1, as creep is slow at their transformation temperatures and the assumption of ideal plasticity is thus accurate. Figure 2.1 shows literature results reported by Greenwood and Johnson [39], Clinard and Sherby [17], de Jong and Rathenau [20] and Zwigl and Dunand [108] for transformation superplasticity of iron containing little or no alloying elements. In that figure, $\Delta\varepsilon_{tot}$ is defined as the strain per full thermal cycle, i.e., α-γ-α. As discussed later, the scatter between the experimental curves in Fig. 2.1 can be attributed to varying impurity and carbon contents in the samples investigated. In general, linear relationships are observed at small strains or stresses, in qualitative agreement with the predictions of Eq. 2.1. However, at higher strains or stresses a considerable deviation from linearity occurs. This effect could be attributed either to the transition from time-independent to time-dependent material

behavior (i.e., creep) or to the breakdown of Eq. 2.1 at high stresses. Since creep is insignificant in the above experiments [17,20,39,108], the non-linear behavior in Fig. 2.1 is an intrinsic behavior which cannot be modeled with the existing linear theories.

In the present chapter, we model internal stress superplasticity of an ideal plastic material exhibiting high strains per transformation by extending Greenwood and Johnson's theory to applied stresses up to the yield stress. We then compare the model predictions to literature values that show non-linear transformation superplastic behavior, e.g., iron. Furthermore, we apply our model to superplasticity induced by other internal stress mechanisms, i.e., anisotropic thermal expansion mismatch and composite thermal expansion mismatch.

2.2 Analytical Model

As summarized in Appendix A, Eq. 2.1 was derived under the assumption that the plastic strain increment ε is much smaller than the transformation volumetric mismatch $\Delta V/V$, i.e., for small applied stresses. But if the plastic strain becomes comparable to, or even larger than the volumetric mismatch, the non-linear terms ignored by Greenwood and Johnson [39] in their derivation (see App. A) cannot be neglected and Eq. 2.1 is invalid.

We first define dimensionless stresses and strains:

$$\alpha = \frac{\varepsilon}{\Delta V / V} \tag{2.2}$$

$$\beta = \frac{\sigma'_{zz}}{\sigma_Y} \tag{2.3}$$

$$\gamma = \frac{(\Delta V / V)_{zz}}{\Delta V / V} \tag{2.4}$$

$$\delta = \frac{\sigma}{\sigma_Y} \tag{2.5}$$

where σ'_{zz} and $(\Delta V/V)_{zz}$ are defined in Appendix A. With these definitions, Eq. A15 is written as:

$$\beta = (\alpha - \gamma)\left(1 + \frac{9}{4}\alpha^2 - \frac{9}{2}\alpha\gamma\right)^{-1/2} \tag{2.6}$$

Rather than expanding terms and linearizing the resulting expression as done by Greenwood and Johnson (see App. A), we determine the volume average over both sides of Eq. 2.5 and use Eqs. 2.3, 2.4 and A17 to get:

$$\delta = \frac{3}{2}\frac{\int(\alpha - \gamma)\left(1 + \frac{9}{4}\alpha^2 - \frac{9}{2}\alpha\gamma\right)^{-1/2} d\Omega}{\int d\Omega} \tag{2.7}$$

where Ω is a spherical volume element. With $(\Delta V/V)_{zz}$ given by Eqs. A7-A10 the right hand side of Eq. 2.6is solved analytically, giving:

$$\delta = \frac{1}{4} + \frac{1}{6\alpha} + \frac{1}{2\sqrt{2\alpha}}\left(\frac{3\alpha}{4} - \frac{1}{6} - \frac{1}{9\alpha}\right)\ln\left[\frac{\left(3\alpha + 3\sqrt{2\alpha} + 2\right)^2}{9\alpha^2 - 6\alpha + 4}\right] \tag{2.8}$$

Eq. 2.8 is obtained without the assumption of small strain ($\varepsilon << \Delta V/V$) and is thus valid for all applied stresses below the yield stress, unlike Greenwood and Johnson's original solution (Eq. 2.1), expressed in dimensionless form as:

$$\delta \sim \frac{6}{5}\alpha \tag{2.9}$$

Fig. 2.2 shows the solution derived by Greenwood and Johnson (Eq. 2.9) together with the exact solution given by Eq. 2.8.

From this figure it is observed that:

- Despite its complexity, the exact solution (Eq. 2.8) is almost linear for $0 < \delta < 0.5$ and follows closely the approximate linear solution by Greenwood and Johnson (Eq. 2.9). Surprisingly, Greenwood and Johnsons's solution (Eq. 2.9) coincides much beyond its nominal range of validity (i.e. $\alpha << 1$) with the exact solution (Eq. 2.8). This fortuitous agreement results from the quasi-linear nature of Eq. 2.8 up to $\alpha \approx 0.4$.
- The value of δ given by Eq. 2.8 and its slope at the origin are respectively:

$$\lim_{\alpha \to 0} \delta = 0 \tag{2.10}$$

$$\lim_{\alpha \to 0} \frac{d\delta}{d\alpha} = \frac{6}{5} \tag{2.11}$$

  as determined by series expansion. As expected, these values correspond to those predicted by Greenwood and Johnson (Eq. 2.9).
- The strains predicted by Eq. 2.8 diverge towards values larger than those extrapolated from Eq. 2.9 when the applied stress approaches the yield stress. As expected for a perfectly plastic material, the strain becomes infinite when the applied stress tends to the yield stress:

$$\lim_{\alpha \to \infty} \delta = 1 \tag{2.12}$$

  This equation was proven by using L'Hospital rule.

2.3 Discussion

While the above solution (Eq. 2.8) is the same as that found by Fischer [30], it is based only on the original assumptions made by Greenwood and Johnson and does not necessitate any further hypothesis. Thus, the radial strain components introduced by Mitter [58] and Fischer [30], do not affect the final result.

2.3.1 Transformation Superplasticity

Fig. 2.3 shows the total strain per cycle as a function of the applied stress for experimental literature data of iron, together with predictions by Eq. 2.8. Fitting was done by keeping the volumetric mismatch constant at $\Delta V/V = 1.05\%$ [8], while changing the yield stress systematically until the sum of the squared differences between applied and calculated stress was minimum:

$$\sum_{i=1}^{n}\left[\sigma_i - \sigma_Y \cdot \delta_i\right]^2 = \min \tag{2.13}$$

where n is the number of points measured. In Fig. 2.3, we assume that the strain of a full α-γ-α transformation cycle is the sum of two equal half-cycle contributions (α-γ and γ-α respectively):

$$\Delta\varepsilon_{tot} = 2 \cdot \varepsilon \tag{2.14}$$

As shown in Fig. 2.3, there is good agreement between experiment and model for the data by Greenwood and Johnson [39] with a yield stress $\sigma_Y = 7.4$ MPa and the data by Clinard and Sherby [17] with $\sigma_Y = 7.8$ MPa. However, the data of de Jong and Rathenau [20] and Zwigl and Dunand [108] cannot be fitted with the single parameter σ_Y (Eq. 2.13). This is because in Eq. 2.8 the yield stress affects not only the non-linear behavior of the ε-σ curve but also the value of the slope in the linear region. Fitting only the data in the linear range gives yield stresses of 16 MPa and 11 MPa for the data by de Jong and Rathenau [20] and Zwigl and Dunand [108], respectively. In Fig. 2.3, the predicted curves however diverge at stress values which are too low; this behavior is attributed to strain hardening, as discussed in the following.

Table 2.1 summarizes the chemical composition of samples used by the different investigators and shows that the yield stress, σ_Y, as determined from fitting of the experimental data, tends to increase with decreasing overall purity. Furthermore, the

impurity content also affects the post-yield behavior. The higher purity data by Greenwood and Johnson [39] and by Clinard and Sherby [17] can accurately be described as ideally plastic (Fig. 2.3), a central assumption of the models. However, samples used by de Jong and Rathenau [20] and Zwigl and Dunand [108] contained 0.2% carbon and 0.3% oxygen, respectively. These impurity levels are much higher than the solubility limit, so that the resulting iron carbides and oxides, respectively, are likely to affect the plastic behavior of the matrix by increasing both the yield stress and the post-yield strain hardening rate. Strain-hardening results in yield stresses σ_Y^* after plastic deformation which are higher than the initial yield stress σ_Y. This behavior can be modeled with a simple stress criterion:

$$\sigma_Y^* = \begin{cases} \sigma_Y & \text{for} \quad \sigma < \sigma_t \\ \sigma_Y + k \cdot (\sigma - \sigma_t) & \text{for} \quad \sigma \geq \sigma_t \end{cases} \tag{2.15}$$

where σ_t is a threshold stress and k is a parameter controlling the hardening rate. Table 2.1 shows these optimized parameters with the threshold stress, σ_t, set as half the initial yield stress, σ_Y, determined from Eq. 2.13 and shown in Fig. 2.3. Eq. 2.15 thus only contains two fitting parameters, i.e., σ_Y and k. With σ_Y given by the fitting in the linear range, k is obtained by fulfilling the condition:

$$\sum_{i=1}^{n} \left[\sigma_i - \sigma_Y^* \cdot \delta_i \right]^2 = \min \tag{2.16}$$

Optimal values for k are given in Table 2.1. The validity of the analytical model (Eq. 2.8) with and without strain hardening is tested by plotting the normalized stress δ (with σ_Y given by Eq. 2.15 and parameters taken from Table 2.1) vs. the normalized strain α (with ε given by Eq. 2.14). The result is shown in Fig. 2.4 together with the prediction of Eq. 2.8. Given the uncertainties of the purities of the materials and differences in the cycling parameters, i.e., frequencies and temperature amplitudes, the model is in good agreement with the experimental observations.

2.3.2 CTE-Mismatch Superplasticity

Eq. 2.8 can be adapted to describe superplasticity resulting from other mismatch mechanisms, e.g., martensitic phase transformations [34,74], irradiation swelling [77], compressibility mismatch [43] and CTE-mismatch [27]. The latter mechanism is discussed in the following, first for pure metals with anisotropic CTE, and second for metal matrix composites with inhomogeneous CTE. The treatment developed by Greenwood and Johnson [39] can be generalized to describe mismatch superplasticity by replacing the phase transformation strain tensor ε_{ij}^{T} (Eq. A6) with a general mismatch strain tensor ε_{ij}^{M}. The internal strains (Eq. A4) then become:

$$\varepsilon_{ij} = \varepsilon_{ij}^{P} + \varepsilon_{ij}^{M} \tag{2.17}$$

From the strain invariants, defined by the principal axes of the ε_{ij}^{M} tensor [23], it follows:

$$\left(\varepsilon_{xx}^{M}\right)^2 + \left(\varepsilon_{yy}^{M}\right)^2 + \left(\varepsilon_{zz}^{M}\right)^2 + 2\cdot\left[\left(\varepsilon_{xxy}^{M}\right)^2 + \left(\varepsilon_{xz}^{M}\right)^2 + \left(\varepsilon_{yz}^{M}\right)^2\right] = \frac{2}{3}\cdot\left(\frac{\Delta V}{V}\right)_{eq}^{2} \tag{2.18}$$

where $(\Delta V/V)_{eq}$ is the equivalent mismatch strain producing the internal stresses. Once the equivalent mismatch strain is specified, the derivation follows that of phase transformation plasticity presented in Appendix A, using Eq. 2.17 instead of Eq. A4. The final result is again Eq. 2.8 where α is now defined $\varepsilon/(\Delta V/V)_{eq.}$

The equivalent mismatch produced by CTE-mismatch mechanisms is of the general form:

$$\left(\frac{\Delta V}{V}\right)_{eq} = G(f)\cdot\int_{\Delta T_{pl}}\Delta\alpha\cdot dT \tag{2.19}$$

where *G(f)* describes the dependence of the volume fraction for the case of composite CTE-mismatch (G = 1 for a single phase anisotropic material), $\Delta\alpha$ is the thermal expansion mismatch between the composite phases (respectively, between crystallographic directions) and ΔT_{pl} is the temperature interval which causes plasticity beyond the elastic regime. ΔT_{pl},

which is smaller than the total temperature amplitude ΔT, is a function of the CTE mismatch, the elastic modulus and the yield stress of the weaker phase. Because these properties are temperature dependent, different values for ΔT_{pl} and thus $(\Delta V/V)_{eq}$ are expected for heating and cooling half-cycles, resulting in different values of half cycle plastic strains ε. While it is possible to use Eq. 2.8 separately for heating and cooling half-cycles, the model can also be used with cycle-averaged values for the yield stress and ΔT_{pl}, thus assuming equal contributions for the plastic strains caused by heating and cooling. This approximate approach must be followed when analyzing strain data reported only for complete temperature cycles. In this case, Eq. 2.19 can be simplified:

$$\left(\frac{\Delta V}{V}\right)_{eq} = K \cdot G(f) \cdot \overline{\Delta\alpha} \cdot \overline{\Delta T_{pl}} \tag{2.20}$$

where K is a parameter correcting for the errors introduced by taking cycle-average values for the thermal mismatch $\overline{\Delta\alpha} \cdot \overline{\Delta T_{pl}}$. Thus, the closer K is to unity the better the assumptions made for $\overline{\Delta\alpha} \cdot \overline{\Delta T_{pl}}$ are.

2.3.3 Anisotropic CTE-Mismatch Superplasticity in Pure Metals

Internal stress superplasticity can be induced upon thermal cycling of a polycrystalline material with anisotropic CTE, as reported for α-uranium [54,101] and zinc [72,101]. Following the derivation of Young et. al. [103], the strain deviators of an anisotropic material in a cartesian coordinate system, $\varepsilon^{M}_{x,y,z}$ are:

$$\varepsilon^{M}_{x} = K_1 \cdot \overline{\Delta T_{pl}} \cdot (\alpha_1 - \alpha_{av}) \tag{2.21}$$

$$\varepsilon^{M}_{y} = K_1 \cdot \overline{\Delta T_{pl}} \cdot (\alpha_2 - \alpha_{av}) \tag{2.22}$$

$$\varepsilon^{M}_{z} = K_1 \cdot \overline{\Delta T_{pl}} \cdot (\alpha_3 - \alpha_{av}) \tag{2.23}$$

where α_1, α_2, α_3 are the CTE's along the crystallographic directions (which are in general temperature dependent), $\alpha_{av} = (1/3)(\alpha_1 + \alpha_2 + \alpha_3)$ is the average CTE of an aggregate of randomly oriented grains, and K_1 is the correction parameter. Equations 2.21-2.23 are equivalent to Eqs. A7-A9, given by Greenwood and Johnson [39] for transformation superplasticity. For the special cases of α-uranium and zinc, $\alpha_1 \approx \alpha_2 = \alpha_3$ [94], so that Eqs. 2.21 to 2.23 become:

$$\varepsilon_x^M = (1/3) \cdot K_1 \cdot \overline{\Delta\alpha_m} \cdot \overline{\Delta T_{pl}} \tag{2.24}$$

$$\varepsilon_y^M = (1/3) \cdot K_1 \cdot \overline{\Delta\alpha_m} \cdot \overline{\Delta T_{pl}} \tag{2.25}$$

$$\varepsilon_z^M = (-2/3) \cdot K_1 \cdot \overline{\Delta\alpha_m} \cdot \overline{\Delta T_{pl}} \tag{2.26}$$

where $\overline{\Delta\alpha_m}$ is the temperature-averaged difference between α_1 and α_3. When comparing Eqs. 2.24-2.26 to A7-A9, the equivalent mismatch for the case of anisotropic CTE-mismatch plasticity is:

$$\left(\frac{\Delta V}{V}\right)_{eq} = K_1 \cdot \overline{\Delta\alpha_m} \cdot \overline{\Delta T_{pl}} \tag{2.27}$$

The parameter K_1 can be found from Eq. 2.27 from the experimental values for $\overline{\Delta T_{pl}}$ the average CTE $\overline{\Delta\alpha_m}$ and the equivalent mismatch $(\Delta V/V)_{eq}$ determined by fitting Eq. 2.8 to the data with the algorithm given in Eq. 2.13. The squared residuals are minimized iteratively by keeping σ_Y constant while locating the minimum for $\overline{\Delta\alpha}$, through changes of $(\Delta V/V)_{eq}$ and vice versa until convergence. If $\overline{\Delta T_{pl}}$ is unknown, the total cycle amplitude ΔT can be used as an upper bound $\overline{\Delta T_{pl}}$, thereby neglecting elastic strains. Figure 2.5 shows literature data for α-uranium [54] and zinc [72] together with model predictions by Eq. 2.8 fitted with the parameters given in Table 2.2. Our model (Eq. 2.8) successfully describes both the linear and the non-linear region of experimental data and gives two fitted parameters, σ_Y and $(\Delta V/V)_{eq}$, that are discussed in the following.

Lobb et. al. [54] showed that the strain rates of α-uranium cycled between 400°C and 600°C (T/T_m = 0.48-0.62) are significantly higher compared to the rates of isothermal creep at 600°C. Thus, plastic accommodation is by time-independent yield rather than by creep and the present model is applicable.

With an average CTE-mismatch of $\overline{\Delta\alpha_m} = 55.2 \cdot 10^{-6} K^{-1}$ between 400°C and 600°C [94] and a temperature amplitude ΔT = 200 K (an upper bound for $\overline{\Delta T_{pl}}$) a maximum mismatch of $\overline{\Delta\alpha_m} \cdot \Delta T = 1.1\%$ is calculated, giving a reasonable value of 0.24 for the parameter K_1. The value obtained for the yield stress (σ_Y = 36 MPa) is also reasonable in view of the yield stresses reported at 400°C (σ_Y = 120 MPa) and at 600°C (σ_Y = 20 MPa) [85].

The zinc data shown in Fig. 2.5 was measured by Pickard and Derby [72] on high purity wrought zinc and the same material after annealing at 350°C. Temperature cycles were between 60°C and 150°C (T/T_m = 0.48 - 0.61) and at all temperatures, the strain rates caused by thermal cycling are significantly higher than the isothermal creep rates calculated from Ref. [31]. The fitted average yield stress of the wrought material is 26.5 MPa, below the room temperature value of 33 MPa measured by Pickard and Derby [72], as expected from the negative temperature dependence of the yield stress. The annealed zinc is best fitted with a yield stress of 9.5 MPa. This value is much lower than that for the wrought material (26.5 MPa), as expected from recovery and recrystallization after annealing at a very high homologous temperature (T/T_m = 0.90). With $\overline{\Delta\alpha_m} = 46.8 \cdot 10^{-6}\ K^{-1}$ [94] the maximum available mismatch $\overline{\Delta\alpha_m} \cdot \Delta T = 0.42\%$, leading to values for K_1 of 0.21 and 0.17, which are similar to that of α-uranium K_1 = 0.24). The similarity in the values of K_1, while possibly fortuitous, is encouraging.

2.3.4 Composite CTE-Mismatch Superplasticity

Composites containing phases with different CTE's also exhibit mismatch superplasticity [27]. At low homologous temperatures where yield is the controlling deformation

mechanism, the present model (Eq. 2.8) can be used by fitting the yield stress and the equivalent volumetric mismatch. For CTE-mismatch superplasticity in composites, the strain deviators are:

$$\varepsilon_x^M = K_2 \cdot G(f) \cdot \overline{\Delta\alpha \cdot \Delta T_{pl}} \tag{2.28}$$

$$\varepsilon_y^M = K_2 \cdot G(f) \cdot \overline{\Delta\alpha \cdot \Delta T_{pl}} \tag{2.29}$$

$$\varepsilon_z^M = -2 \cdot K_2 \cdot G(f) \cdot \overline{\Delta\alpha \cdot \Delta T_{pl}} \tag{2.30}$$

where $\overline{\Delta\alpha}$ is the temperature-averaged linear mismatch between the CTE's of reinforcement and matrix, $\overline{\Delta T_{pl}}$ the temperature difference causing plastic deformation, $G(f)$ a function of the reinforcement volume fraction f and K_2 the correction parameter incorporating the non-ideality of the assumptions made above. Comparing Eqs. 2.28-2.30 to Eqs. A7-A9, the equivalent mismatch for composite CTE-mismatch superplasticity becomes:

$$\left(\frac{\Delta V}{V}\right)_{eq} = 3 \cdot G(f) \cdot K_2 \cdot \overline{\Delta\alpha} \cdot \overline{\Delta T_{pl}} \tag{2.31}$$

Fig. 2.6 shows the data and fits for Al/SiC metal matrix composites from Chen et. al. [15] and Pickard and Derby [71]. Chen et. al. [15] cycled a 2124 Al composite containing 20 vol.% SiC whiskers between 100°C and 350°C (T/T_m = 0.400.67) and showed that the strain rates caused by thermal cycling are more than an order of magnitude higher than isothermal creep at a homologous temperature of 0.69. Pickard and Derby [71] used composites containing 20 vol.% and 30 vol.% 2.3 μm SiC particulates with a matrix of commercially pure aluminum, for which plasticity by creep was also insignificant over the cycling temperature range between 130°C and 350°C (T/T_m = 0.43-0.67). Thus the composite behavior upon thermal cycling is controlled by time-independent yield and can be described by Eq. 2.8 with $(\Delta V/V)_{eq}$ given by Eq. 2.31. The fitted values for σ_Y and $(\Delta V/V)_{eq}$ are given in Table 2.2.

Table 2.2 shows that the yield stress is significantly higher for the composite with an alloyed 2124 matrix than for the pure aluminum composite. This effect is expected both because the alloy is stronger than the pure metal and because whiskers typically strain harden a metallic matrix more effectively than particulates. Also, Pickard and Derby [71] measured the yield stress of the commercially pure aluminum matrix as a function of the temperature, giving a cycle-averaged yield stress of 20.5 MPa, in reasonable agreement with our fitted values of 26 MPa for the 20 vol.% SiC_p composite and 26.5 MPa for the 30 vol.% SiC_p.

The dependence of the volume fraction was modeled by Pickard and Derby [71] as $G(f) = (1f)f$. Furthermore, they independently measured the temperature amplitude ΔT_{el} for the onset of plasticity. By taking $\overline{\Delta\alpha_m} = 22.7 \cdot 10^{-6}\ K^{-1}$ [94] and an average value for heating and cooling $\overline{\Delta T_{el}} = 137$ K (i.e., $\overline{\Delta T_{pl}} = \Delta T - \overline{\Delta T_{el}} = 83$ K, the mismatch strains are $3 \cdot G(f) \cdot \overline{\Delta\alpha_m} \cdot \overline{\Delta T_{pl}} = 0.030\%$ and 0.040% for the 20 vol.% and 30 vol.% SiC_p composite, respectively. Using the fitted values for $(\Delta V/V)_{eq}$ given in Table 2.2, K_2 values of 2.7 and 1.6 are obtained respectively from Eq. 2.31. Assuming the same value for $\Delta T_{el} = 137$ K, the mismatch strain of the 2124 Al composite becomes 0.041% and $K_2 = 0.46$. While K_2 values are similar for the two pure aluminum composites, the value for K_2 for the alloyed composite is significantly lower, possibly because (i) the yield stress of the 2124 alloy is much higher than for pure aluminum, thus increasing ΔT_{el}, (ii) whiskers produce a mismatch stress field different from that of equiaxed particulates. In general, the values for the correcting parameters K_1 and K_2 determined for anisotropic CTE-mismatch and composite mismatch superplasticity are, respectively within factors 6 and 3, of the predicted ideal value of unity. We believe that this error can be explained by the assumptions and approximations made for the equivalent mismatch (Eq. 2.20).

2.4 Conclusions

Allotropic materials deforming by transformation superplasticity exhibit at low applied stresses a linear relationship between plastic strain per transformation and the applied stress, as predicted by the linear relationship of Greenwood and Johnson [39]. However, at intermediate and high applied stresses, where their theory becomes invalid, experimental data show that the strain increases non-linearly with the applied stress. We generalize the original theory of Greenwood and Johnson [39] to include these stress regimes and derive a closed-form solution valid for all applied stresses (from zero up to the yield stress of the weaker phase) for an ideally plastic material. As expected, the strains predicted by the complete solution converge to the linear expression by Greenwood and Johnson [39] at low stresses and diverge to infinity for stresses tending towards the yield stress. The complete solution accurately describes data for high-purity iron in both these linear and non-linear regions. The model is then extended to the case of a strain-hardening material and applied successfully to literature data for iron with high impurity content. Finally, the model is adapted to the more complex case of CTE-mismatch superplasticity exhibited by metals with anisotropic CTE and by composites with inhomogeneous CTE. Experimental literature data on α-uranium, zinc and Al/SiC composites are successfully described with two fitting parameters (yield stress and thermal mismatch) which take values that are physically reasonable.

Appendix A

Summary of the Derivation by Greenwood and Johnson [39]

Phase transformation superplasticity is attributed to the presence of deviatoric stresses $\sigma'_{ij} = \sigma_{ij} - (1/3)\delta_{ij}\sigma_{kk}$ where σ_{ij} are the stress tensor components, σ_{kk} its hydrostatic components and δ_{ij} the Kronecker symbol. The kinetics of strain production is modeled as

$$\dot{\varepsilon}_{ij} = \sigma'_{ij}\lambda \tag{A1}$$

where $\dot{\varepsilon}_{ij}$ are the internal strain rate components and λ is the viscosity of the weaker phase once the yield stress is reached. Assuming that the rate of production of the internal stress is fast compared to any possible relaxation mechanism, Eq. A1 can be integrated over the time of transformation Δt to give:

$$\varepsilon_{ij} = \sigma'_{ij}\lambda_1 \tag{A2}$$

where $\lambda_1 = \lambda\Delta t$ is a constant. The internal strain components ε_{ij} are only a function of the deviatoric stress components. Substituting Eq. A2 into the Lévy-Von Mises yield criterion (which relates the deviatoric stress components to the yield stress, σ_Y, as measured in uniaxial tension) gives:

$$\varepsilon_{xx}^2 + \varepsilon_{yy}^2 + \varepsilon_{zz}^2 + 2\cdot\varepsilon_{xy}^2 + 2\cdot\varepsilon_{yz}^2 + 2\cdot\varepsilon_{xz}^2 = (2/3)\cdot\lambda_1^2\cdot\sigma_Y^2 \tag{A3}$$

The internal strains are obtained by superimposing the strains due to plastic deformation of the weaker phase, ε_{ij}^P and the strains associated with the phase transformation, ε_{ij}^T:

$$\varepsilon_{ij} = \varepsilon_{ij}^P + \varepsilon_{ij}^T \tag{A4}$$

with

$$\varepsilon_{ij}^{P} = \begin{bmatrix} -\frac{1}{2}\cdot\varepsilon & 0 & 0 \\ 0 & -\frac{1}{2}\cdot\varepsilon & 0 \\ 0 & 0 & \varepsilon \end{bmatrix} \tag{A5}$$

$$\varepsilon_{ij}^{T} = \begin{bmatrix} (\Delta V/V)_{xx} & (\Delta V/V)_{xy} & (\Delta V/V)_{xz} \\ (\Delta V/V)_{xy} & (\Delta V/V)_{yy} & (\Delta V/V)_{zy} \\ (\Delta V/V)_{xz} & (\Delta V/V)_{zy} & (\Delta V/V)_{zz} \end{bmatrix} \tag{A6}$$

where ε is the plastic strain increment in the direction of the uniaxial applied stress and $(\Delta V/V)_{ij}$ the components of the phase transformation strain tensor. The negative sign in Eq. A6 indicates that a volume reduction occurs during the phase transformation. Greenwood and Johnson [39] followed Anderson and Bishop [4] by assuming that the strain $(\Delta V/V)_{x,y,z}$ in principal coordinates are:

$$(\Delta V/V)_x = (1/3)\cdot(\Delta V/V) \tag{A7}$$

$$(\Delta V/V)_y = (1/3)\cdot(\Delta V/V) \tag{A8}$$

$$(\Delta V/V)_z = (-2/3)\cdot(\Delta V/V) \tag{A9}$$

The components of the transformation strain tensor (Eq. A6) are related to the principal strain deviators (Eqs. A7-A9) by a coordinate transformation, e.g.:

$$\begin{aligned}(\Delta V/V)_{zz} = {} & (\Delta V/V)_x\cdot\cos(\varphi)^2\cdot\sin(\vartheta)^2 + \\ & (\Delta V/V)_y\,\sin(\varphi)^2\cdot\sin(\vartheta)^2 + (\Delta V/V)_z\cdot\cos(\vartheta)^2\end{aligned} \tag{A10}$$

Using Eqs. A7-A9 and Eq. A10, the second invariant of the transformation tensor (Eq. A6) is:

$$(\Delta V/V)_{xx}^2 + (\Delta V/V)_{yy}^2 + (\Delta V/V)_{zz}^2 + 2\cdot\left[(\Delta V/V)_{xy}^2 + (\Delta V/V)_{yz}^2 + (\Delta V/V)_{xz}^2\right] = (2/3)\cdot\left(\frac{\Delta V}{V}\right)^2 \quad \text{(A11)}$$

Further, the first invariant of the phase transformation strain tensor requires that:

$$(\Delta V/V)_{xx} + (\Delta V/V)_{yy} + (\Delta V/V)_{zz} = 0 \quad \text{(A12)}$$

Introducing Eq. A4 into Eq. A3 and using Eqs. A11 and A12 gives:

$$(3/2)\cdot\varepsilon^2 - 3\cdot\varepsilon\cdot(\Delta V/V)_{zz} + (2/3)\cdot(\Delta V/V)^2 = (2/3)\cdot\lambda_1^2\cdot\sigma_Y^2 \quad \text{(A13)}$$

Compatibility of strains in the z-direction (i.e., the direction of the uniaxial applied stress) requires that:

$$\varepsilon_{zz} = \varepsilon - (\Delta V/V)_{zz} \quad \text{(A14)}$$

After introducing Eqs. A2 and A14 into Eq. A13, eliminating λ_1 and rearranging terms, the deviatoric stress component in the z-direction is given by:

$$\sigma'_{zz} = \frac{\sigma_Y\cdot\left[\varepsilon - (\Delta V/V)_{zz}\right]}{(\Delta V/V)\cdot\left[1 + \frac{9\cdot\varepsilon^2}{4\cdot(\Delta V/V)^2} - \frac{9\cdot\varepsilon\cdot(\Delta V/V)_{zz}}{2\cdot(\Delta V/V)^2}\right]^{1/2}} \quad \text{(A15)}$$

This is equation (7) of Greenwood and Johnson's article [39]. Under the assumption that $\varepsilon << \Delta V/V$ these authors make three approximations by

- neglecting the ε^2 term in the denominator of Eq. A15,
- expanding $(1 - x)^{-1/2} \approx 1 + x/2$, where $x = [9\cdot\varepsilon\cdot(\Delta V/V)_{zz}]/[2\cdot(\Delta V/V)^2]$
- neglecting again the ε^2 term to obtain:

$$\sigma'_{zz} \approx \frac{\sigma_Y \cdot \left[\varepsilon \cdot \left(1 - \frac{9 \cdot (\Delta V / V)^2_{zz}}{4 \cdot (\Delta V / V)^2} \right) - (\Delta V / V)_{zz} \right]}{(\Delta V / V)} \tag{A16}$$

$$\frac{\int \sigma'_{zz} d\Omega}{\int d\Omega} = \frac{2}{3} \cdot \sigma \tag{A17}$$

$$\frac{\int \left(\frac{\Delta V}{V}\right)^2_{zz} d\Omega}{\int d\Omega} = \frac{4}{45} \cdot \left(\frac{\Delta V}{V}\right)^2 \tag{A18}$$

$$\frac{\int \left(\frac{\Delta V}{V}\right)_{zz} d\Omega}{\int d\Omega} = 0 \tag{A19}$$

where σ is the applied stress in the z-direction. Introducing Eqs. A17 to into Eq. A19 leads to the concise result found by Greenwood and Johnson [39]:

$$\varepsilon \approx \frac{5}{6} \cdot \frac{\Delta V}{V} \cdot \frac{\sigma}{\sigma_Y} \tag{A20}$$

Figures of Chapter 2

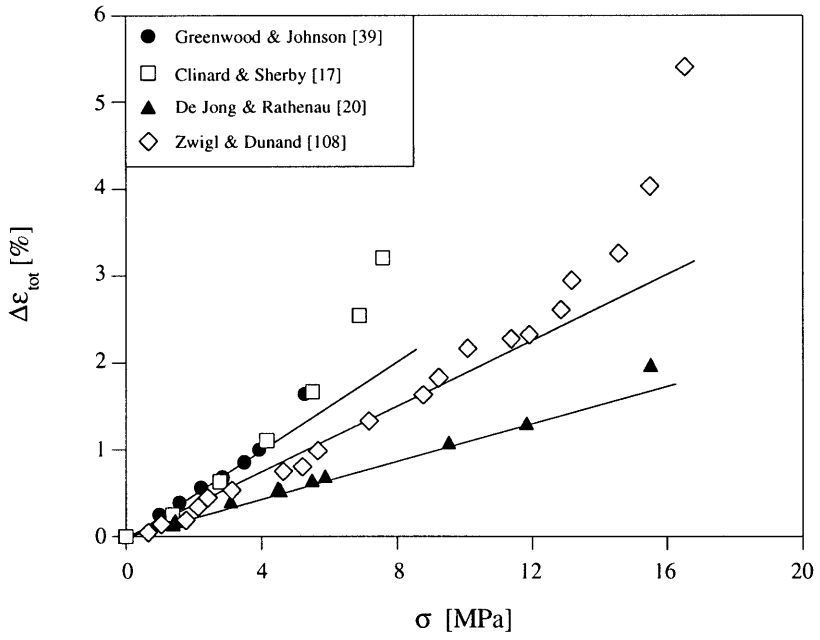

Figure 2.1: Strain per cycle as function of applied stress for iron with varying purity. Data by Clinard and Sherby [17] are creep-corrected.

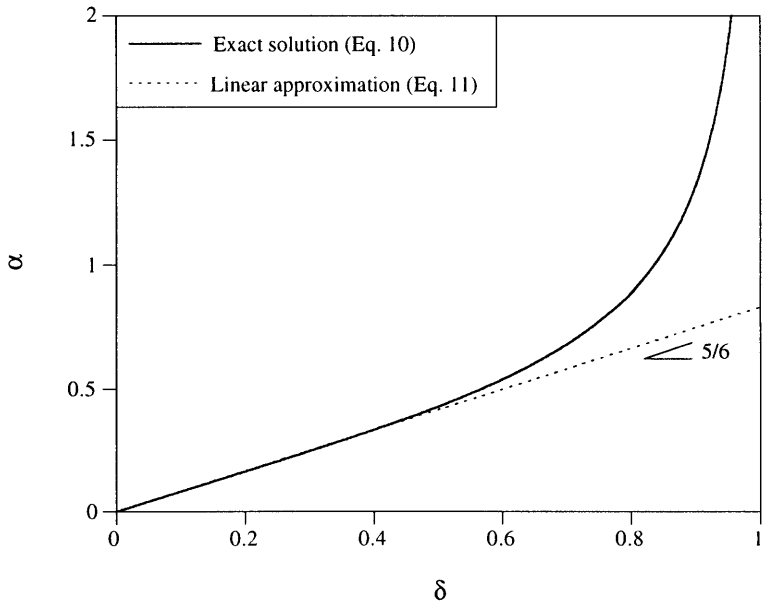

Figure 2.2: Dimensionless transformation strain as a function of dimensionless applied stress as predicted by Eq. 2.8 (exact solution) and Eq. 2.9 (approximate solution by Greenwood and Johnson [39]).

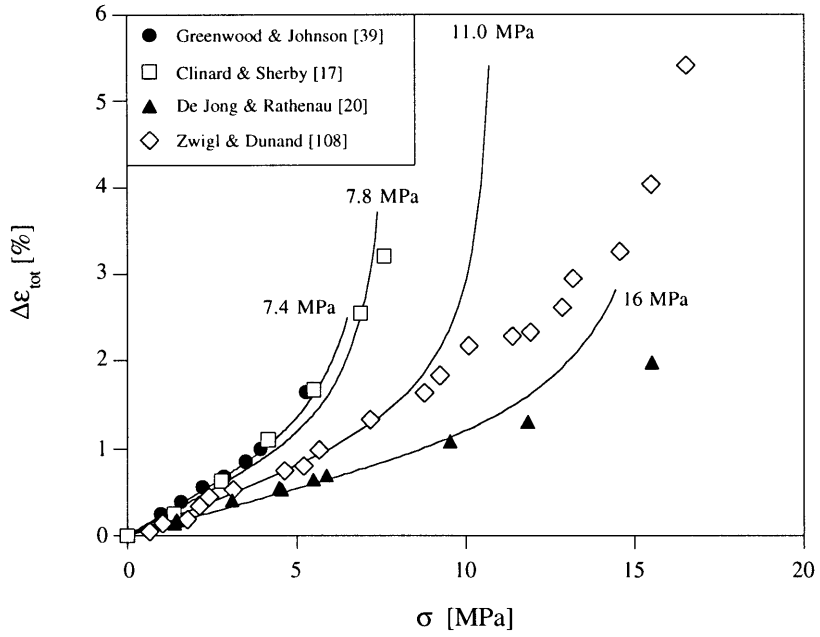

Figure 2.3: Total strain per cycle as a function of applied stress. Literature values (symbols) are compared to model prediction (line, Eq. 2.8) with σ_Y as a parameter given in the figure.

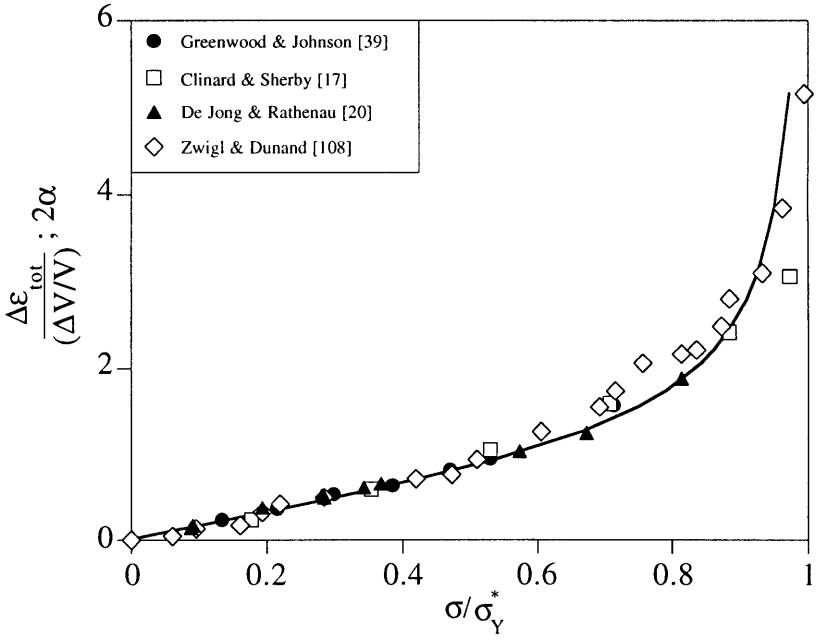

Figure 2.4: Total strain per cycle normalized by the transformation mismatch strain as a function of applied stress normalized by the yield stress (symbols). Theoretical solution (Eq. 2.8) is given by the line.

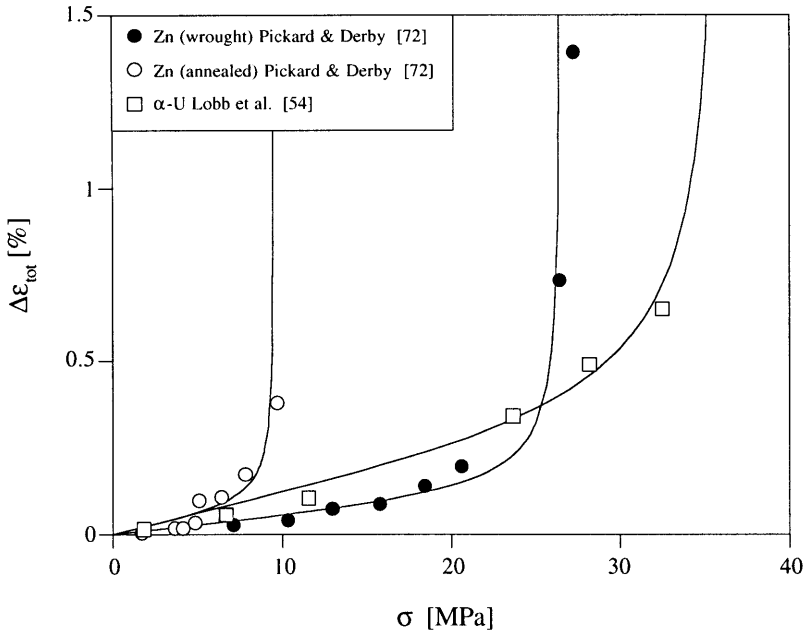

Figure 2.5: Total strain per cycle as a function of applied stress for anisotropic CTE-mismatch superplasticity of α-uranium [54] and zinc [72] (symbols) compared to model predictions by Eq. 2.8 (line) using parameters given in Table 2.2.

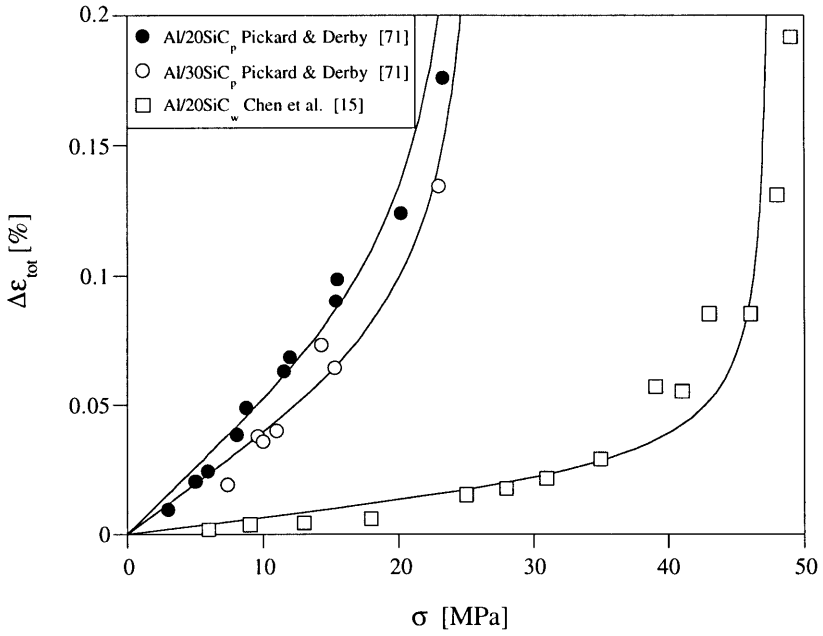

Figure 2.6: Total strain per cycle as a function of applied stress for composite CTE-mismatch superplasticity of Al/SiC composites [15,71] (symbols) compared to model predictions by Eq. 2.8 (line) using parameters given in Table 2.2.

Tables of Chapter 2

Table 2.1: Chemical composition and material parameters for the yield stress given by Eq. 2.15 for iron.

purity [wt.%]	main impurity [wt.%]	σ_Y [MPa]	k	σ_t [MPa]	Reference
~100	~0	7.4	0	0	[39]
99.7	0.02 C	7.8	0	0	[17]
99.7	0.3 O	11	0.51	5.5	[20]
~99.8	0.2 C	16	0.41	8	[108]

Table 2.2: Summary of material parameters used in CTE-mismatch superplasticity models.

Material	σ_Y [MPa]	$(\Delta V/V)_{eq}$ [%]	K_1 Eq. 2.27	K_2 Eq. 2.31	Reference
α-U	36.0	0.27	0.24	-	[54]
Zn-wrought	26.5	0.090	0.21	-	[72]
Zn-annealed	9.5	0.070	0.17	-	[72]
2124 Al/20SiC$_w$	47.5	0.019	-	0.46	[15]
pure Al/20SiC$_p$	26.0	0.082	-	2.7	[71]
pure Al/30SiC$_p$	26.5	0.063	-	1.6	[71]

Chapter 3

A Numerical Model of Transformation-Superplasticity for Iron

Abstract

A numerical model of transformation superplasticity for an elastic, ideally plastic material is presented using a plane-strain formulation considering both temperature and displacement. The evolution of temperature, stresses and strains during the ferrite-austenite phase transformation of iron is computed for different values of the applied stress. For low stresses, the numerical model predicts a linear relationship between the applied stress and the plastic strain increment accumulated after crossing the phase transformation range. For high stresses, the relationship becomes non-linear: the strain increments tend to infinity as the applied stress approaches the yield stress. Both these trends are in qualitative agreement with analytical solutions for transformation superplasticity. Furthermore, upon introducing plane-strain specific equivalent quantities for the transformation mismatch and the yield stress, the numerical model is in good quantitative agreement with both analytical predictions and experimental data for pure iron.

3.1 Introduction

Transformation superplasticity is a deformation mechanism relying on the biasing by an externally applied stress of isotropic internal mismatch stresses or strains induced during the phase transformation of allotropic polycrystalline materials. Plastic deformation of the weaker phase due to the internal and external stresses controls the macroscopic strain increment developed during the allotropic transformation. As internal stresses are regenerated each time the material transforms, large superplastic strains can result by accumulation of the individual strain increments produced during cycling about the allotropic temperature, as reviewed in e.g. Refs. [25,29,60,68].

For elastic, ideally-plastic materials, Greenwood and Johnson [39] derived an approximate analytical solution for the uniaxial strain increment $\Delta\varepsilon$ accumulated during a full temperature cycle (where the allotropic temperature is crossed twice), as a function of the absolute value of the volume mismatch between the two allotropic phases $\Delta V/V$, the externally applied uniaxial stress σ and the uniaxial yield stress σ_y of the weaker phase:

$$\Delta\varepsilon \sim \frac{5}{3}\frac{\Delta V}{V}\frac{\sigma}{\sigma_Y} \tag{3.1}$$

However, Eq. 3.1 is valid only for applied stresses which are small compared to the yield stress. Based on Greenwood and Johnson's derivation, Refs. [30,107] extended the model for all applied stresses below the yield stress:

$$\delta = \frac{1}{4} + \frac{1}{6\alpha} + \frac{1}{2\sqrt{2\alpha}}\left(\frac{3\alpha}{4} - \frac{1}{6} - \frac{1}{9\alpha}\right)\ln\left[\frac{\left(3\alpha + 3\sqrt{2\alpha} + 2\right)^2}{9\alpha^2 - 6\alpha + 4}\right] \tag{3.2}$$

where the dimensionless parameters δ and α are defined as σ/σ_y and $(\Delta\varepsilon/2)/(\Delta V/V)$, respectively. Equation 3.2 was found to be in good agreement with experimental data for pure iron undergoing the α/γ transformation without strain-hardening [107,109]. As

expected, Eq. 3.2 tends toward the limit for small stresses (Eq. (3.1)) expressed in dimensionless manner for half a temperature cycle as:

$$\alpha \sim \frac{5}{6}\delta. \tag{3.3}$$

While the closed-form solution Eq. 3.2 is compact and predictive, it does not give any information on the time-evolution of internal stresses, internal strains, or macroscopic strain during the allotropic transformation. Such information can however be generated by finite-element models, which can also take into account the temperature-dependence of the thermo-mechanical properties during thermal cycling and the coupling between thermal and mechanical behavior of the material. Finite-element modeling has been used to study the related problems of thermal mismatch superplasticity in Al/SiC composites during thermal cycling [105,106], and transformation plasticity in steel due to the formation of pearlite [33] or martensite [21,35,52,76].

In the present chapter, we introduce a plane-strain finite-element model with thermal-mechanical coupling describing an elastic, ideally-plastic material undergoing an allotropic phase transformation under an externally applied stress. Numerical results for the transformation superplasticity of iron are compared to the predictions of the analytical model given by Eq. 3.2 and experimental results by Refs. [17,39]. Further, the consistency of the numerical model with respect to changes of the yield stress and the volume mismatch is tested and the time-dependence of stresses and strains are discussed.

3.2 Model

The numerical model consists of 16 plane-strain, temperature-displacement elements [41] regularly arranged in a square 4x4 mesh with a length L_0 = 100 μm as shown in Fig. 3.1. The boundary- and symmetry conditions are defined such that the mesh remains rectangular throughout the analysis. The initial temperature of the stress-free domain was set to T =

909°C. Defining the 3-direction as being constrained by plane-strain (i.e. $\varepsilon_{33} = 0$), an external uniaxial stress σ_{22} (referred to as σ in the following) is applied along the a-a edge in the first step of the analysis. In the following steps, a square temperature profile (Fig. 3.1) is repeatedly applied along the b-b edge where the temperature is cycled between T_l = 909°C and T_u = 915°C about the ferrite-austenite α–γ allotropic range of iron, taken as 911.5 - 912.5°C. The time-incrementation during the transient temperature-displacement analysis (performed with ABAQUS version 5.5 [41]) is set so that the element strain is below $5 \cdot 10^{-4}$ and the temperature difference is below 0.2 K during each increment. Heat transport is assumed to occur by convection with a heat transfer coefficient h = 50 $W \cdot m^{-2} \cdot K^{-1}$. Consistent with the analytical model, isotropic macroscopic material properties are used to model the α–γ transformation of iron, as summarized in Table 3.1.

As shown in Fig. 3.2 for the thermal strain, the density change is modeled by varying the technical coefficient of thermal expansion $\alpha_{20°C}$ linearly over the allotropic temperature range between the values given in Table 1. The technical coefficient of thermal expansion includes the contraction due to the ferrite-austenite transformation with respect to room-temperature and thus has a smaller value for the austenite than for the ferrite. However, the instantaneous thermal expansion, defined as the slope of the extension/temperature curve, is higher for austenite than for ferrite. Using technical coefficients of thermal expansion, the allotropic length change is:

$$\frac{\Delta L}{L} = \left(\alpha_{20°C,\alpha} - \alpha_{20°C,\gamma}\right) \cdot \Delta T \tag{3.4}$$

With $\alpha_{20°C,\alpha}$, $\alpha_{20°C,\gamma}$ taken from Table 3.1, ΔT = 912°C - 20°C, Eq. 3.4 gives $\Delta L/L$ = 0.348%, corresponding to a volume change $(\Delta V/V) = 3 \cdot (\Delta L/L)$ = 1.04%, in agreement with the value reported in Ref. [8] for iron.

The yield stress of the weaker low-temperature ferrite is taken as σ_Y = 7.5 MPa, as determined from experimental transformation superplasticity data [107,109]. The yield

stress of the stronger austenite is assumed to be ten times higher than that of ferrite. Furthermore, it is assumed that the yield stress of the material is equal to that of ferrite throughout the transformation (i.e. over $\Delta T = 1K$), and that it increases rapidly to that of austenite immediately after the end of the phase transformation over a small temperature interval $\Delta T = 0.1K$, as shown in Fig. 3.2.

3.3 Results

Figure 3.3a shows the time-dependence of the strain ε_{22} (referred to as ε in the following) and the domain temperature during the first three thermal cycles for an applied stress $\sigma = 4.0$ MPa. The cycle period is $\Delta t = 240$ s, with equal intervals $\Delta t_{1/2} = 120$ s for heating and cooling. The temperature was determined at the upper right hand corner of the domain and thermal gradients within the material were below $\Delta T = 0.1$ K at all times. During the heating stage of the cycles, the temperature increases rapidly from T = 909°C to the onset of the phase transformation, modeled at T = 911.5°C. Because of the heat absorbed or released during the phase transformation, the heating and cooling rates are reduced when the material transforms (Fig. 3.3a).

A small thermal expansion is observed upon initial heating (Fig. 3.3b) before the domain shrinks over the phase transformation interval $\Delta T = 1K$. This large allotropic contraction is followed by a small thermal expansion (Fig. 3.3c) upon heating to the upper cycling temperature T = 915°C. On cooling, thermal contractions occur outside the phase transformation interval over which the material expands (Figs. 3.3c,d). An overall plastic strain increment in the 2-direction (referred to as $\Delta\varepsilon$ in the following) is observed after each full cycle. The magnitude of the strain increment, which was taken as the difference of plastic strains between the start and the end of a cycle, changes slightly between the first and the succeeding cycles, because of different residual stresses: at the onset of the first heating ramp, the material is free of residual stresses, but at the onset of the second and all

subsequent heating ramps, residual stresses exist in the material. The value of $\Delta\varepsilon$ remains unchanged after the first cycle.

Figure 3.4a shows the evolution of the Von Mises equivalent stress σ_{eq} and the plastic strain ε_{pl} in the 2-direction during the third temperature cycle of Fig. 3.3a. The Von Mises stress is calculated at the center of the upper right element of the mesh. The stress-field showed no gradients within the 16 elements so that the stress history of this element is representative of that of the whole domain. The plastic strain ε_{pl}, as determined from the deformation of the whole domain along the 2-direction, is obtained by subtraction of the total strains in the 2-direction with and without applied stress:

$$\varepsilon_{pl} = \varepsilon(t,\sigma) - \varepsilon(t,\sigma = 0) \ . \tag{3.5}$$

The initial thermal expansion (Fig. 3.3b) induces a stress increase (point (1) in Fig. 3.4b). The subsequent contraction (Fig. 3.3b) of the domain due to the α/γ transformation relaxes the thermal mismatch, causing first a reduction of the equivalent stress (point (2) in Fig. 3.4b) and then an increase to the yield stress (point (3) in Fig. 3.4b). The sharp drop of the equivalent stress between points (1) and (3) in Fig. 3.4b is due to the change of the σ_{33}-stress component from a compressive to a tensile state of stress. Up to that point, no plastic strains are produced. Point (3) in Fig. 3.4b marks the onset of plasticity, and yielding occurs until the end of the α/γ transformation (point (4) in Fig. 3.4a), causing an overall plastic strain increment $\Delta\varepsilon_{\alpha/\gamma}$ = 0.153%. Finally, upon heating to the upper cycle temperature, the equivalent stress is reduced to σ_{eq} = 5.0 MPa (because the thermal and allotropic strains are of opposite signs) with no associated plastic strain (point (5) in Fig. 3.4a). Because the yield stress of the austenite is never reached (except very briefly at point (4) and (6) in Fig. 3.4a), its exact value (taken arbitrarily as 10 times that of the ferrite) is unimportant. The cooling portion of the cycle shows qualitatively the same stress and strain behavior, giving a residual equivalent stress σ_{eq} = 5.5 MPa (point (7) in Fig. 3.4a) and $\Delta\varepsilon_{\gamma/\alpha}$

= 0.146%, so that the total uniaxial strain accumulated at the end of the cycle is $\Delta\varepsilon = \Delta\varepsilon_{\alpha/\gamma} + \Delta\varepsilon_{\gamma/\alpha} = 0.299\%$.

Figure 3.5 shows the steady-state strain increment in the 2-direction (i.e. $\Delta\varepsilon$ for the third temperature cycle) as a function of the applied stress. A linear relationship between the strain increment and the applied stress exists at low stresses, while progressively increasing strain increments are developed at high stress levels. Also, finite strain increments are obtained above the uniaxial yield stress σ_Y because of the plane-strain condition, as discussed later. When higher values are taken for the yield stress limits (σ_Y = 11 MPa for ferrite and σ_Y = 110 MPa for austenite), smaller strain increments are observed at low stresses and the divergence occurs at a higher stress.

To examine the sensitivity of the model to the value of the allotropic volume mismatch $\Delta V/V$, the technical coefficient of thermal expansion of the austenite was further varied, i.e. $\alpha_{20°C,\gamma} = \alpha_{20°C,\alpha} - (\Delta V/V)/(3\cdot\Delta T)$. Figure 3.6 shows the effect of the volume mismatch on the strain increment per cycle for applied stresses of σ = 4.0 MPa and σ = 8.0 MPa using a uniaxial yield stress of σ_Y = 7.5 MPa. The strain increment is proportional to the volume mismatch, with slopes $d(\Delta\varepsilon)/d(\Delta V/V) = 0.30$ and $d(\Delta\varepsilon)/d(\Delta V/V) = 1.35$ at the lower and higher applied stress, respectively.

3.4 Discussion

3.4.1 Temperature-, Strain- and Stress Evolution

The numerical results showed that thermal gradients were insignificant ($\Delta T < 0.1$ K) with the standard 16-element mesh (or with meshes containing 64 and 256 elements). This is consistent with the value much smaller than unity for the Biot number:

$$Bi = \frac{h \cdot L_0}{k} \tag{3.6}$$

where k is the thermal conductivity and L_0 is the domain length (Fig. 3.1): with values h = 50 $W \cdot m^{-2} \cdot K^{-1}$, k = 0.3 $W \cdot cm^{-1} \cdot K^{-1}$, L_0 = 100 μm, the Biot number is Bi = $1.7 \cdot 10^{-4}$. Under these thermal conditions, the time for transformation is:

$$\Delta t = \frac{L_0 \cdot \rho \cdot \Delta H}{h \cdot |T_S - T_P|}, \tag{3.7}$$

where T_S is the surface temperature (T_S = 915°C on heating and T_S = 909°C on cooling) and T_P is the phase transformation temperature. Since the phase transformation is modeled over a temperature interval ΔT = 1K, Eq. 3.7 is integrated between T_{P1} = 911.5°C (912.5°C) and T_{P2} = 912.5°C (911.5°C) for heating (cooling):

$$\Delta t = \frac{L_0 \cdot \rho \cdot \Delta H}{h \cdot |T_{P2} - T_{P1}|} \cdot \ln\left(\frac{T_{P1} - T_S}{T_{P2} - T_S}\right). \tag{3.8}$$

Taking an average density of ρ = 7.73 $g \cdot cm^{-3}$, the expected time for transformation from Eq. 3.8 is Δt = 97.8, close to the value found numerically (Δt = 102.4 s for Fig. 3.3a).

Based on the elastic responses ε_{el} of the domain upon initial application of a series of externally applied uniaxial stresses (e.g. Fig. 3.3b for σ = 4.0 MPa), the numerical elastic modulus for the ferrite at T = 909°C is E^* = 71.6 GPa, in good agreement with the expected value of the elastic modulus in plane-strain $E^* = E/(1 - \nu^2)$ = 71.5 GPa (where ν is the Poisson's ratio), using elastic constants given in Table 3.1.

The magnitudes of the thermal strains outside the phase transformation range (Fig. 3.3c,d) are small compared to transformation strains (Fig. 3.3a) so that thermal expansion mismatch plasticity can be excluded as a deformation mechanism. Furthermore, because the thermal and allotropic strains have opposite signs, the small thermal mismatch outside the transformation range reduces the allotropic mismatch produced during transformation.

As shown in Fig. 3.3a for an applied stress σ = 4.0 MPa, the sample shrinks in the 2-direction during heating through the transformation by $\Delta\varepsilon_h$ = - 0.370% and expands on

cooling by $\Delta\varepsilon_c = 0.669\%$, giving a strain increment over a whole cycle of $\Delta\varepsilon = \Delta\varepsilon_h + \Delta\varepsilon_c = 0.299\%$. The magnitude of $\Delta\varepsilon_h$ and $\Delta\varepsilon_c$ are different because on cooling the allotropic strain $\Delta L/L$ has the same sign as the plastic strain due to the applied stress, while on heating the strains have opposite signs. When no stress is applied, the uniaxial allotropic strains developed on heating and cooling in the 2-direction are equal and of opposite sign: $|\varepsilon_0| = 0.516\%$. This strain translates into a volume change $\Delta V/V = 2\cdot\varepsilon_0 = 1.032\%$ for plane-strain conditions, close to the allotropic volume mismatch ($\Delta V/V = 1.048\%$). Using Eq. 3.5 to determine the plastic strain, Fig. 3.4a shows that nearly equal plastic strain increments are developed during the transformation on heating ($\Delta\varepsilon_{\alpha/\gamma} = \Delta\varepsilon_h + \varepsilon_0 = 0.146\%$) and on cooling ($\Delta\varepsilon_{\gamma/\alpha} = \Delta\varepsilon_c - \varepsilon_0 = 0.153\%$). The small difference is probably due to the slight asymmetry of the temperature-dependence of the yield stress (Fig. 3.2). In the case of the α/γ transformation, the initial stress drop at the onset of the phase transformation (Fig. 3.4b) takes place while the material is in the weaker α-phase. For the γ/α transformation however, the stress drop coincides with the linear decrease of the yield stress from $\sigma_Y = 75$ MPa to $\sigma_Y = 7.5$ MPa.

Finally, the residual equivalent stress present after transformation is slightly higher on cooling ($\sigma_{eq} = 5.5$ MPa, point (7) in Fig. 3.4a) than on heating ($\sigma_{eq} = 5.0$ MPa, point (5) in Fig. 3.4a). Two mechanisms explain this effect. First, the physical thermal expansion of ferrite near the phase transformation is lower than that of austenite [3], so that the internal allotropic stresses present at the transformation are relaxed less by thermal contraction in the ferrite than by thermal expansion in the austenite. Second, since the elastic modulus of ferrite ($E_\alpha = 65.1$ GPa) is much lower than that of austenite ($E_\gamma = 117$ GPa), the internal stresses decrease less in the ferrite than in the austenite for the thermal strain relaxation occurring during the thermal excursion $\Delta T = 2.5$ K above and below the transformation range. The thermal stress relaxation along the 3-direction can be estimated using:

$$\Delta\sigma_{33} = E \cdot \alpha_{20^\circ C} \cdot \Delta T \qquad (3.9)$$

Eq. 3.9 gives $\Delta\sigma_{33}$ = 2.44 MPa on cooling and $\Delta\sigma_{33}$ = 3.24 MPa on heating, close to the numerical values $\Delta\sigma_{33}$ = 2.41 MPa and $\Delta\sigma_{33}$ = 3.09 MPa, respectively.

3.4.2 Model Discussion

The model is sensitive to the assumption made for the temperature-dependence of the yield stress during the transformation. The present results are for the specific case where plasticity occurs throughout the transformation range at the lowest yield stress of ferrite (Fig. 3.2). Physically, this is equivalent to plastic deformation being spatially localized in the weak ferrite until that phase disappears. The continuum approach taken in the numerical model approximates this spatially inhomogeneous behavior by assuming that the whole domain yields at the yield stress of the ferrite. If instead a rule of mixture is used for the yield stress, much reduced plasticity is found.

The nature of the mismatch needs to be examined, since the numerical model with coupled thermal-mechanical elements allows for two possible types of mismatch. First, internal mismatch stresses are produced by the constraining effect in the 3-direction from the plane strain condition, i.e. transformation mismatch and thermal mismatch plasticity. Second, since in the present case the material is heated and cooled from one side (Fig. 3.1), a phase front may form and move in the 1-direction through the material and mismatch stresses can then arise locally near the phase front, i.e. ratchetting. However, no strain increment was observed after a full temperature cycle under zero applied stress (Fig. 3.5), indicating that ratchetting was absent. This is further confirmed by the lack of thermal gradient discussed earlier, indicating that no phase front is formed.

The numerical results shown in Fig. 3.5 are in qualitative agreement with the prediction of the analytical solution (Eq. 3.2): a linear strain-stress behavior at low stresses is followed by a non-linear strain increase at high stresses. Before proceeding to a quantitative comparison between analytical and numerical results, the stresses and the strain mismatch

must be harmonized between the numerical plane-strain model and the analytical three-dimensional model, as discussed more fully below.

The fundamental difference between the two models is the origin of the allotropic mismatch. In the analytical model leading to Eq. 3.2), internal stresses occur because the transformation is constrained within a plastically deforming material. In the numerical plane-strain model however, the constraint along the 3-direction is the only source of the internal stresses. Thus, the internal stress field is caused by the constraint in one single dimension (the 3-direction), as compared to the constraint in all three dimensions in the analytical model. To compare these models, an equivalent mismatch in plane-strain $(\Delta V/V)^*$ can then be defined as:

$$\left(\frac{\Delta V}{V}\right)^* = \frac{1}{3}\left(\frac{\Delta V}{V}\right). \tag{3.10}$$

In the present case, $(\Delta V/V)^* = (\Delta L/L) = 0.348\%$.

Another important difference between the models is the stress at which plasticity occurs. While the analytical model is based on yield under uniaxial tension, the current numerical model considers yield under plane-strain conditions. For plane-strain under an applied stress σ in the 2-direction, the non-zero stress components are: $\sigma_{22} = \sigma$, and $\sigma_{33} = \nu\cdot\sigma$. Thus the equivalent Von Mises stress is:

$$\sigma_{eq} = \sigma \cdot \sqrt{1 - \nu + \nu^2} \tag{3.11}$$

and the uniaxial stress in the 3-direction to induce plastic yielding σ_Y^* is:

$$\sigma_Y^* = \frac{\sigma_Y}{\sqrt{1 - \nu + \nu^2}}. \tag{3.12}$$

Taking $\nu = 1/2$, Eq. (3.12) gives $\sigma_Y^* = (2/\sqrt{3})\cdot\sigma_Y$.

For the specific case of Fig. 3.5 with a uniaxial yield stress $\sigma_Y = 7.5$ MPa, the plane-strain yield stress calculated from Eq. 3.12 is then $\sigma_Y^* = 8.66$ MPa. As expected, the strain

increments in Fig. 3.5 are finite above σ_Y but tend to infinity when approaching σ_Y^*. The same overall behavior is observed in Fig. 3.5 for the higher yield stress σ_Y = 11 MPa. At small stresses, the strain increments are proportional to the applied stress, but the proportionality constant is smaller than for σ_Y = 7.5 MPa, as expected from the larger value of σ_Y and Eq. 3.1. At high stresses, the curve diverges when the stress approaches the plane-strain yield stress σ_Y^* = 12.70 MPa.

The plane-strain specific volume mismatch (Eq. 3.10) and yield stress (Eq. 3.12) can be used to redefine the analytical solutions (Eqs. 3.2 and 3.3) using

$$\alpha^* = \frac{\Delta\varepsilon}{2 \cdot (\Delta V / V)^*} \tag{3.13a}$$

$$\delta^* = \frac{\sigma}{\sigma_Y^*} \tag{3.13b}$$

The numerical results (Fig. 3.6) confirm the linearity between the mismatch $\Delta V/V$ and the strain increment in the 2-direction $\Delta\varepsilon$. The results at the lower stress σ = 4.0 MPa can be compared to Eq. 3.3 using the specific plane-strain quantities (Eqs. 3.13a,b). With δ^* = 0.46, Eq. 3.3 predicts α^* = 0.38. This is to be compared to the slope of $d(\Delta\varepsilon)/d(\Delta V/V)$ = 0.30 in Fig. 3.6, which must be multiplied by a factor 2/3 to account for a half cycle (factor 2, Eq. 3.13a) and for the effective mismatch (factor 3, Eq. 3.10), resulting in a value of 0.45. For a high stress σ = 8.0 MPa (δ^* = 0.92) where the strain increments increase non linearly with the applied stress, Eq. 3.2 gives α^* = 3.0, while $(3/2)\cdot d(\Delta\varepsilon)/d(\Delta V/V)$ = 2.0 is obtained from Fig. 3.6. The numerical model thus underestimates the analytical normalized strain increment, probably as a result of the different assumptions used.

Figure 3.7 shows the numerical values of Fig. 3.5 normalized by the plane-strain mismatch $(\Delta V/V)^*$ and the plane-strain yield stress σ_Y^* given by Eqs. 3.10 and 3.12. Also shown in Fig. 3.7 are the predictions from Eqs. 3.2 and 3.3 (using $2\cdot\alpha$ for a full temperature cycle encompassing two phase transformations) as well as the experimental data

on pure iron by Refs. [17,39]. In the linear region at low stresses ($\delta < 0.4$), there is good agreement between the numerical, analytical and experimental results. In the non-linear region however, the 2-dimensional numerical model gives somewhat higher strain values than the 3-dimensional analytical solution (Eq. 3.2), but correctly predicts the progressive departure from the linear behavior observed both in the analytical model and the experimental data. Also, the experimental point for the highest stress is significantly lower than predicted by the models, probably because the large strains developed during cycling give raise to strain hardening, thus increasing the yield stress of the material and decreasing the total strain increment, as modeled in Ref. [107].

3.5 Conclusions

A finite-element model for transformation superplasticity is presented for an elastic, ideally-plastic material. The numerical model not only gives the total strain accumulated after crossing the allotropic range under stress, it also allows the study of the time-evolution of the plastic strains and stresses during the phase transformation. Numerical results for the ferrite-austenite transformation iron capture the behavior predicted by closed-form solutions, i.e. the strain increments after a thermal cycle increase first linearly with the applied stress, but diverge when the applied stress becomes large. However, the numerical model approximates the constrained phase transformation in a polycrystalline material with a simple plane-strain constraint. Thus, while the constrained mismatch for a polycrystalline material is $\Delta V/V$, only one third of this volumetric mismatch is available as the mismatch source in the plane-strain configuration, where only one direction is constrained. Furthermore, the yield stress in plane-strain is slightly higher than the yield stress under uniaxial conditions. Taking these two differences into account in the normalization of the data, the numerical model can be compared to the analytical model as well as experimental

data for iron. Good agreement is found both for small stresses (where strain increments increase linearly with stress) and for high stresses (where the behavior is non-linear).

Figures of Chapter 3

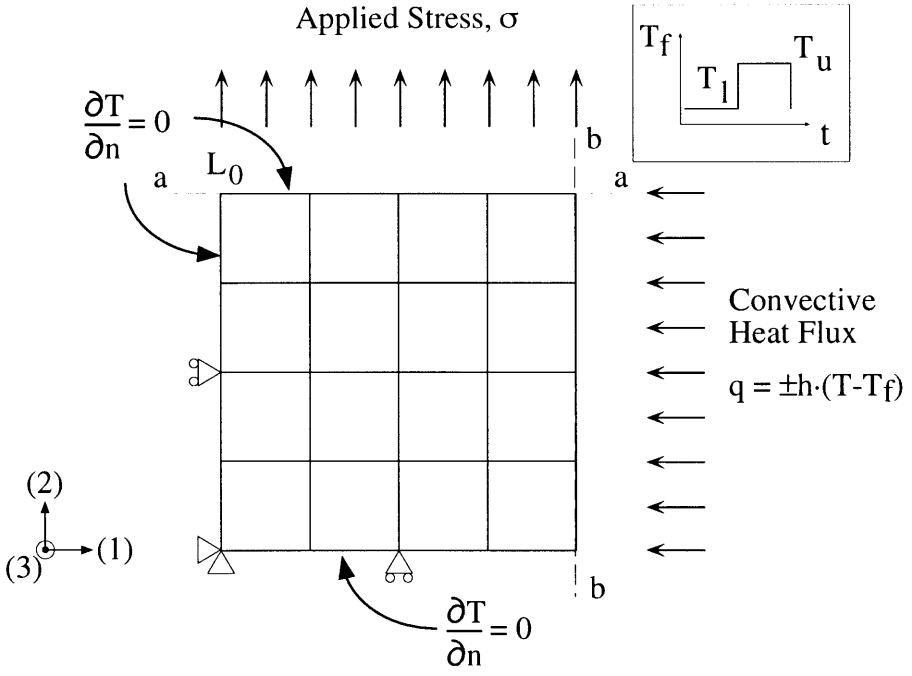

Figure 3.1: Mesh, symmetry and boundary conditions of the plane-strain coupled temperature-displacement model. The applied temperature profile is given in insert.

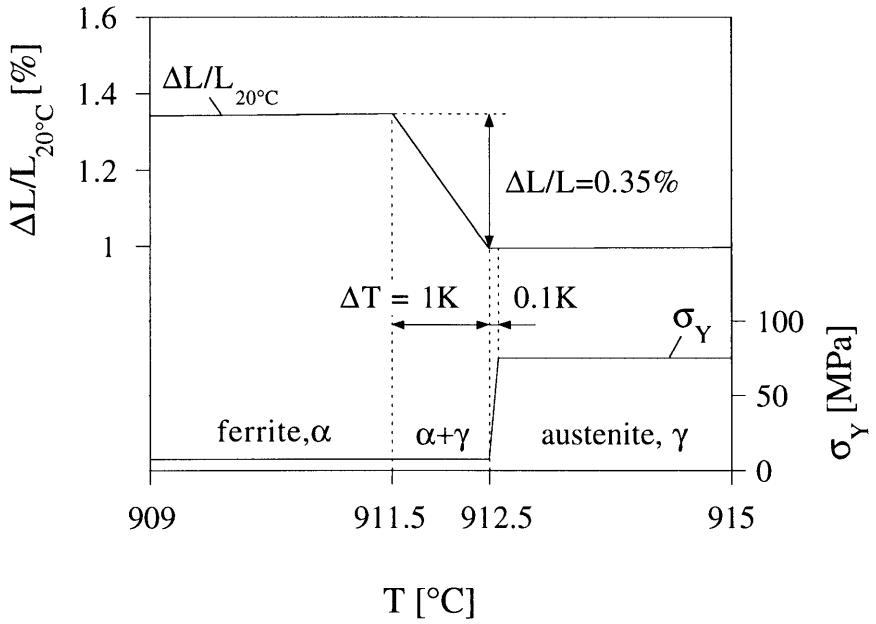

Figure 3.2: Thermal strain ($\Delta L/L_{20°C}$) with allotropic strain ($\Delta L/L$) and yield stress σ_Y as a function of temperature.

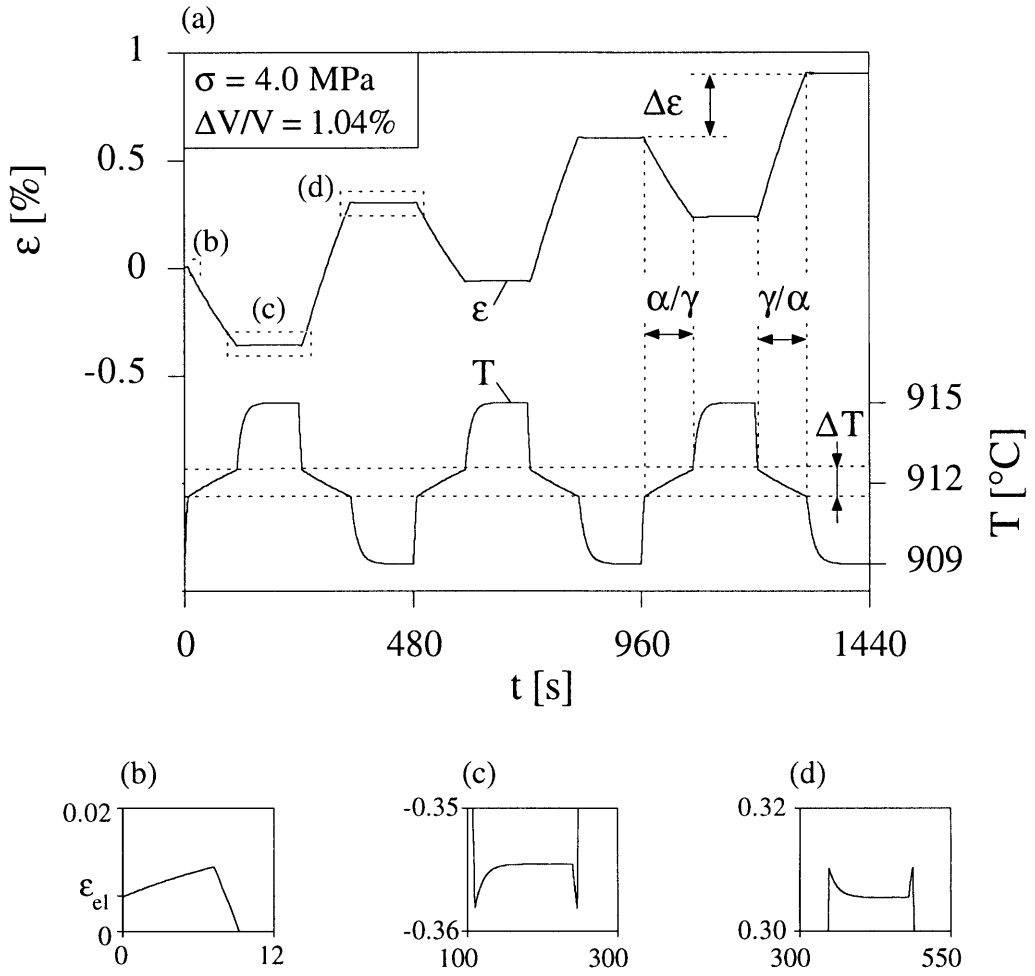

Figure 3.3: (a) Total uniaxial strain in the 2-direction and temperature as a function of time during the first three cycles for an applied stress σ = 4.0 MPa at σ_Y = 7.5 MPa; (b), (c), (d) magnified regions of the strain history.

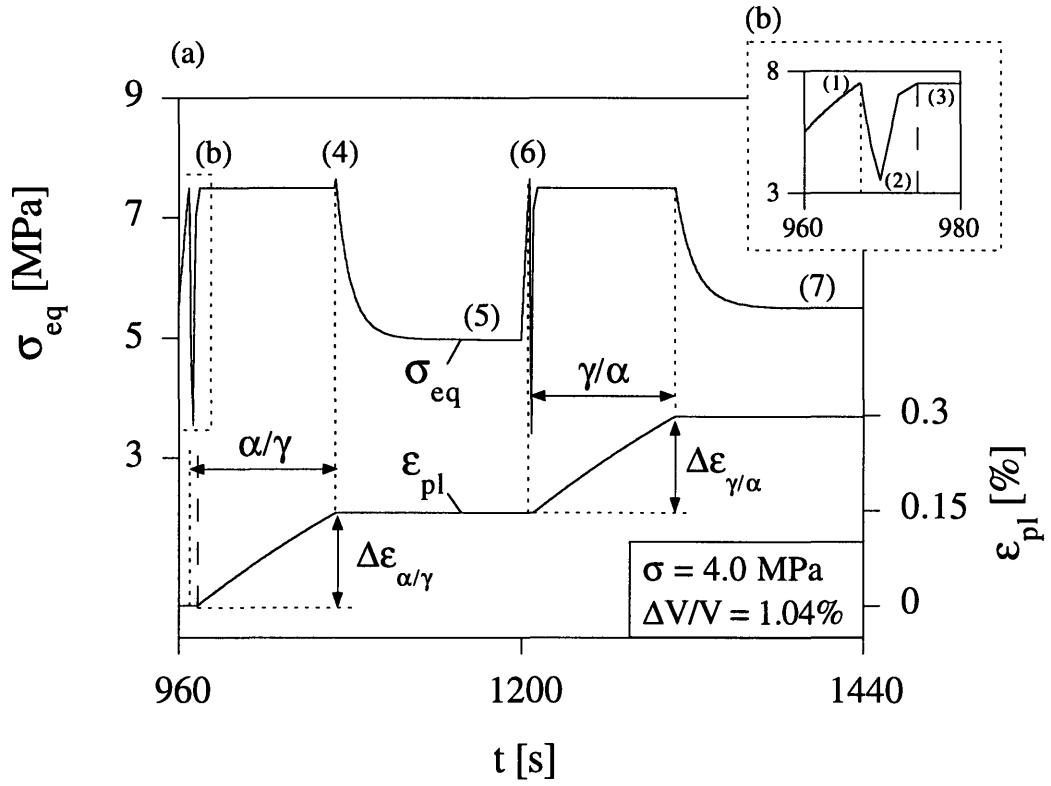

Figure 3.4: (a) Von Mises equivalent stress and uniaxial plastic strain in the 2-direction as a function of time during the third cycle for an applied stress σ = 4.0 MPa and a uniaxial yield stress σ_Y = 7.5 MPa; (b) magnified region at the onset of transformation.

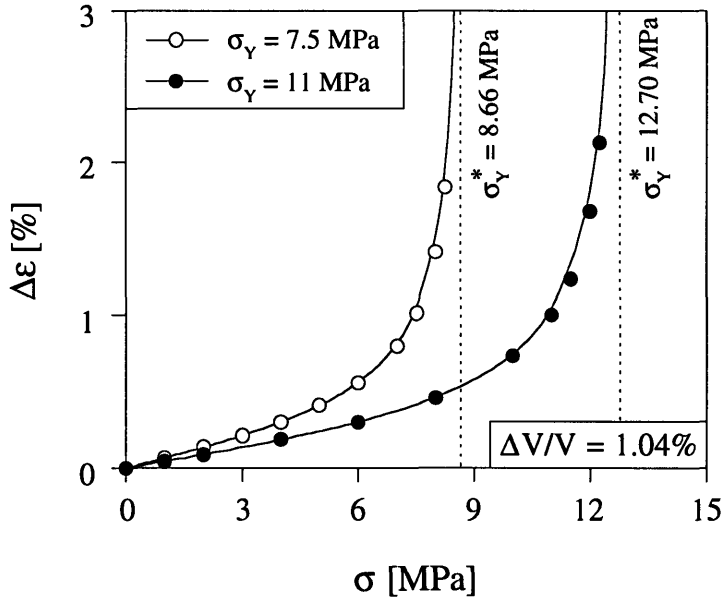

Figure 3.5: Strain increment in the 2-direction for a full cycle as a function of the applied stress for uniaxial yield stresses σ_Y = 7.5 MPa and σ_Y = 11 MPa.

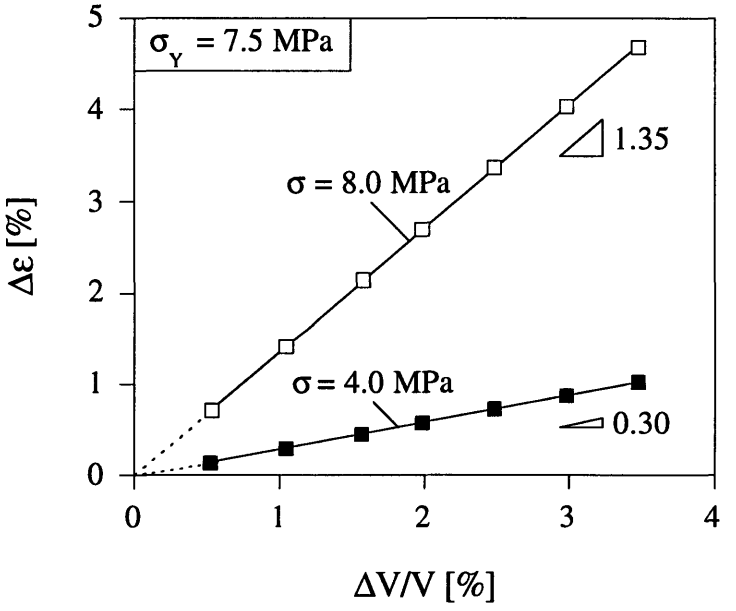

Figure 3.6: Strain increment in the 2-direction for a full cycle as a function of the allotropic volume mismatch for applied stresses σ = 4.0 MPa and σ = 8.0 MPa with σ_Y = 7.5 MPa.

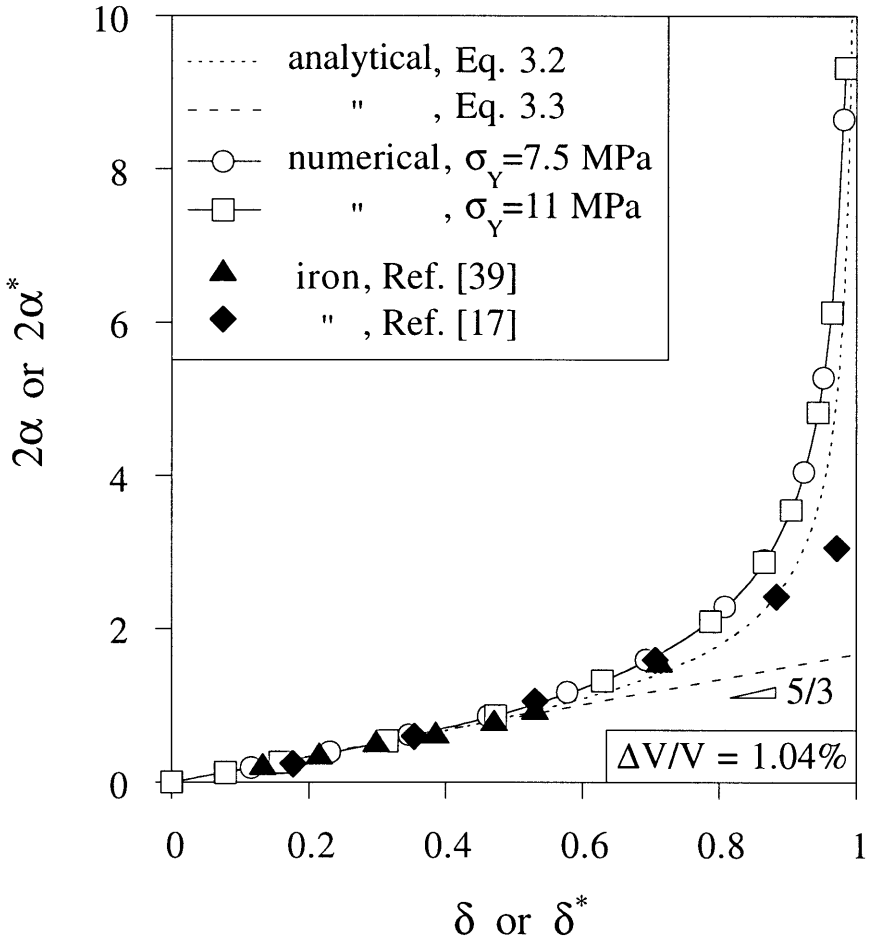

Figure 3.7: Strain increment in the 2-direction for a full cycle normalized by the transformation mismatch as a function of the applied stress normalized by the yield stress. Comparison between analytical predictions, numerical predictions and experimental results for pure iron.

Tables of Chapter 3

Table 3.1: Physical properties of iron near the phase transformation.

Property		Temperature 911.5°C (ferrite)	Temperature 912.5°C (austenite)	Ref.
Density	ρ [$g \cdot cm^{-3}$]	7.87	7.58	[3]
Transformation Enthalpy	ΔH [$J \cdot g^{-1}$]	18.8		[7]
Specific Heat	C_p [$J \cdot g^{-1} \cdot K^{-1}$]	0.87	0.71	[7]
Coefficient of Thermal Expansion*	$\alpha_{20°C}$ [K^{-1}]$\cdot 10^6$	15.0	11.1	[8]
Thermal Conductivity	k [$W \cdot cm^{-1} \cdot K^{-1}$]	0.296	0.286	[93]
Poisson's Ratio	ν [–]	0.3	0.3	[3]
Young's Modulus	E [GPa]	65.1	117	[31]

* technical value, defined as $\alpha_{20°C} := (L - L_{20°C})/(T - 20°C)$ where L and $L_{20°C}$ are the sample lengths at the temperatures T (in degrees centigrade) and 20°C, respectively.

Chapter 4

Transformation Superplasticity of Zirconium

Abstract

A tensile strain of 270% was achieved for coarse-grained zirconium subjected to transformation superplasticity conditions, where strain increments are accumulated upon repeated thermal cycling around the allotropic transformation temperature under the biasing effect of a uniaxial tensile stress. The strain increment per cycle was found to consist of two equal contributions from transformations on heating and cooling, and to increase linearly with the applied stress. The measured strain increments are in good quantitative agreement with predictions based on the average internal stress during the transformation, which was determined independently from experimental transformation times. As the cycling frequency is raised, the average strain-rate increases (a maximum value of $1.3 \cdot 10^{-4}$ s^{-1} was measured), but the strain increment per cycle decreases above a critical cycling frequency for which the sample gauge section undergoes only a partial phase transformation. The resulting reduction in internal mismatch and increase in internal stress are modeled using the experimental observation that β–Zr deforms by a mixture of diffusional and dislocation creep in the stress range of interest.

4.1 Introduction

Superplastic deformation is characterized phenomenologically by tensile failure strains above 100% and can be classified into two mechanism types: fine-structure superplasticity and internal-stress superplasticity [60]. The former type of superplasticity relies on grain-boundary sliding and is operative in metals with grains smaller than 10 μm which are stable at the temperature of deformation. This can be achieved through duplex microstructures or through grain boundary pinning by fine second-phase particles [60]. Since pure metals display neither duplex structures nor grain boundary pinning, they exhibit rapid grain growth at elevated temperature and are thus incapable of fine-structure superplasticity. However, certain pure metals can deform superplastically by the second mechanism (internal-stress superplasticity), where internal mismatch stresses are biased by an external stress, resulting in a strain increment. These mismatch stresses and the resulting strain increments can be repeatedly produced by thermal cycling of pure metals exhibiting coefficients of thermal expansion anisotropy [27,60] (e.g. Zn [54,72,101], U [54,101,103]) and/or an allotropic phase transformation [25,60] (e.g. Fe [17,39,108], Co [39,73], Ti [26,39], Zr [39,55], U [39]). Since the only requirement for internal-stress superplasticity is the repeated creation of internal mismatch stresses, these pure metals can be deformed superplastically by this alternate mechanism independently of their grain size.

In transformation superplasticity, internal mismatch stresses are produced by the volumetric difference between the two allotropic phases $|\Delta V/V|$ (referred to as $\Delta V/V$ in the following). A net plastic strain increment is produced in the direction of the applied stress after each phase transformation as a result of the accommodation of these internal mismatch stresses by the weaker allotropic phase, which can deform either by time-independent plastic yield, or by a time-dependent creep mechanism such as dislocation creep or diffusional creep. Transformation superplasticity was first investigated systematically by Greenwood

and Johnson [39], who developed a model predicting a linear relationship between the applied stress σ and the plastic strain increment per transformation $\Delta\varepsilon$:

$$\Delta\varepsilon \approx \frac{2}{3} \cdot \frac{\Delta V}{V} \cdot \frac{\sigma}{\sigma_0} \cdot \frac{5 \cdot n}{(4 \cdot n + 1)} , \tag{4.1}$$

where σ_0 is the average internal stress (averaged over both transformation time and spatial orientation of the phase transformation) of the plastically deforming weaker phase, and n is the stress exponent of the creep law describing the plastic accommodation. Greenwood and Johnson [39] also considered the case of ideal plastic yielding at low homologous temperatures which can be described with Eq. 4.1 by replacing σ_0 by the yield stress σ_Y of the weaker phase and by letting n tend to infinity.

Equation 4.1, which is only valid for small applied stresses, was later extended analytically by Refs. [30,107] to high applied stresses where a non-linear stress-strain behavior is predicted for plastically yielding materials (e.g. Fe, Co, $U_{\alpha/\beta}$). Similarly, Mitter [58] numerically solved the non-linear case of high applied stresses for materials deforming by yield and by creep (e.g. Ti, Zr, $U_{\beta/\gamma}$).

As seen from Eq. 4.1, low values for the yield stress or the internal stress result in large strain increments. Thus, phase transformations occurring at high homologous temperatures where the material is weak are most suitable for deformation by transformation superplasticity. However, high cycling temperatures also promote creep outside the transformation range, so that experimentally measured plastic strain accumulated after a full cycle often include appreciable amounts of creep strain unrelated to the superplastic strain increment. Creep is furthermore undesirable because it promotes cavitation and neck instability which reduce the total strain to failure. Thus, the observation of transformation superplasticity (large elongation to fracture and linear dependence between applied stress and strain increment, Eq. 4.1) depends sensitively on suppressing creep outside the

transformation range, which can be achieved by optimizing the temperature cycle profile and the sample geometry.

In the present paper, we investigate transformation superplasticity in pure zirconium, which was chosen for the following three reasons. First, to our knowledge, only two studies [39,55] exist on the transformation plasticity of zirconium. Second, these studies did not report values for failure strains, a necessary condition for demonstrating transformation superplasticity. Third, zirconium shows an allotropic phase transformation at $T_{\alpha/\beta}$ = 863°C ($T_{\alpha/\beta}/T_m$ = 0.53) [6] where creep is the dominant deformation mechanism [80]. Thus, zirconium can be used to test the numerical predictions of Mitter [58] for a creeping material transforming under high applied stresses. As described above, this can only be achieved if creep outside the phase transformation range is minimized, a condition we fulfill by modifying the usual geometry for superplastic samples. Furthermore, we use measured thermal characteristics during the phase transformation to calculate the average internal stress σ_0, which is compared to predictions from mechanical models.

4.2 Experimental Procedures

The material used was unalloyed zirconium (Zircadyne 702 from Wah Chang, OR) with extra-low oxygen content (Table 4.1). Flat tensile samples were machined with their gauge length parallel to the rolling direction. Because the sample heads (length: 28.1 mm, width: 14.0 mm, thickness: 4.44 mm, hole diameter: 5.07 mm) were much larger than the gauge section (length: 19.85 mm, width: 5.10 mm, thickness: 4.44 mm), only 12% of the total sample volume was in the gauge section.

Thermal cycling and isothermal creep experiments were conducted under small uniaxial tensile stresses in a custom-designed apparatus (Fig. 4.1). Rapid heating was achieved by using four symmetrically-arranged, 2 kW, infrared radiant heaters concentrating radiation at a focal line. The temperature was controlled at the sample surface (point A in Fig. 4.1b,c)

and monitored at the head of the sample (point B in Fig. 4.1b,c) with inconel-shielded, boron-nitride coated, grounded K-type thermocouples with a small diameter of 1.6 mm to minimize the response time. Both thermocouples were subjected to (i) a radiative heat flux to, and from, the sample surface, (ii) a conductive heat flux through the sample, and (iii) a convective heat flux caused by the inert gas. For isothermal conditions, where these heat fluxes are at steady-state, the temperatures measured corresponded to the internal sample temperature. However, under transient conditions, i.e. temperature cycling, the thermocouples measured a combination of surface temperature and surrounding temperature. The thermocouple B positioned at the sample head was farther from the focal line of the heaters and thus experienced lower heat flux density as compared to the controlling thermocouple A located at the sample surface.

Square wave temperature profiles were applied at the sample surface with temperatures between T_A = 810-940°C and frequencies between ν = 6-30 hr^{-1}. A special characteristic of the experiments was that only the gauge section was fully exposed to the radiative heat flux whereas the sample heads were largely shielded from the radiation (Fig. 4.1b). By using alumina pins and spacers (Fig. 4.1c) as well as low-conductivity Inconel pullheads and pullrods to minimize heat transfer through the sample heads, sample cooling was also mainly controlled by radiation from the surface of the gauge section. The sample was surrounded by a quartz tube flushed with purified argon produced by flowing 99.999% pure argon through a titanium powder bed held at a temperature of 1000°C. The sample stress was adjusted manually by applying weights. The force from the spring bellow compensated the stress increase due to the sample cross-sectional reduction, so that constant stress conditions were maintained over a defined deformation range.

The deformation, which was measured by a linear voltage displacement transducer placed at the cold end of the lower pullrod, included the thermal dilatation of the whole load train and therefore did not represent the sample deformation under transient temperature

conditions. However, the plastic deformation measured under steady-state conditions and over full temperature cycle periods was only due to the sample plastic deformation.

The same sample was subjected to both isothermal creep and thermal cycling under stress in an experiment consisting of five successive parts. In the first part, the sample was heated to 810°C under a low stress (0.3 MPa) until the deformation rate of the load train due to thermal expansion was below the detection limit of the apparatus ($d(\Delta D)/dt < 4\ \mu m \cdot hr^{-1}$). Creep was then measured at 810°C at different stress levels between 0.6-2.0 MPa, and at 910°C at a constant stress of 1.0 MPa, allowing enough time to reach steady-state at each stress and temperature. In the second part of the experiment, the sample was thermally cycled with a frequency of 10 hr^{-1} between the lower cycling temperature $T_A = T_l = 810°C$ and the upper cycling temperature $T_A = T_u = 910°C$ at stresses of 0.3 MPa and 1.0 MPa. Before and after each cycling segment which consisted of 4 to 8 individual cycles, steady-state isothermal creep was established. In the third part of the experiment, cycling segments were conducted where the cycling frequency was varied between 6 hr^{-1} and 15 hr^{-1} at a constant stress of 1.0 MPa and with temperature amplitudes of $T_l = 810°C$ and $T_u = 910°C$. These cycling segments were also preceded and succeeded by isothermal creep measurements at the upper cycling temperature T_u. The fourth and fifth parts of the experiment consisted of a series of stress variations at frequencies of $\nu = 15\ hr^{-1}$ and $\nu = 30\ hr^{-1}$, respectively, with $T_l = 810°C$ and $T_u = 910\text{-}940°C$. The stress was changed in discrete steps during the thermal cycling, with 8 to 20 cycles measured at each stress level. The experiment was stopped after 25 hr and a total of 212 cycles, because the travel limit of the apparatus had been reached.

4.3 Results

Figure 4.2 shows the isothermal steady-state creep rate of α–Zr at 810°C and β–Zr at 910°C, as measured during the first and second part of the experiment. The creep behavior can be described by a power-law:

$$\dot{\varepsilon} = \frac{A}{T} \cdot exp\left(-\frac{Q}{R \cdot T}\right) \cdot \left(\frac{\sigma}{E}\right)^{n}, \qquad (4.2)$$

where R is the gas constant, Q is the activation energy, E is the Young's modulus and A is a constant. This constant is obtained by fitting Eq. 4.10 to the experimental data using literature values for Q_α = 190 kJ·mole^{-1} and the shear modulus [80] (converted to Young's modulus using a Poisson's ratio of 0.35 [3]), giving $A_{810°C} = 4.9 \cdot 10^{16}$ K·s^{-1} and $n_{810°C}$ = 2.4. At 910°C, the creep curve shows a gradually increasing stress exponent so that the data for stresses below 0.6 MPa are best described by a stress exponent $n_{910°C}$ = 2.9 whereas the data for stresses above 0.8 MPa show $n_{910°C}$ = 5.0; the pre-exponential factors are $A_{910°C} = 4.6 \cdot 10^{19}$ K·s^{-1} and $A_{910°C} = 1.1 \cdot 10^{30}$ K·s^{-1} respectively using Q_β = 184 kJ·mole^{-1}[80].

Figure 4.3 shows the strain history upon thermal cycling between T_l = 810°C and T_u = 910°C with a thermal cycling frequency of ν = 6 hr^{-1} at a stress σ = 0.34 MPa, followed by the isothermal creep history of β-zirconium for the same stress at the upper cycling temperature T_u = 910°C measured immediately after cycling. Despite the lower average temperature of the cycling experiments, the average strain rate upon thermal cycling $\dot{\varepsilon}_{cyc}$ = $3.9 \cdot 10^{-6}$ s^{-1} is ten times higher than the isothermal creep rate of β-zirconium $\dot{\varepsilon}_{910°C}$ = $4.0 \cdot 10^{-7}$ s^{-1}.

The strain increment per cycle $\Delta\varepsilon_{tot}$ = ΔD/L (where ΔD = ΔL is the deformation increment of the sample gauge for a full cycle and L is the gauge length at the beginning of the cycle) is shown in Fig. 4.4 as a function of the applied stress for cycles with T_l = 810°C, T_u = 910-940°C and ν = 6-30 hr^{-1}. Cycling data measured when the sample strain was under 56% are

not given in Fig. 4.4 because, before that point, the stress-normalized cyclic strain increments were slowly but systematically decreasing, most probably as a result of grain growth in the sample. Figure 4.4 shows that, at frequencies below $\nu = 30\ hr^{-1}$, the strain increment increases linearly with the applied stress up to $\sigma = 1.4$ MPa with a slope $d(\Delta\varepsilon_{tot})/d\sigma = 4.4\ GPa^{-1}$. A linear fit of the data gives an extrapolated strain value of $\Delta\varepsilon_0 = 0.08\%$ when no stress is applied. At $\sigma = 1$ MPa several points measured at frequencies of $\nu = 6\text{-}15\ hr^{-1}$ overlap. Upon cycling with a high frequency of $\nu = 30\ hr^{-1}$, smaller strain increments are observed, leading to a slope $d(\Delta\varepsilon_{tot})/d\sigma = 3.0\ GPa^{-1}$ up to $\sigma = 2.9$ MPa, after which a significantly higher strain increment $\Delta\varepsilon_{tot} = 1.6\%$ is obtained for the maximum stress of 3.4 MPa.

The points shown in Fig. 4.4 are averages of 4 to 6 total cycle strain increments. Over multiple cycles, the deformation increment ΔD showed only a very small standard deviation (the reproducibility of the deformation upon thermal cycling is illustrated in Fig. 4.3a). However, the length L of the sample was calculated assuming conservation of volume of the gauge section without sample head deformation or necking. The systematic error due to these simplifying assumptions increases with the extent of plastic deformation and was estimated by comparing the final gauge length (calculated as the sum of the deformation increments and including the deformation of the sample heads) with the measured gauge length of the deformed sample at the end of the experiment. Accordingly, the uncertainties are $\pm 5\%$ for the strain and $\pm 8\%$ for the stress.

Figure 4.5 depicts the deformation history, D(t), for two heating segments as measured with the linear voltage displacement transducer and the corresponding temperature $T_B(t)$ measured at the shoulder of the sample head (Fig. 4.1b,c) for upper cycling temperatures $T_u = T_A = 910°C$ and 940°C. The controlling gauge section temperature (thermocouple A) reaches its final value very rapidly ($dT/dt = 10\text{-}15\ K \cdot s^{-1}$) and is not shown in Fig. 4.5.

Figure 4.6 shows the sample before the experiment and after a total strain e = 270% had been accumulated without fracture at the end of the experiment. Metallography of the undeformed sample revealed equiaxed grains typical of a cold-worked, recrystallized structure with a grain size d = 19±2 μm. The deformed sample showed large, coarsened grains (d = 0.2-2 mm), typical of a transformed β-structure. Except for hydrogen, the concentrations of interstitial elements increased only little during the 25 hr experiment (Table 4.1). Hydrogen probably originated from traces of water in the argon gas, decomposing over the titanium bed where oxygen was gettered preferentially, thus increasing the hydrogen concentration in the cover gas, which was then absorbed by the zirconium sample. This slight contamination did not, however, affect the transformation superplastic behavior over the course of the experiment; furthermore, hydrogen can easily be removed from zirconium by a vacuum anneal.

4.4 Discussion

4.4.1 Isothermal Creep

Figure 4.2 shows that isothermal creep of BCC β-zirconium is significantly faster at 910°C than for HCP α-zirconium at 810°C, as expected from the more open BCC structure of β-zirconium and in agreement with the deformation mechanism map of zirconium by Sargent and Ashby [80]. However, the stress exponent $n_{910°C}$ = 5.0, measured at high stresses for β-zirconium, is somewhat higher than the reported value n = 4.3 for power-law creep [80]. This discrepancy may be due to the fact that the latter stress exponent was not experimentally measured, but assumed to be equal to that of isomechanical β-titanium. The calculated transition between diffusional creep and power-law creep (expected for β-zirconium at σ = 1.0 MPa for a grain size d = 0.2 mm and at σ = 0.25 MPa for a grain size

of d = 2 mm [80]) is in agreement with the observed gradual decrease of stress exponent below about σ = 0.8 MPa.

The stress exponent $n_{810°C}$ = 2.4 for α-zirconium (measured over the narrow stress range of interest for the present cycling experiments) is much lower than the experimental literature value for power-law creep of cold-rolled and annealed α-zirconium (n = 6.6 [80]). As for β-zirconium, the deformation mechanism of α-zirconium is calculated to change from power-law (n = 6.6) to diffusion (n = 1) in the stress range σ = 1.4-3.2 MPa for d = 0.2-2 mm [80].

4.4.2 Thermal Cycling

4.4.2.1 Experiment Design

The experimental set-up (Fig. 4.1) was designed to minimize deformation of zirconium in the β-range where creep is rapid (Fig. 4.2). While the large sample heads were mostly shielded by the pull heads from the radiative heat flux (Fig. 4.1b), the gauge section was fully exposed to the radiation, so that heat flow to the sample occurred predominantly through the surface of the gauge section. Conversely on cooling, little heat was lost by conduction through the alumina pins and spacers and the low-conductivity superalloy load train (Fig. 4.1c), so that heat transfer occurred mostly by radiation from the gauge surface.

During the allotropic phase change, the heat flux has to provide the transformation enthalpy. The time for the complete transformation of the sample is thus proportional to the ratio of the volume to be transformed (full sample volume including gauge section and sample heads) and the area of the heat-flux surface (gauge section surface area only). Since heat flows predominantly trough the gauge section, the transformation of the sample heads occurs by conduction of heat from the sample gauge section. Given that the initial volume-to-surface-area ratio for the gauge section V_0/S_0 = 1.2 mm is small compared to the ratio of the head volume to the gauge area V_h/S_0 = 8.8 mm, the gauge section transforms much more

rapidly than the large sample heads. However, since conduction is not limiting, the temperature throughout the gauge section remains constant at the phase transformation temperature until the sample heads are fully transformed. The slowly-transforming heads thus act as heat sinks (on heating) and heat reservoirs (on cooling) after the gauge section has fully transformed. By using cycle periods longer than the time interval necessary to complete the phase transformation in the gauge section but shorter than the time interval to transform the whole sample, the sample temperature can be maintained at the allotropic temperature $T_{\alpha/\beta}$, thus minimizing excessive creep in the β-range. This heat-buffer technique is also potentially interesting for commercial superplastic forming, as it allows a passive control of the temperature and minimizes creep in the weak allotropic phase.

4.4.2.2 Transformation Times

The heat transport analysis is based on the assumption that (i) heat transfer is by radiation only, (ii) the absorptivity and emissivity of the sample are $\alpha' = \varepsilon' = 0.5$ and (iii) thermal gradients are negligible within the material. The latter assumption is validated by calculating the dimensionless number M [36], which is equivalent to the Biot number for conductive heat transport, and is defined as:

$$M = \frac{\sigma_B \cdot \alpha' \cdot T^3 \cdot x}{k} , \qquad (4.3)$$

where σ_B is the Stefan Boltzmann constant, α' the absorptivity on heating (or the emissivity on cooling), k the thermal conductivity and x is the characteristic distance, which is half the sample gauge section width for the transformation of the gauge section, or the head length for the transformation of the heads. With k(860°C) = 25 $W \cdot m^{-1} \cdot K^{-1}$ [3], $\alpha' = 0.5$, T = 940°C, x = 2.55 mm for the gauge section and x = 28.1 mm for the sample head, Eq. 4.3 gives values for M smaller than 0.1 (M = 0.005 and M = 0.06 respectively), so that of thermal gradients within the material are negligible and conduction is not controlling the heat

transport (Newtonian conditions). The absence of macroscopic thermal gradients within the material also excludes deformation by ratchetting observed during allotropic cycling of e.g. uranium [86] with a sharply-defined phase front.

In Fig. 4.5 the temperature T_B, as measured at the sample head surface, increases until the onset of the phase transformation where the rate of heating is reduced to near zero due to the absorption of heat supporting the transformation enthalpy. After the gauge section has transformed (marked as t_{min} in Fig. 4.5), the heating rate measured at point B increases again until the temperature levels off at about 30°C below the upper cycling temperature specified by T_A. The above interpretation (i.e., the temperature T_B is largely constant during the transformation of the sample gauge section, but is increasing during the transformation of the sample heads) can be justified as follows.

Over the short time period corresponding to the gauge transformation, the temperature at the thermocouple tip T_B is controlled by the sample temperature which is constant due to the phase transformation; however, over the long time period where the sample heads transform, the heating contribution from the heat flux to the thermocouple mantle and tip becomes dominant and the thermocouple tip temperature T_B rises again, despite the constant sample temperature. As expected, the value of T_B at the transformation plateau increases with increasing flux, which is proportional to $T_u^4 - T_{\alpha/\beta}^4$ (Fig. 4.5). Also, T_B is lower than T_A because thermocouple B is further from the focus line of the heaters than thermocouple A, which is located at the gauge section surface. Thus, the thermocouple temperature measured at position B (Fig. 4.1b,c) is affected both by the heat flux due to transformation and the impinging radiation.

Under Newtonian conditions where thermal gradients are not sustainable within the material, the time Δt^* to transform a volume V by a radiative heat transfer mechanism through a surface S is:

$$\Delta t^* = \frac{\Delta H \cdot \rho}{\sigma_B \cdot \alpha' \cdot \left(T_s^4 - T_{\alpha/\beta}^4\right)} \cdot \frac{V}{S} \,, \tag{4.4}$$

where $\Delta H = \pm 38.8$ J·g^{-1} [84] is the enthalpy of transformation (positive on heating and negative on cooling), $\rho = 6.49$ g·cm^{-3} [13] is the density, and T_s is the surface temperature ($T_s = T_u$ on heating, $T_s = T_l$ on cooling). The volume to surface area ratio in Eq. 4.4 can be found as a function of the engineering strain e by conservation of volume:

$$\frac{V}{S} = \frac{1}{\sqrt{1+e}} \cdot \frac{V_0}{S_0} \,, \tag{4.5}$$

where $V_0/S_0 = 1.19$ mm is the initial ratio of the gauge section. The transformation times predicted by using Eqs. 4.4 and 4.5 are in good agreement with experimentally determined transformation times, as seen from Table 4.2 where averages are taken from four measurements. Although the predicted time for transformation (Eq. 4.4) depends on several assumptions (e.g. $\alpha' = \varepsilon' = 0.5$), the values for Δt^* are reasonable, so that the time t_{min} in Fig. 4.5 can indeed be taken as the time needed to transform the gauge section.

This time t_{min} depends on the cycle characteristics (T_l, T_u, ν) and is given in Table 4.3 for $T_u = T_A = 910$°C and $T_u = T_A = 940$°C. The minimum cycling period for a complete transformation of the gauge length is estimated as $2 \cdot t_{min}$ (taking the larger t_{min} value of heating and cooling from Table 4.3), so that the maximum cycling frequency is $\nu_{max} = (2 \cdot t_{min})^{-1} = 21$ hr^{-1} for cycles with $T_u = 910$°C. At cycle frequencies above this limit, the superplastic strain is expected to decrease as the gauge does not undergo a complete transformation. The cycle frequency was varied between $\nu = 6$-30 hr^{-1} at $T_u = 910$°C for a constant stress $\sigma = 1.0$ MPa (Fig. 4.7). By subtracting the extrapolated strain per cycle when no external stress is applied, $\Delta\varepsilon_0$, from the total strain per cycle, $\Delta\varepsilon_{tot}$, and normalizing by the applied stress, i.e. $(\Delta\varepsilon_{tot} - \Delta\varepsilon_0)/\sigma$, the single stress results can be directly compared to the slope $d(\Delta\varepsilon_{tot})/d\sigma$ obtained by varying the stress (Fig. 4.4).

At $T_u = 910°C$, the strain increment per cycle normalized by the stress $d(\Delta\varepsilon_{tot})/d\sigma = 4.4 \pm 0.3\ GPa^{-1}$ is constant between $\nu = 6\text{-}15\ hr^{-1}$ but decreases to $3.0 \pm 0.1\ GPa^{-1}$ at $\nu = 30\ hr^{-1}$. This is because at frequencies above $\nu_{max} = 21\ hr^{-1}$, only partial transformation occurs in the gauge section, so that the internal mismatch and thus the superplastic strain increments are reduced. When the upper cycle temperature is increased to $T_u = 940°C$, the critical frequency is increased to $\nu_{max} = (2 \cdot t_{min})^{-1} = 34\ hr^{-1}$. In contrast, the experimental data shows a reduction of $d(\Delta\varepsilon_{tot})/d\sigma$ already at about $\nu = 30\ hr^{-1}$. This value is lower than predicted, probably because of the effect of high cycle frequencies on the actual cycle temperatures: the sample is not given enough time to cool to the lower temperature or to heat to the upper temperature, thus decreasing the effective temperature amplitude, as discussed in more detail later.

The deformation histories in Fig. 4.5 show first the thermal expansion of the load train, followed by a decreasing expansion rate as the sample temperature is stabilized by the phase transformation of the large sample heads. During that time interval, the gauge section, which is fully transformed at t_{min}, is slowly creeping near the phase transformation temperature, as internal thermal gradients are not sustainable. The onset of accelerated expansion (marked as t_{max} in Fig. 4.5) is interpreted as the end of the phase transformation of the sample heads, where both thermal expansion and sample creep occur since the sample temperature rises again.

At low cycling frequencies, significant strain will be accumulated due to creep outside the phase transformation range, causing an increase of the total strain increment $\Delta\varepsilon_{tot}$. According to Fig. 4.7, this occurs at $\nu_{min} = (2 \cdot t_{max})^{-1} = 8.0\ hr^{-1}$ for cycles with $T_u = T_A = 940°C$ and $\nu_{min} = (2 \cdot t_{max})^{-1} = 3.5\ hr^{-1}$ for $T_u = T_A = 910°C$ (dotted lines in Fig. 4.7). The results for t_{max} are given in Table 4.3, where the single data point for $T_A = 910°C$ was obtained during isothermal creep at the end of thermal cycling while the value for $T_A = 940°C$ is the average of 4 cycles with a cycle frequency of $\nu = 6\ hr^{-1}$. Since the

measurements with a slope of $d(\Delta\varepsilon_{tot})/d\sigma = 4.4\ GPa^{-1}$ in Fig. 4.4 were performed at rates falling within the window given by ν_{min} and ν_{max}, the measured superplastic strain increments correspond to full transformation of a gauge length with an insignificant creep contribution after transformation plasticity.

A final check is performed by calculating the ratio of the time to transform the whole sample ($t_{max} - t_{min} + \Delta t^*$) to the time for gauge transformation (Δt^*). With experimental data from Table 4.2, this ratio is 14 at 910°C and 8 at 940°C, reasonably close to the ratio 8.3 of the total sample volume to the gauge section volume.

4.4.2.3 Cycle Strains

To the best of our knowledge, only two other studies exist on transformation superplasticity of zirconium. An early investigation was carried out by Lozinsky [55] under non-uniform temperature conditions, giving only a qualitative description of the effect. Greenwood and Johnson [39] performed a systematic study for zirconium cycled between 810°C and 910°C and reported a linear strain increment-stress behavior up to $\sigma = 1$ MPa (with a slope $d(\Delta\varepsilon_{tot})/d\sigma = 9.0\ GPa^{-1}$ significantly higher than in Fig. 4.4) becoming progressively non-linear up to a maximum strain increment of $\Delta\varepsilon_{tot} = 1.9\%$ at $\sigma = 1.4$ MPa. Although these results are qualitatively consistent with the present data (linear stress-strain correlation at small stresses followed by a non-linear increase), direct comparison is impossible since Greenwood and Johnson [39] stated neither cycle frequency nor grain size, so that the creep contribution outside the phase transformation range at higher stresses is unknown. Additional possible causes for their higher strain increments in the linear range are the presence of primary creep (if no creep deformation was performed prior to cycling) and the contribution of diffusional creep (if the grain size was not stabilized). The latter effect may also explain the decreasing strain increment (from $\Delta\varepsilon_{tot}/\sigma = 8.5\ GPa^{-1}$ to $\Delta\varepsilon_{tot}/\sigma = 5.0\ GPa^{-1}$, not shown in Fig. 4.4) observed during the second part of our experiment.

The theoretical models relate the physical properties of the transforming material ($\Delta V/V$, σ_0, A, Q, n) to the plastic strain $\Delta\varepsilon$ induced by a single phase transformation during a half cycle. However, the plastic strain increments $\Delta\varepsilon_{tot}$ measured over a whole cycle (Fig. 4.3) include plastic strains caused by both phase transformations on heating and cooling, which are not necessarily equal. We examine this issue in the following.

The load-train displacement measured at the end of each half-cycle on heating ΔD_h and on cooling ΔD_c (Fig. 4.3b) consists of three contributions:

$$\Delta D_{h,c} = \pm\Delta D_{cte} + \Delta D_{creep} + \Delta D_{tp} \ , \tag{4.6}$$

where ΔD_{cte} is the magnitude of the displacement of the load train due to the thermal expansion on heating or contraction on cooling, ΔD_{creep} is the displacement due to sample creep outside the phase transformation range and ΔD_{tp} is the displacement caused by transformation plasticity. While ΔD_{cte} is fully reversible over a whole thermal cycle, ΔD_{creep} and ΔD_{tp} give irreversible plastic strains at the end of each half-cycle. At low stresses were ΔD_{creep} is small compared to ΔD_{tp} (Fig. 4.3a) and ΔD_{tp} is linearly dependent on the applied stress, Eq. 4.6 can be approximated by:

$$\Delta D_{h,c} \approx \pm\Delta D_{cte} + \frac{d\left(\Delta\varepsilon_{h,c}\right)}{d\sigma} \cdot L \cdot \sigma \ , \tag{4.7}$$

where $\Delta\varepsilon_{h,c}$ is the strain increment per transformation (h: heating, c: cooling) and L is the gauge length of the sample. Thus, the slope of ΔD_h or ΔD_c as a function of $L\cdot\sigma$ gives the stress-normalized strain increment $d(\Delta\varepsilon_{h,c})/d\sigma$ for transformation on heating and cooling, respectively, as shown in Fig. 4.8 where $d(\Delta\varepsilon_h)/d\sigma$ = 2.4 GPa^{-1} and $d(\Delta\varepsilon_c)/d\sigma$ = 2.0 GPa^{-1}. Although the slightly higher value on heating may be due to creep outside the transformation range, the difference in the slope and in the intercepts at zero stress are within experimental error (5% on strain and 8% on stress). Thus, the strain increment per transformation on heating (α/β) and cooling (β/α) are equal for a given stress ($\Delta\varepsilon_h = \Delta\varepsilon_c =$

$\Delta\varepsilon$) with $d(\Delta\varepsilon)/d\sigma = 2.2 \pm 0.2\ GPa^{-1}$, as predicted by the linear theory (Eq. 4.1). It is assumed that this also holds for the non-linear stress region described in Refs. [30,58,107].

Because of its HCP-structure, α-zirconium exhibits different coefficients of thermal expansion for the basal plane and for its normal direction, so that the corresponding thermal strains are also a source of internal mismatch. The models developed for transformation plasticity can be used for anisotropic thermal expansion mismatch by introducing an equivalent volumetric mismatch $(\Delta V/V)_{eq}$ [107]:

$$\left(\frac{\Delta V}{V}\right)_{eq} = K_1 \cdot \overline{\Delta\alpha_m} \cdot \overline{\Delta T_{pl}} \ , \qquad (4.8)$$

where $\overline{\Delta\alpha_m}$ is the temperature-averaged difference between the coefficients of thermal expansion in the two directions, $\overline{\Delta T_{pl}}$ is the effective temperature amplitude causing plasticity and K_1 is a correction factor incorporating the non-ideality of the simple form of Eq. 4.8. For α-uranium and zinc, K_1 takes a value of 0.2. The thermal mismatch strain $\overline{\Delta\alpha_m} \cdot \overline{\Delta T_{pl}}$ can be estimated directly from the thermal dilatation curve [94]. Neglecting any elastic accommodation, the difference between the thermal strains ($\Delta L/L_{20°C}$) parallel to the c-axis and parallel to the a-axis is $\varepsilon_{c,863°C} - \varepsilon_{a,863°C} = 0.49\%$ at $T_{\alpha/\beta} = 863°C$ and $\varepsilon_{c,810°C} - \varepsilon_{a,810°C} = 0.43\%$ at $T_1 = 810°C$, giving $\overline{\Delta\alpha_m} \cdot \overline{\Delta T_{pl}} = 0.06\%$. Thus, the equivalent thermal expansion mismatch is $(\Delta V/V)_{eq} = 0.012\%$, which is negligible compared to the phase transformation mismatch $\Delta V/V = 0.41\%$ [94], so that thermal expansion mismatch superplasticity can be ruled out in the present case.

4.4.3 Internal Stress

4.4.3.1 Complete Transformation

Greenwood and Johnson [39] developed a model for transformation superplasticity where internal strain accommodation is by creep. In their derivation, they expressed the von Mises criterion in terms of strain rates which they integrated over the time of transformation Δt^* to relate the internal strains with the equivalent internal stress σ_0. By requiring compatibility of strains in the z-direction where the external stress σ is applied and by using invariant properties of the $\Delta V/V$-tensor, they obtained:

$$\sigma'_{zz} = \frac{\sigma_0 \cdot \left[\Delta\varepsilon - (\Delta V/V)_{zz}\right]}{(\Delta V/V)\cdot\left[1+\frac{9\cdot(\Delta\varepsilon)^2}{4\cdot(\Delta V/V)^2} - \frac{9\cdot\Delta\varepsilon\cdot(\Delta V/V)_{zz}}{2\cdot(\Delta V/V)^2}\right]^{\frac{(n-1)}{2\cdot n}}} \quad , \tag{4.9}$$

where $(\Delta V/V)_{zz}$ and σ'_{zz} are the zz-components of the mismatch tensor and deviatoric stress tensor respectively and σ_0 is the average internal stress given by:

$$\sigma_0 = E\cdot\left[\frac{2}{3}\cdot\frac{\Delta V/V}{\Delta t^*\cdot\frac{A}{T_{\alpha/\beta}}\cdot exp\left(-\frac{Q}{R\cdot T_{\alpha/\beta}}\right)}\right]^{1/n} . \tag{4.10}$$

Dimensionless strains and stresses can be defined:

$$\eta := \frac{\Delta\varepsilon}{\Delta V/V} \quad , \tag{4.11a}$$

$$\psi := \frac{\sigma'_{zz}}{\sigma_0} \quad , \tag{4.11b}$$

$$\gamma := \frac{(\Delta V/V)_{zz}}{\Delta V/V} \quad , \tag{4.11c}$$

where $\gamma = (1/3)\cdot cos(\varphi)^2\cdot sin(\vartheta)^2 + (1/3)\cdot sin(\varphi)^2\cdot sin(\vartheta)^2 - (2/3)\cdot cos(\vartheta)^2$ is obtained by relating the volumetric mismatch $\Delta V/V$ to $(\Delta V/V)_{zz}$, and by averaging over a spherical volume element within $\vartheta = \varphi = [0; \pi/2]$:

$$\bar{g} = \frac{\int_{\Omega} g \; d\Omega}{\int_{\Omega} d\Omega} \; . \tag{4.12}$$

where g is the function to be averaged. Equation 4.9 then takes the form:

$$\bar{\psi} = (\eta - \gamma)\cdot\left(1 + \frac{9}{4}\cdot\eta^2 - \frac{9}{2}\cdot\eta\cdot\gamma\right)^{\frac{(1-n)}{2\cdot n}} \; , \tag{4.13}$$

Because of the non-linearity introduced by the stress exponent n, integration of Eq. 4.13 is only possible by numerical methods (as done by Mitter [58]), except for two special cases. First, for $n = 1$ Eq. 4.13 takes the form

$$\delta = \frac{3}{2}\cdot\eta \; . \tag{4.14}$$

Second, for $n \rightarrow \infty$, (i.e. the ideal plastic limit [30,107]), Eq. 4.13 becomes:

$$\delta = \frac{1}{4} + \frac{1}{6\cdot\eta} + \frac{1}{2\sqrt{2\cdot\eta}}\cdot\left(\frac{3\cdot\eta}{4} - \frac{1}{6} - \frac{1}{9\cdot\eta}\right)\cdot ln\left[\frac{\left(3\cdot\eta + 3\sqrt{2\cdot\eta} + 2\right)^2}{9\cdot\eta^2 - 6\cdot\eta + 4}\right] \; . \tag{4.15}$$

In Eqs. 4.14 and 4.15, the dimensionless stress δ is defined as:

$$\delta := \frac{\sigma}{\sigma_0} = \frac{3}{2}\cdot\bar{\psi} \; . \tag{4.16}$$

For the case of small strains where $\Delta\varepsilon << \Delta V/V$ (i.e. $\eta << 1$), Greenwood and Johnson [39] expanded the argument of the right-hand side integral of Eq. 4.13 to obtain Eq. 4.1, expressed in dimensionless manner as:

$$\delta \approx \frac{3}{2} \cdot \frac{(4 \cdot n+1)}{5 \cdot n} \cdot \eta \quad . \tag{4.17}$$

Thus, the internal stress σ_0 can be determined by fitting experimental strain increment data:

(i) to Eq. 4.13 determined by numerical integration;

(ii) to Eq. 4.14 for diffusional accommodation with $n = 1$;

(iii) to Eq. 4.15 for power-law accommodation with a very high stress exponent ($n > 10$) over the whole range of stresses;

(iv) to Eq. 4.17 for power-law accommodation at small stresses ($\sigma << \sigma_0$).

Alternatively, the internal stress σ_0 can be found:

(v) from Eq. 4.10 if the transformation time Δt^* is known.

Because creep for zirconium in the stress range of interest is by a mixture of dislocation creep and diffusional creep with effective stress exponents between 2.9 and 5 (Fig. 4.4), methods (ii) and (iii) cannot be used to calculate the internal stress. Furthermore, most of the measured strain increments $\Delta\varepsilon$ are on the order of $\Delta V/V = 0.41\%$ (Fig. 4.4) so that method (iv) with Eq. 4.1 is strictly not possible. However, Eq. 4.1 has been used to model transformation superplasticity of creeping materials even at larger stresses and strains [26,39] where Eq. 4.1 coincides with the numerical solutions (Eq. 4.13). For full transformation cycles ($\nu < 30$ hr^{-1} in Fig. 4.4), we compare in Fig. 4.9 the analytical and numerical solutions with the adjusted strain increments $\Delta\varepsilon = (\Delta\varepsilon_{tot} - \Delta\varepsilon_0)/2\sigma_0$. These are found by subtracting from the experimental strain increment $\Delta\varepsilon_{tot}$ the extrapolated zero-stress strain value $\Delta\varepsilon_0 = 0.08\%$, dividing by 2 to obtain transformation strains (as the superplastic strain is composed of two equal contributions, Fig. 4.8), and normalizing by the internal stress $\sigma_0 = 1.6$ MPa. The internal stress was determined from three of the above methods, as described in the following.

First, fitting the data to the numerical solution of Eq. 4.13 (method (i)) using a least square error technique gives an internal stress $\sigma_0 = 1.6$ MPa for $\Delta V/V = 0.41\%$ for both $n =$

2.9 and $n = 5$, since the numerical solutions are not very sensitive to n at intermediate strain increments (i.e. $0.5 < \eta < 0.7$) where most of the data was collected. Second, using method (iv) with Eq. 4.1 beyond its nominal validity range with $d(\Delta\varepsilon)/d\sigma = 2.2\pm0.2$ GPa^{-1}, gives $\sigma_0 = 1.4\text{-}1.5\pm0.1$ MPa for stress exponents of $n = 2.9$ and $n = 5$ respectively. As expected, the latter values are close to that obtained from fitting to the numerical solution (method (i)), as both models coincide up to $\eta \approx 0.3$. However, the data with normalized strains between $\eta = 0.5\text{-}0.7$ (Fig. 4.9) is consistently above the predictions by Eq. 4.1, which is due to the difference of $\Delta\sigma_0 = 0.15$ MPa found between the best fits for the linear model and the numerical integration. Although this difference is small (≈10%), it demonstrates the limitation of the linear model.

Finally, method (v) gives an internal stress $\sigma_0 = 1.7\text{-}1.5$ MPa when Eq. 4.10 is used with the reported activation energy of β-zirconium $Q = 184$ kJ·mole^{-1} [80], the elastic modulus $E_\beta(863°C) = 51.7$ GPa [80], $n = 5.0$ and $A = 1.1\cdot10^{30}$ K·s^{-1} as well as the experimentally-determined time periods for gauge transformation $\Delta t^* = 24\text{-}34$ s (Table 4.2). When applying the lower stress exponent creep law at 910°C (Eq. 4.10 with $A = 4.6\cdot10^{19}$ K·s^{-1} and $n = 2.9$ for $\sigma < 0.6$ MPa), internal stresses $\sigma_0 = 3.5\text{-}3.1$ MPa are obtained. While these values are much higher than those obtained above, they are still reasonable given the approximations made in determining the time of transformation Δt^* and the assumption that the plastic strain is evolving only during that time period, i.e. relaxation of the internal strains occurs quickly.

4.4.3.2 Partial Transformation

Additional considerations must be taken into account to model the partial transformation data in Fig. 4.4. High frequency cycling causes a change of the internal stress because of the smaller effective temperature amplitude to which the sample is subjected, since heat transport to, and from, the sample surface is reduced. The resulting reduction in the thermal driving force for the phase transformation increases the time period Δt^* (Eq. 4.4, as

demonstrated for cycles with $T_u = 910°C$ and $T_u = 940°C$) which would lead to a reduction of the internal stress according to Eq. 4.10. However, the volume mismatch which develops over the time Δt^* is also reduced. Without specific information about the relationship between the kinetics of the internal mismatch decay and the time of transformation at high cycle frequencies, a quantitative determination of the internal stress on the basis of Eq. 4.10 is not possible. In an attempt to quantify transformation superplasticity under rapid cycling conditions, a simple approach is to define, based on Eq. 4.1, an effective mismatch $(\Delta V/V)_{eff}$ and an effective internal stress $\sigma_{0,eff}$:

$$\left(\frac{\Delta V}{V}\right)_{eff} = \frac{1}{2}\cdot\left(\frac{\Delta V}{V} + z\cdot\frac{\Delta V}{V}\right) = \frac{1+z}{2}\cdot\frac{\Delta V}{V}\,, \tag{4.18}$$

$$\sigma_{0,eff} = \frac{1}{2}\cdot\left(\sigma_0 + \frac{\sigma_0}{z}\right) = \frac{1+z}{2\cdot z}\cdot\sigma_0\,, \tag{4.19}$$

where z is the ratio of $d(\Delta\varepsilon_v)/d\sigma$ (the superplastic slope for partial transformation at a frequency ν) and $d(\Delta\varepsilon)/d\sigma$ (the corresponding slope for full transformation). Thus, Eqs. 4.18 and 4.19 are the averages of the extreme cases where the reduction of $d(\Delta\varepsilon)/d\sigma$ is due to either only a change in $\Delta V/V$ or only a change in σ_0. From Fig. 4.4, $z = 3.0\ GPa^{-1}/4.4\ GPa^{-1} = 0.68$, so that $(\Delta V/V)_{eff} = 0.34\%$ (for $\Delta V/V = 0.41\%$) and $\sigma_{0,eff} = 2.0$ MPa (for $\sigma_0 = 1.6$ MPa). Figure 4.10 shows the average effective dimensionless data for partial transformation together with analytical and numerical predictions. The data points are found to fit with the curves defined by n = 1.5-2. Although there is appreciable uncertainty regarding the exact value of the normalized data due to the somewhat arbitrary averaging procedure defined by Eqs. 4.18 and 4.19, the normalized results are significantly distinct from the curve defined by $n = 5$, even when extremes are considered, i.e. either $(\Delta V/V)_{eff} = z\cdot(\Delta V/V)$ with σ_0 or $\sigma_{0,eff} = \sigma_0/z$ with $\Delta V/V$.

Since the phase transformation occurs over a stress range coinciding with the transition between diffusional creep (n = 1) and power-law creep (n = 5.0), the average

transformation superplastic behavior might indeed by described by intermediate stress exponent and pre-exponential factor, as suggested by the fit in Fig. 4.10. Also, intermediate values for n and A conform with the results found for complete transformation (Fig. 4.9), because the normalized transformation superplastic strain is largely insensitive to values of the stress exponent for n = 1.5-5 up to $\delta \approx 0.8$. This is in contrast to the case of a yielding material where the strain increments, at an applied stress of 80% of the yield stress σ_Y are within the non-linear region.

In summary, the partial transformation behavior observed at high cycle frequency can be characterized only qualitatively with the existing data, although the main factors affecting transformation superplasticity have been identified. While the strain per cycle for a given stress is reduced when transformation is incomplete, the average strain rate is increased because of the high cycling frequency. Also, higher applied stresses can be used before significant creep occurs, because the sample temperature is fixed at $T_{\alpha/\beta}$. Thus, high frequency cycling can be used for rapid deformation by transformation superplasticity with large tensile strains, as confirmed by the total strain in excess of 100% accumulated during the parts of the experiment were rapid cycling was used.

4.5 Conclusions

1. Transformation superplasticity was demonstrated for polycrystalline zirconium with an engineering tensile strain of 270% without fracture. Strains per cycle as high as 1.6% and average strain rates of up to $1.3 \cdot 10^{-4}$ s^{-1} where achieved with grain sizes as large as 2 mm.
2. Isothermal creep was measured for α-zirconium at 810°C and for β-zirconium at 910°C between 0.3 and 2 MPa, where deformation occurs by a mixture of diffusional and dislocation creep. A new technique was developed to minimize creep

during thermal cycling outside the phase transformation range by using the transformation enthalpy of over-sized sample heads as a heat buffer.

3. The transformation superplastic slope is $d(\Delta\varepsilon)/d\sigma = 2.2\ GPa^{-1}$ for each α/β- and β/α-transformation, leading to a total value of $2 \cdot d(\Delta\varepsilon)/d\sigma = 4.4\ GPa^{-1}$ for a full thermal cycle. Good agreement was found for the average internal allotropic stress as determined by two independent methods: first by using the measured isothermal creep law and transformation times, second by using the experimentally-determined transformation superplastic slope.
4. A window of cycle frequencies was found where the superplastic slope is independent of the cycling frequency, in agreement with predictions based on the transformation times and the temperature amplitudes.
5. High cycle frequencies reduced the superplasticity linear slope to $2 \cdot d(\Delta\varepsilon)/d\sigma = 3.0\ GPa^{-1}$. This effect is explained by an incomplete gauge transformation resulting in a decrease of the internal mismatch and increase of the internal stress. The stress- and strain-normalized data can be fitted to β-zirconium stress exponents between $n = 1.5$-2, corresponding to experimentally-determined creep values.

Figures of Chapter 4

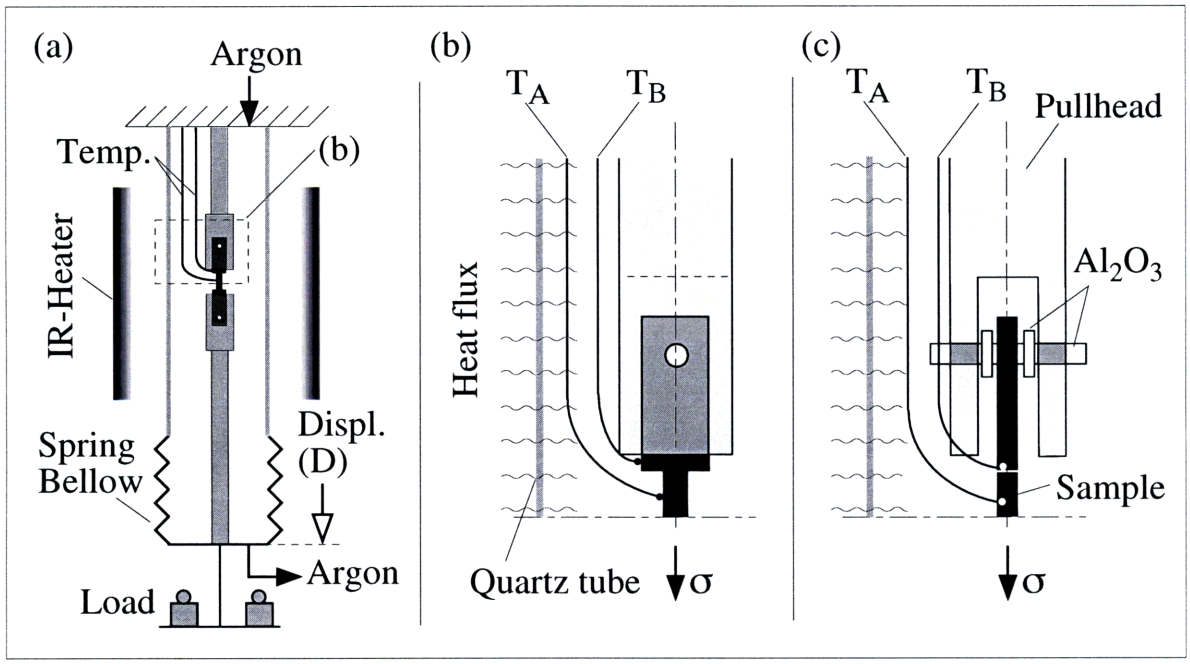

Figure 4.1: (a) Schematic of the experimental setup; (b,c) two detailed orthogonal views.

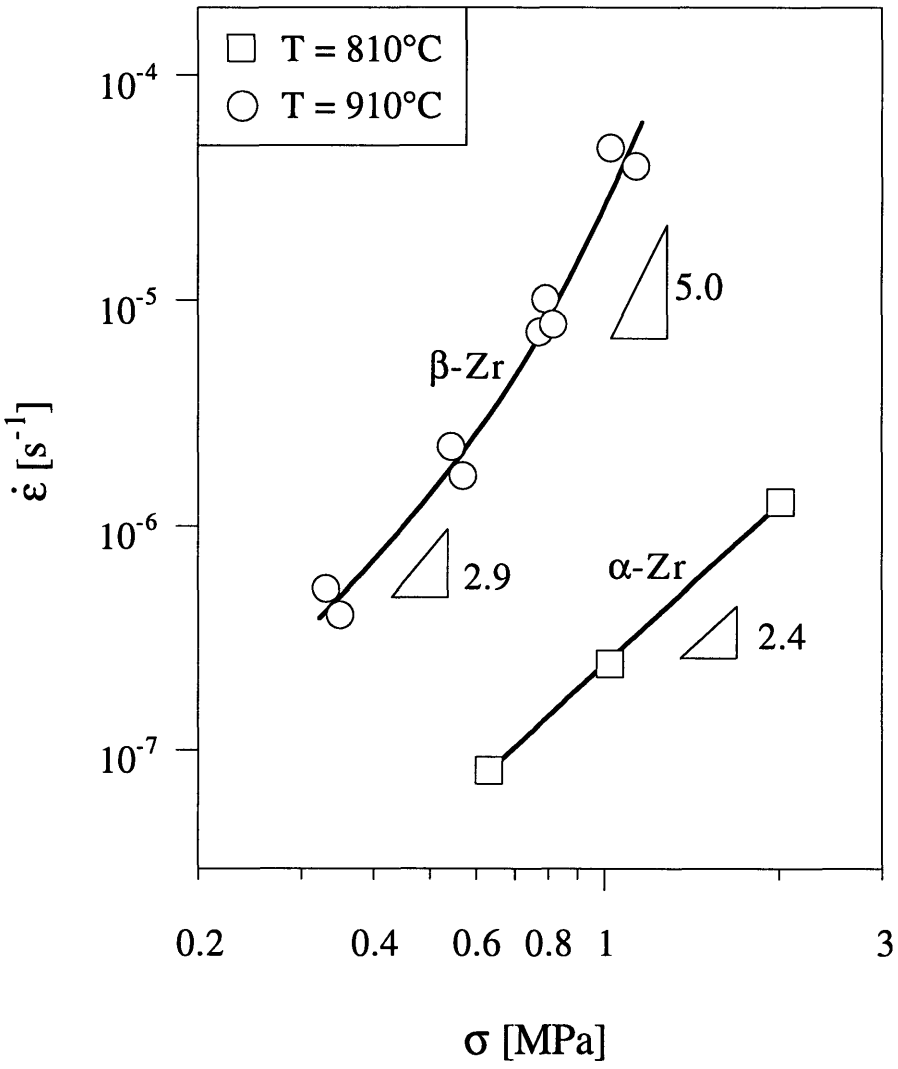

Figure 4.2: Isothermal creep rate as a function of the applied stress for α-zirconium at 810°C and β-zirconium at 910°C.

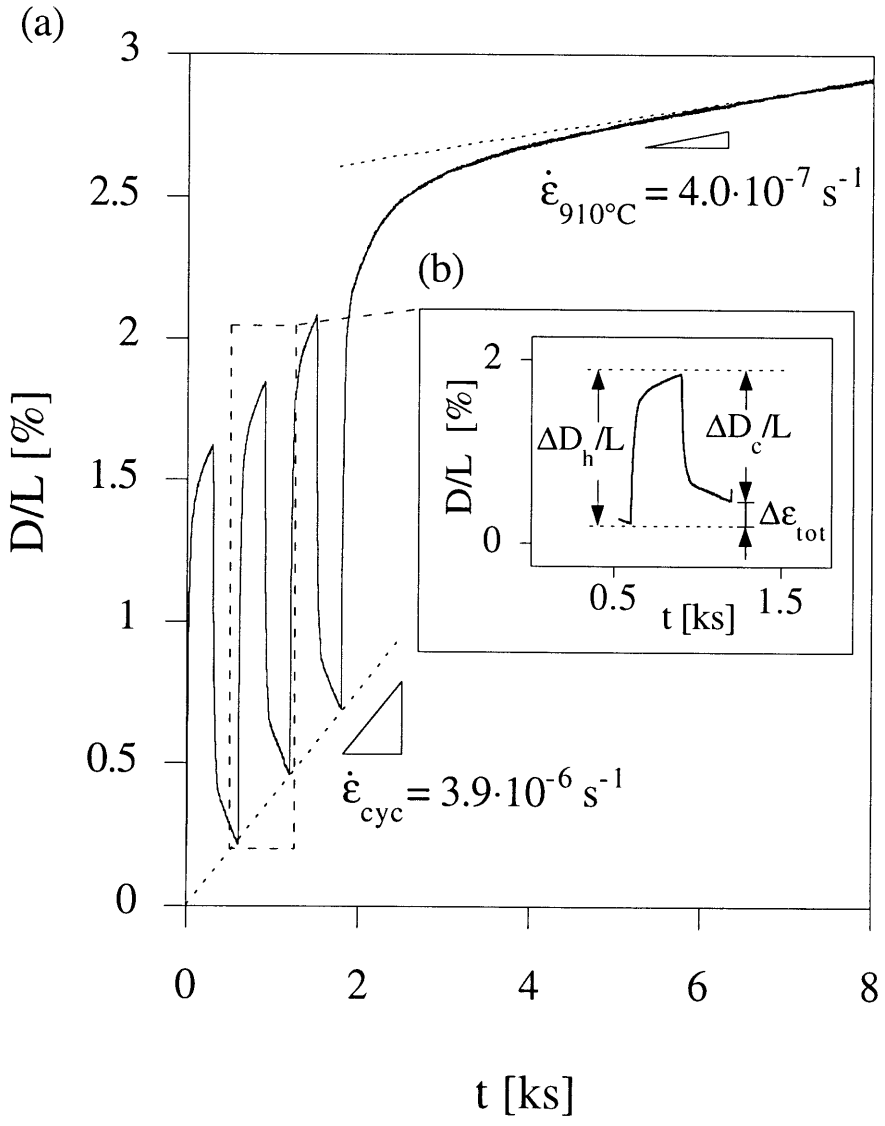

Figure 4.3: (a) Strain as a function of time for cycling between T_l = 810°C and T_u = 910°C with ν = 6 hr^{-1} under constant stress σ = 0.34 MPa. Isothermal creep at T_u = 910°C followed the cycling segment. (b) Single thermal cycle.

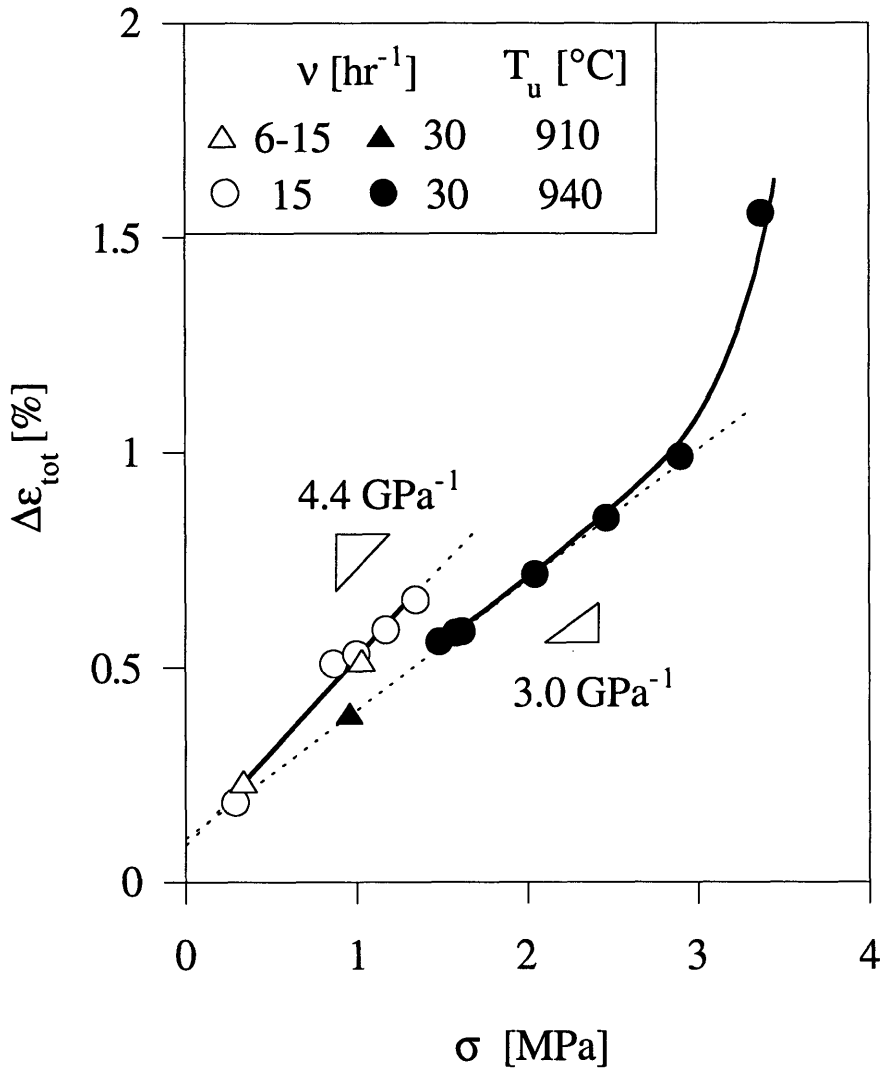

Figure 4.4: Total strain increment per cycle as a function of the applied stress for cycles with $T_l = 810°C$, $T_u = 910\text{-}940°C$ and $\nu = 6\text{-}30\ hr^{-1}$.

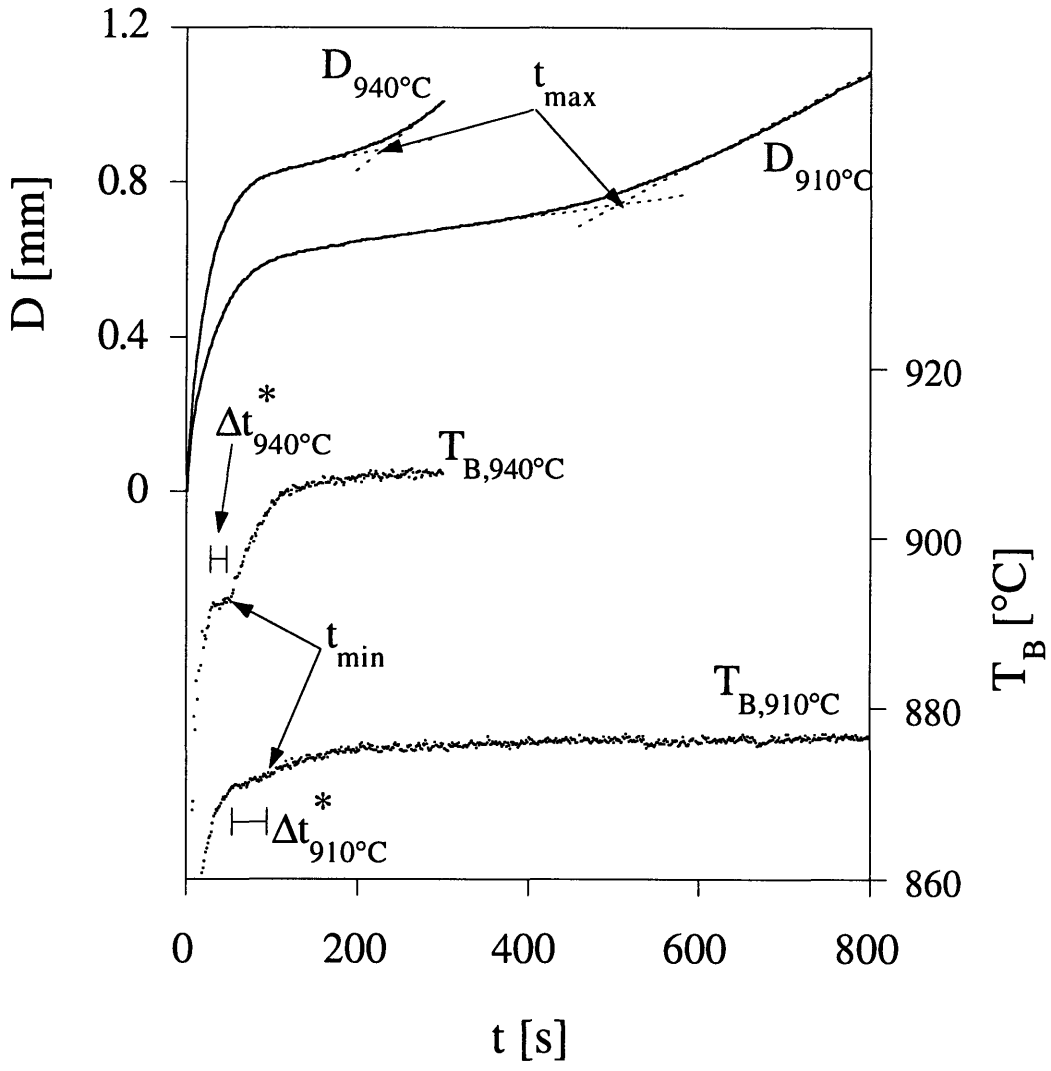

Figure 4.5: Deformation D and temperature T_B as a function of time for heating from T_l = 810°C to T_u = 910°C or T_u = 940°C. The temperature used in index is T_A, the upper cycling temperature applied at the sample gauge section.

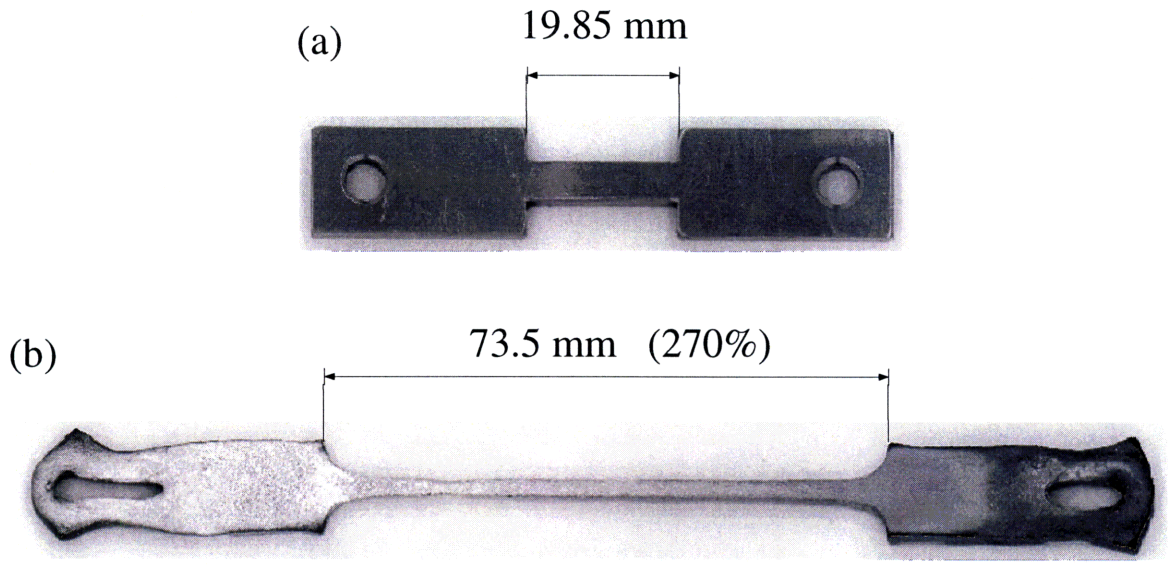

Figure 4.6: Zirconium sample (a) in the undeformed state and (b) at the end of the experiment, after deformation by both transformation superplasticity and isothermal creep at various stresses.

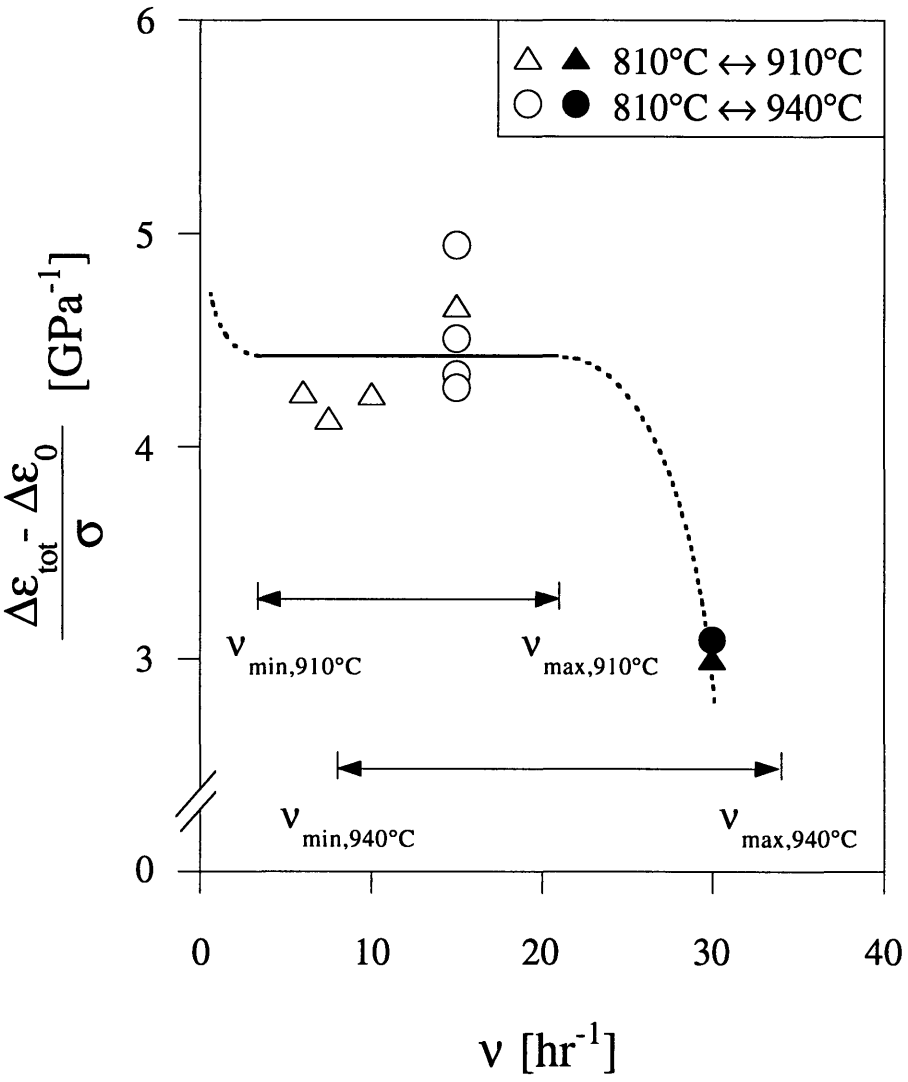

Figure 4.7: Adjusted total strain increment per cycle normalized by the applied stress as a function of the cycling frequency for cycles with T_l = 810°C, T_u = 910-940°C and stresses σ = 0.9-1.6 MPa; The symbols are the same as in Figure 4.4.

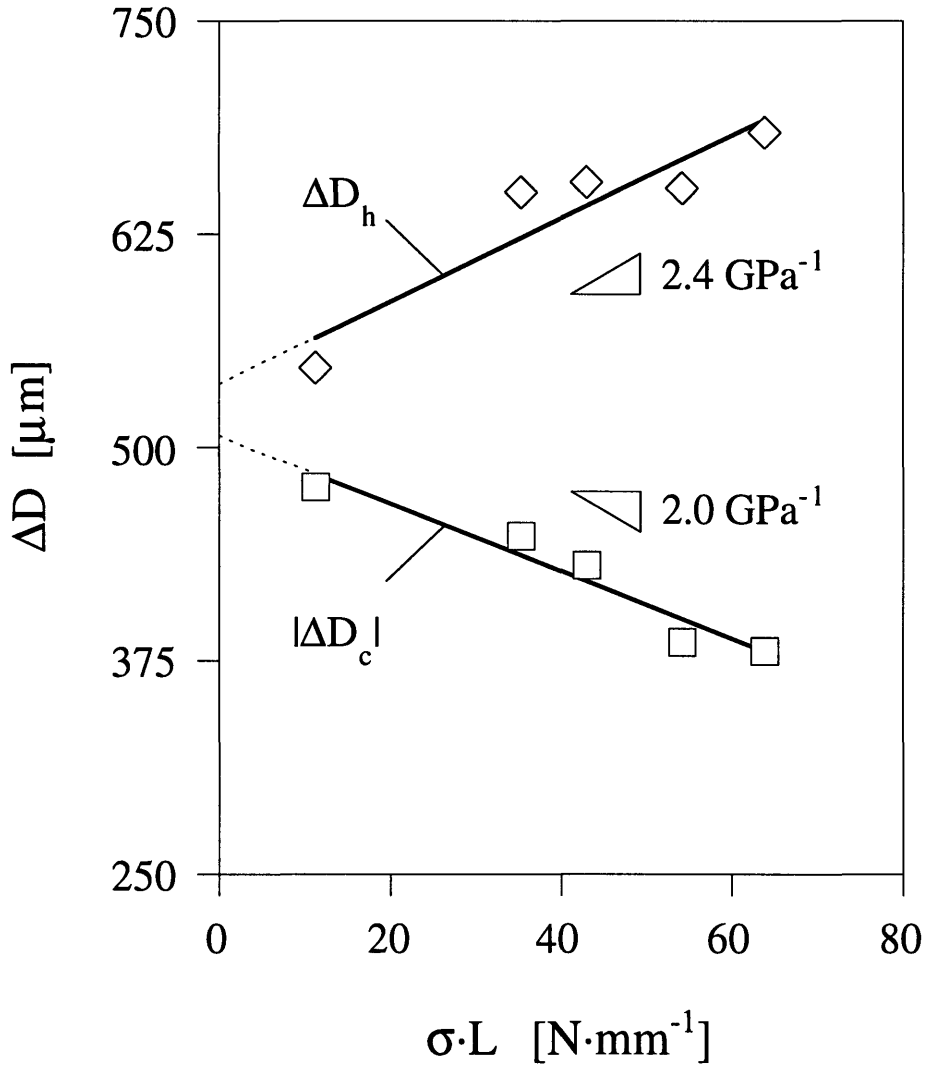

Figure 4.8: Deformation difference of the heating- and cooling part of the temperature cycle (Fig. 4.3b) as a function of the product of the applied stress with the instantaneous sample length for cycles with T_l = 810°C, T_u = 940°C, ν = 15 hr^{-1}, σ = 0.3-1.3 MPa.

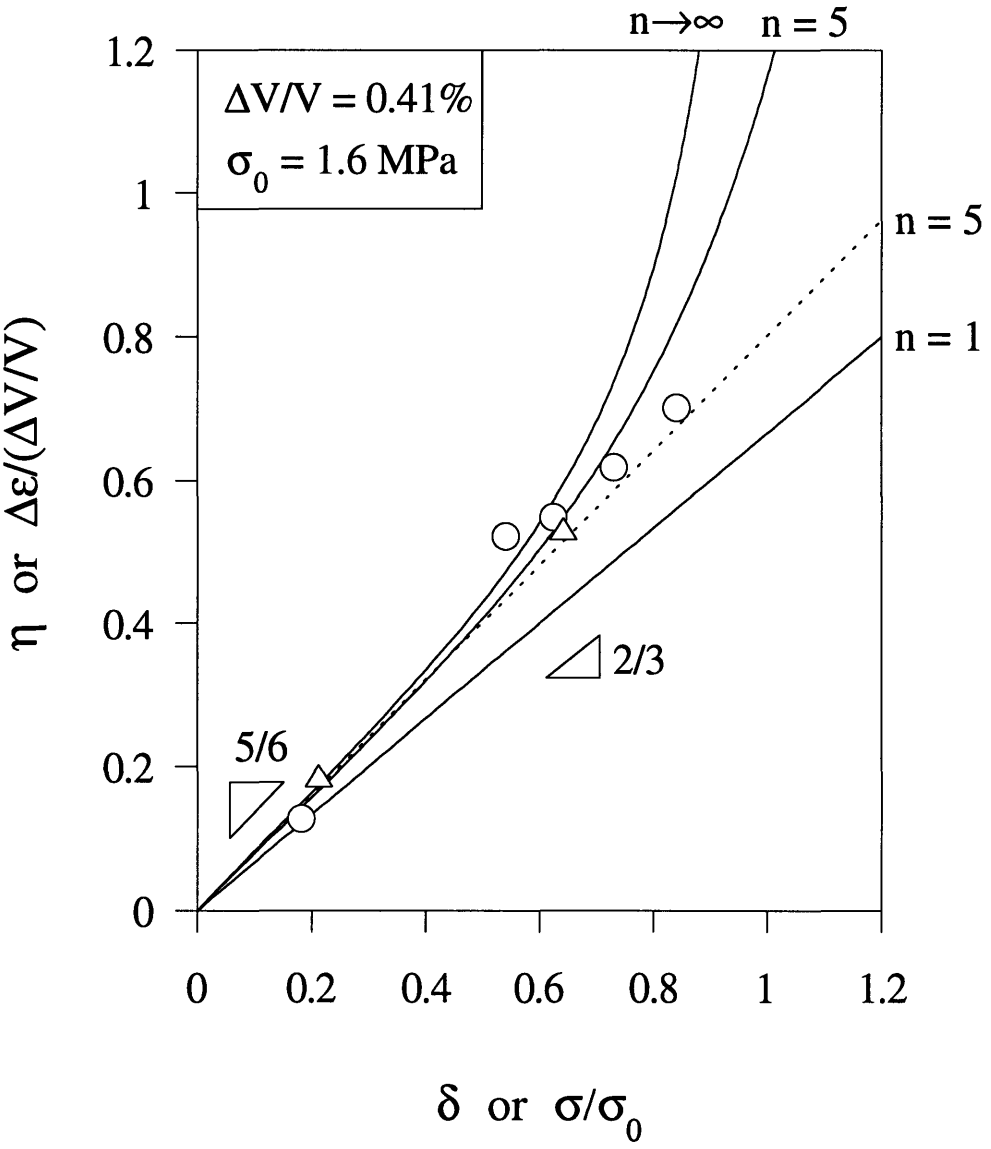

Figure 4.9: Adjusted dimensionless strain increment per transformation as a function of the dimensionless stress. Experimental results for full transformation are compared to model predictions (diffusional creep: $n = 1$ (Eq. 4.14); power-law creep: $n = 5$ (full: Eq. 4.13, dotted: Eq. 4.1); ideally plastic: $n \rightarrow \infty$ (Eq. 4.15)). The symbols are the same as in Figure 4.4.

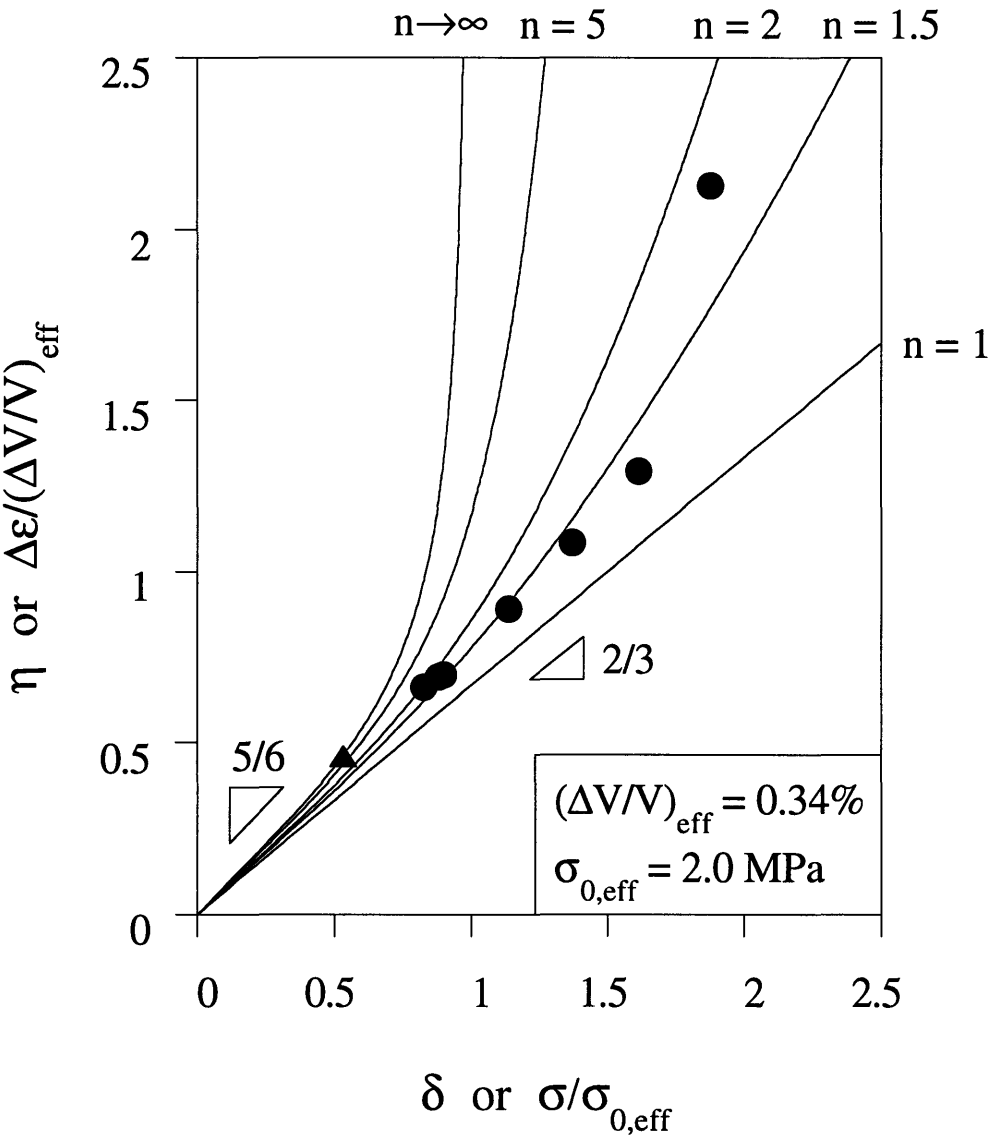

Figure 4.10: Effective adjusted dimensionless strain increment per transformation as a function of the effective dimensionless stress. Experimental results for partial transformation are compared to model predictions (diffusional creep: $n = 1$ (Eq. 4.14); power-law creep: $n = 1.5, 2, 5$ (Eq. 4.13); ideally plastic: $n \rightarrow \infty$ (Eq. 4.15)). The symbols are the same as in Figure 4.4.

Tables of Chapter 4

Table 4.1: Sample chemical composition [ppm]

	C	H	N	O
As-received	< 20	4	< 20	340
After thermal cycling	42	150	40	360

Table 4.2: Transformation times as obtained experimentally (illustrated in Fig. 4.5), and as predicted (Eq. 4.4).

	$\Delta t^*_{910°C}$ [s]		$\Delta t^*_{940°C}$ [s]	
	Fig. 4.5	Eq. 4.4	Fig. 4.5	Eq. 4.4
Heating ($T_s = T_u$)	32.8±3.9	31.3	24.3±3.2	19.5
Cooling ($T_s = T_l$)	34.0±1.2	33.6	34.3±2.6	31.7

Table 4.3: Minimum time t_{min} as obtained from $T_B(t)$ and maximum time t_{max} as obtained from D(t) as illustrated in Fig. 4.5.

	t_{min} [s]		t_{max} [s]	
	$T_A = 910°C$	$T_A = 940°C$	$T_A = 910°C$	$T_A = 940°C$
Heating	85.3±5.1	51.5±2.1	510	225 ± 5
Cooling	44.4±0.9	52.7±0.3	n.d.	n.d.

n.d.: not detectable

Chapter 5

Transformation-Mismatch Plasticity in Intermetallic Matrix Composite

Abstract

A NiAl composite containing 10 vol.% unstabilised zirconia particles was thermally cycled around the allotropic phase transformation range of zirconia while an external uniaxial tensile stress was applied. The strain rates due to thermal cycling are significantly higher than the isothermal creep rates of the composite or the unreinforced matrix. An established model for transformation plasticity of a transforming, creeping material can be adapted to model the phenomenon. To the best of our knowledge, this is the first demonstration of transformation plasticity in an intermetallic system, and the first attempt to induce transformation superplasticity in a composite through transformation of the reinforcement.

5.1 Introduction

Among intermetallics, NiAl stands out as a potential replacement for nickel-based superalloys, because of its low density, large stoichiometric range, high melting point, good thermal conductivity, low material cost and outstanding oxidation resistance [18,57,62]. However, NiAl is brittle at low temperature and creeps rapidly at elevated temperature. Both these problems can be addressed by adding to NiAl a strong ceramic second phase, which increases toughness by debonding and creep resistance by load transfer. Shaping of such composites is however very difficult: casting is limited by the high reactivity of liquid NiAl and its high melting point, while powder-metallurgy techniques usually require a final machining step, which is difficult because of the extreme hardness of the ceramic reinforcement. A possible solution to the problem of shaping NiAl-based composites is to deform these materials superplastically. Microstructural superplasticity requires very fine grains which are difficult to achieve and maintain in NiAl. Transformation superplasticity (TSP), on the other hand, occurs independently of the grain size, but relies on the biasing by an external stress of internal stresses produced during an allotropic phase transformation. Transformation superplasticity has been reported in metals and alloys, as reviewed in [25,29,68]. While NiAl does not exhibit any phase transformation, a suitable allotropic ceramic reinforcement can produce internal stresses in a composite, thus inducing transformation superplasticity in the composite. Unstabilised zirconia is an attractive choice, because it is chemically inert with NiAl, its strength is much higher than NiAl and its allotropic transformation exhibits a large volume mismatch while occurring at temperatures where NiAl deforms easily by creep. Large internal stresses can thus be created by ZrO_2 transforming within a NiAl matrix and these stresses can be relaxed rapidly by creep of NiAl under a biasing stress. Transformation superplasticity in a composite was recently demonstrated by Dunand and Bedell [26] in the Ti/TiC system, where the matrix is allotropic while the reinforcement is inert. The complementary case (i.e., a composite

where the particles undergo a phase transformation while the matrix is inert) is examined in the present chapter, using a technologically-relevant composite system ($NiAl/ZrO_2$). To the best of our knowledge, this is the first demonstration of transformation superplasticity in an intermetallic system, and the first attempt to induce TSP in a composite through transformation of the reinforcement.

5.2 Experimental Procedures and Results

NiAl powders with a particle size of -150+325 mesh (44-100 μm) and a purity of 99.5% (Cerac, Milwaukee, WI) were mixed for 12 hours in a V-Blender with 10 vol.% ZrO_2 powders (Ferro, Cleveland, OH), which had been annealed at 1550°C for 96 hours and screened between 230 and 270 mesh (53-63 μm). The processing of both unreinforced NiAl and the composite was done by cold pressing of the powders into low carbon steel pipes (ASM 5050J, 25.4 mm outside diameter, 3.2 mm wall thickness, 127 mm height), closing the pipes by welding 1018 steel, degassing under vacuum at elevated temperature, and compacting by hot isostatic pressing (UltraClad, Andover MA, 103 MPa, 1163°C, 4 hours). A 100 μm thick molybdenum foil was used between the steel container and the powder to prevent contamination. Flat specimens, as shown in Fig. 5.1b, were machined by diamond grinding. Figure 5.1a shows an etched micrograph of the $NiAl/10\%ZrO_2$ composite after processing, ground with 6 μm and 3 μm diamond paste. Etching was done by using Kallings reagent (5% $CuCl_2 \cdot xH_2O$} in a 1:1 mixture of HCl (conc.) H_2O.

The compact relative density after cold pressing was 59 vol.% for NiAl and 57 vol.% for the composite, as determined by the Archimedes method. The densities after HIPing were 5.92 $g \cdot cm^{-3}$ for the NiAl and 5.87 $g \cdot cm^{-3}$ for the composite. The transformation temperature of the zirconia powder was determined by differential thermal analysis (DTA) (Perkin Elmer, Series 7) under heating and cooling rates $\dot{T}$ =10 $K \cdot min^{-1}$ in air with alumina as reference material (Fig. 5.2a).

Zirconia transforms between a low-temperature monoclinic (m) phase and a denser, high-temperature tetragonal (t) phase in a diffusionless, martensitic reaction exhibiting a significant thermal hysteresis [67,100]. Maiti et. al. [56] reported that the magnitude of undercooling depends on the crystallite size. To stabilize the transformation temperature, the zirconia powder was annealed at 1550°C for 96 hours. Figure 5.2a shows that annealing increased both transformation temperatures by 27 K (from 1066°C to 1093°C on heating and from 925°C to 952°C on cooling), reduced the temperature intervals over which both transformations take place and increased the heat absorbed and released during the phase transformations. However, the thermal hysteresis (141 K) was not affected by the annealing treatment. Dilatometry experiments were performed on a Netzsch 402 ES dilatometer with $\dot{T}$ = 10 $K \cdot min^{-1}$ to determine the transformation temperatures of the zirconia within the composite. Figure 5.2b shows the m/t transformation at 1076°C with a contraction of 0.13% and the t/m transformation at 894°C with an expansion of 0.10%. The zirconia particles show transformation temperatures which are lower in the composite than as free powders: the m/t and t/m transformations are decreased by 17 K and 58 K, respectively. Tensile samples were tested in a custom-designed creep apparatus allowing the application of small tensile stresses with a simultaneous rapid temperature cycling in an argon atmosphere. Before thermal cycling, the samples were crept isothermally until steady-state was reached. The deformation was measured by a linear voltage displacement transducer (LVDT) placed at the cold end of the lower pullrod. Under cycling conditions, the deformation measured by the LVDT included the thermal dilatations of the pullrods and samples and therefore did not represent the sample plastic strain. However, the strain measured under isothermal conditions and over full temperature cycle periods is only due to the sample plastic deformation. The sample stress was adjusted manually by periodically applying or removing weights. The plastic strain increment per cycle, $\Delta\varepsilon_{tot}$, was calculated

as the average of 4 to 6 cycles strains once the strain increments reached steady-state, to avoid the strain contribution due to primary creep.

Figure 5.3 shows the steady-state creep rates as a function of stress for unreinforced NiAl and the NiAl/10%ZrO_2 composite together with the strain rates obtained by thermal cycling of the composite. Thermal cycling was performed between T_l = 700°C and T_u = 1150°C with one minute heating and cooling ramps ($\dot{T}$ = 7.5 $K \cdot s^{-1}$) and one minute hold periods at both extreme temperatures, corresponding to a cycle frequency of 15 hr^{-1}. Figure 5.1c shows the deformed NiAl/10%ZrO_2 sample.

5.3 Discussion

5.3.1 Materials

The measured density of the unreinforced NiAl was 5.92 $g \cdot cm^{-3}$, close to the values reported in the literature (5.90 $g \cdot cm^{-3}$ [62], 5.85 $g \cdot cm^{-3}$ [57]), indicating full densification. Because the zirconia particles were somewhat porous, the density of the composite could not be used to determine its densification. However, the micrograph of the composite (Fig. 5.1a) shows that the material is fully densified. Figure 5.1a also shows that the particles are well distributed within the NiAl matrix with a grain size of approximately 40 μm, well above the typical upper limit of 10 μm for microstructural plasticity to occur.

The observed decrease in transformation temperatures for ZrO_2 within NiAl (Fig. 5.2a vs. Fig. 5.2b) could be due to a constraining effect of the matrix during the phase transformation. As expected, the effect is more pronounced upon cooling where the t/m transformation temperature is lower and thus the matrix is stronger and can exert a larger constraint on the transforming particles. The creep and thermal cycling experiments were conducted until failure, which occurred at the lower sample head as shown in Fig. 5.1c for the composite. The gauge length (originally at 20 mm) increased by 23% while the heads

deformed by 11.4% (over an original length of 17.5 mm). Thus, head deformation contributed significantly to the total plastic deformation measured by the LVDT. However, because the same geometries were used for all specimen, this systematic error affects only the relative position of the strain rate curves. Unreinforced NiAl fractured after 5% strain in the gauge section where fracture occurred at the lower sample head.

5.3.2 Isothermal Creep of NiAl

The stress exponents n = 4.06 at 1100 and n = 3.72 at 1200°C are comparable to results obtained by Vandervoort et. al. [96]. These authors reported stress exponents of 4.4 at 1100°C and 3.8 at 1250°C with an activation energy of 300 kJ·mole^{-1} for cast NiAl deformed in compression at stresses between 6.5 MPa and 43 MPa. By taking an average stress exponent of 3.9, our data can be fitted to a power-law

$$\dot{\varepsilon} = A \cdot \sigma^n \cdot exp\left(-\frac{Q}{R \cdot T}\right), \tag{5.1}$$

with Q = 318 kJ·mole^{-1} and A = 90 (expressing $\dot{\varepsilon}$ in units of s^{-1} and σ in units of MPa). The predicted strain rates are then within a factor 1.4 of the experimental results.

5.3.3 Isothermal Creep and Thermal Cycling of NiAl/10%ZrO_2

The isothermal strain rate of the composite at 1150°C and σ =11.7 MPa was measured as $\dot{\varepsilon}$ = $6.7 \cdot 10^{-7}$ s^{-1}. This value is lower than the creep rate $\dot{\varepsilon}$ = $2.8 \cdot 10^{-6}$ s^{-1} obtained by Eq. 5.1 for unreinforced NiAl, as expected from the strengthening effect of non-creeping particles. The strain rate of the thermally cycled composite as a function of the applied stress (Fig. 5.3) can be fitted to:

$$\Delta\dot{\varepsilon}_{tot} = B \cdot \sigma^n, \tag{5.2}$$

where n = 1.41 and B = $2.35 \cdot 10^{-7}$ ($\dot{\varepsilon}$ in units of s^{-1} and σ in units of MPa). Strain rates between isothermal and cycling experiments can be compared by considering an effective temperature T_{eff} for which the strain rate by power-law creep is the same as the power-law strain rate averaged over a full temperature cycle during the non-isothermal experiments:

$$T_{eff} = -\frac{Q}{R \cdot ln\left(\nu \int exp\left(-\frac{Q}{R \cdot T(t)}\right) dt\right)}, \qquad (5.3)$$

where ν is the cycling frequency. For the temperature history T(t) used in the present cycling experiments, T_{eff} = 1363 K (= 1090°C), so the cycling data in Fig. 5.3 can be, to a good approximation, compared to the isothermal data at 1100°C. It is evident from Fig. 5.3 that the strain rate of NiAl at the equivalent temperature is significantly lower than the strain rate of the composite subjected to thermal cycling. The difference between the isothermally deformed composite and the cycled composite is expected to be even larger, since the composite isothermal creep is slower than that of unreinforced NiAl (Fig. 5.3). Both, the large increase in deformation rate upon cycling and the low cycling stress exponent n = 1.41, are indicative of a material deforming by transformation plasticity. Large tensile elongations, necessary for TSP, can be expected if fracture in the specimen head can be avoided, e.g. by decreasing the stress concentration at the loading pin.

5.3.4 Modeling of Transformation Mismatch Plasticity of NiAl/10%ZrO_2

Figure 5.4a shows the total plastic strain increment per cycle, $\Delta\varepsilon_{tot}$, as a function of the applied stress, σ, on a linear scale. The strain per cycle increases linearly with the applied stress below σ = 10 MPa and non-linearly thereafter. Figure 5.4b shows the deformation histories as measured with the LVDT of two representative cycles, i.e., cycles where the plastic strain increment is constant over 4 to 6 cycles. As depicted in this figure, plastic strain accumulates only during the heating part of the cycle ($\Delta L_{hc} = \Delta L_h$), i.e., during the m/t

transformation at 1076°C. Thus, mismatch stresses produced during the t/m transformation on cooling at 894°C must be accommodate elastically by the NiAl matrix. If no relaxation occurs upon subsequent heating up to the m/t transformation temperature, these elastic stresses are expected to be canceled by that transformation, and transformation plasticity is not expected to be observed. Figure 5.1c however demonstrates that deformation occurs repeatedly upon thermal cycling, and that most of the deformation occurs on heating (Fig. 5.4b). Thus, stored elastic strains produced by the t/m transformation must be released during the heating period before the m/t transformation temperature is reached, possibly resulting in an additional plastic strain contribution. Finally, we note that the dilatometry experiment, performed with much slower cooling rates (factor 45), showed that internal strains could be relaxed during the t/m transformation (Fig. 5.2b) if the observation time is long enough. Because of the high homologous temperature of NiAl at the m/t transformation of ZrO_2 ($T/T_m = 0.71$), at which power-law creep is rapid (Fig. 5.3), we assume that mismatch accommodation in the composite is by matrix creep. Within the linear strain-stress range, Greenwood and Johnson [39] modeled transformation plasticity for a creeping system undergoing a complete allotropic transformation (e.g. titanium):

$$\Delta\varepsilon \approx \frac{2}{3}\cdot\frac{\Delta V}{V}\cdot\frac{\sigma}{\sigma_0}\cdot\frac{5\cdot n}{(4\cdot n+1)}, \tag{5.4}$$

where $\Delta\varepsilon$ is the strain per transformation, σ_0 the internal stress, $\Delta V/V$ the volume mismatch between the two allotropic phases and n the isothermal stress exponent of the weaker phase. In a composite for which only the reinforcement undergoes a phase transformation with a volume mismatch $\Delta V/V$, an equivalent volume mismatch, $(\Delta V/V)_{eq}$ can be defined as:

$$\left(\frac{\Delta V}{V}\right)_{eq} = K_1\cdot G(f)\cdot\frac{\Delta V}{V}, \tag{5.5}$$

where $G(f)$ is a function of the reinforcement volume fraction f and K_1 is a correction parameter taken as unity. Assuming isotropy, the measured dilatometric length mismatch of

the composite, $G(f)\cdot\Delta L/L$ =0.13% is one third the volumetric mismatch $G(f)\cdot\Delta V/V$ = 0.39%. Assuming a volume fraction dependence of $G(f) = f\cdot(1-f)$, where f = 0.1, the volume change of the zirconia is calculated as $\Delta V/V$ = 4.3%, in reasonable agreement with literature data [11,78]. The internal stress is then determined by fitting Eq. 5.4 to the experimental data within the linear range ($\sigma \leq 10$ MPa) substituting $(\Delta V/V)_{eq}$ of Eq. 5.5 for the volume mismatch $\Delta V/V$ in Eq. 5.4, the result of which is shown in Fig. 5.4a. The fitted value σ_0 = 24 MPa is also reasonable when compared to the applied stress range.

5.3.5 Estimation of the expansion-mismatch

Composite mismatch plasticity can also result from the difference between the coefficients of thermal expansion (CTE) of the reinforcement and the matrix [26] The equivalent composite CTE-mismatch is then:

$$\left(\frac{\Delta V}{V}\right)_{eq,cte} = 3\cdot K2\cdot G(f)\cdot\overline{\Delta\alpha}\cdot\left(T_t - T_l\right), \qquad (5.6)$$

where K_2 a correction parameter taken as unity and T_t is the transformation temperature. The CTE of NiAl increases from $16.1\cdot10^{-6}\,K^{-1}$ at 700°C to $17.4\cdot10^{-6}\,K^{-1}$ at 1076°C [16] and the CTE of ZrO_2 climbs from $7.0\cdot10^{-6}\ K^{-1}$ at 700°C to $12.0\cdot10^{-6}\ K^{-1}$ at the m/t transformation temperature [95]. Taking a temperature-averaged mismatch CTE of $\overline{\Delta\alpha}$ = $7.3\cdot10^{-6}\,K^{-1}$, and assuming a volume fraction dependence of $G(f) = f\cdot(1-f)$ with f = 0.1, the equivalent CTE-mismatch is $(\Delta V/V)_{eq,cte}$ = 0.07%. This value is small compared to the equivalent composite transformation mismatch calculated (i.e. 0.39%). More importantly, it is comparable to the elastic strain that are likely to accumulate without significant relaxation [71]. We thus conclude that CTE-mismatch strain can be neglected in the present model.

5.4 Conclusions

A composite consisting of a NiAl matrix reinforced with 10 vol.% zirconia particles was thermally cycled about the allotropic transformation temperature range of zirconia and simultaneously subjected to an uniaxial tensile stress. The strain rates under thermal cycling conditions were much higher than those under equivalent isothermal conditions for either the composite or the unreinforced matrix. While the total elongation was limited by fracture outside the gauge length, the linear relationship between strain per cycle and applied stress indicates that the composite deforms by transformation superplasticity, whereby internal mismatch stresses due to the transformation of the zirconia are biased by the external stress. To the best of our knowledge, this is the first report of transformation superplasticity in an intermetallic system or in any composite system where the reinforcement is allotropic (as opposed to the matrix, as in the Ti/TiC system investigated by Dunand and Bedell [26]). The model by Greenwood and Johnson [39], for transformation superplasticity of a single-phase allotropic material undergoing full transformation under creeping conditions, can be adapted to model the phenomenon by using an effective transformation mismatch strain taking into account the volume fraction of transforming second phase.

Figures of Chapter 5

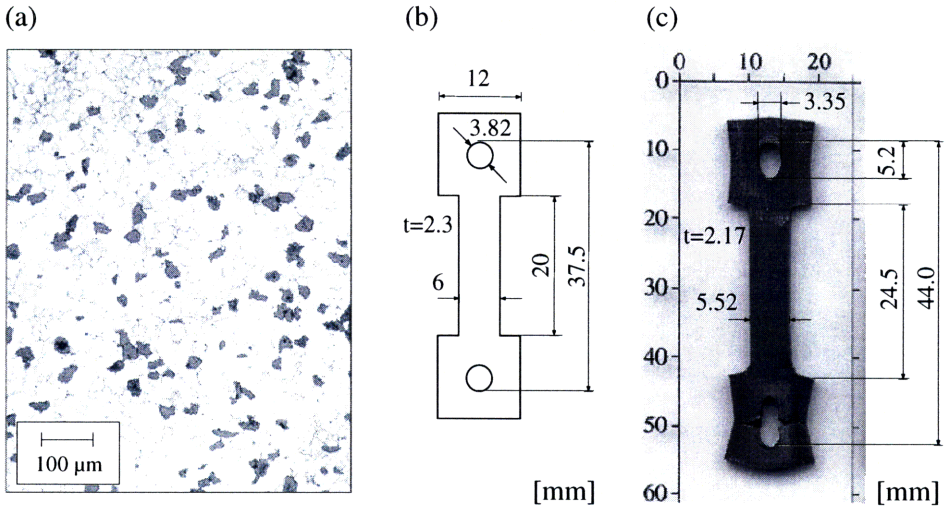

Figure 5.1: (a) Micrograph of the undeformedNiAl/10%ZrO_2 composite showing dark zirconia particles within an etched NiAl matrix; (b) undeformed geometry of tensile sample; (c) macrograph of deformed composite.

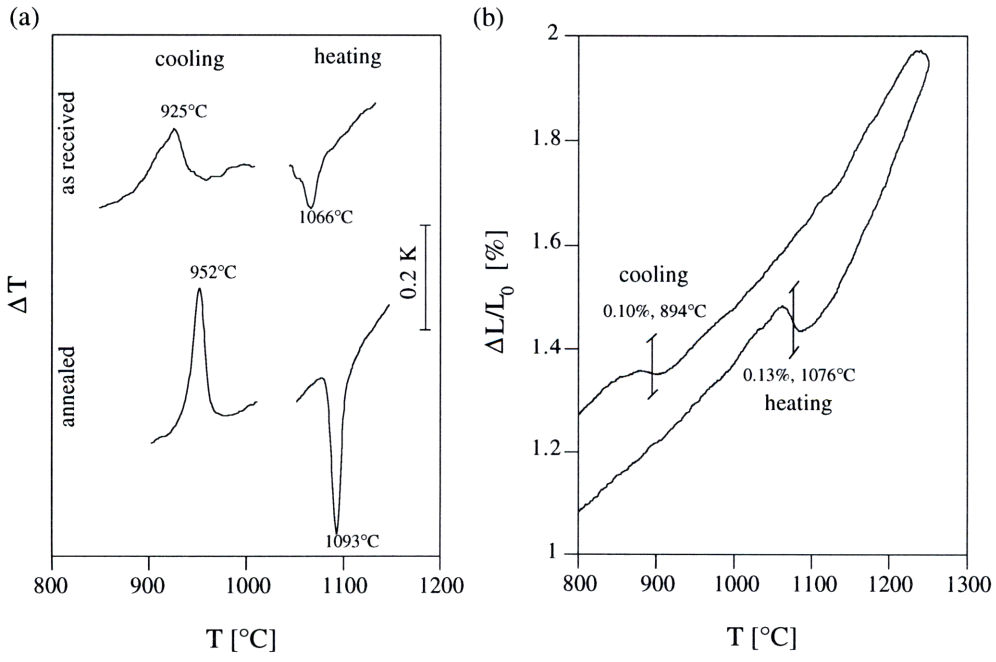

Figure 5.2: (a) Differential Thermal Analysis of the ZrO_2 as received and annealed at 1550°C for 96 hr; (b) Dilatometry of the NiAl/10%ZrO_2 composite.

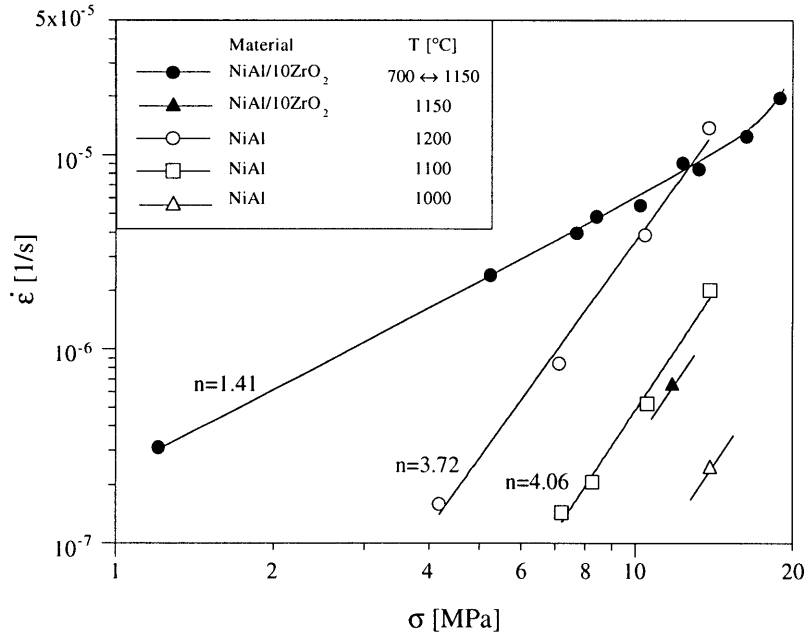

Figure 5.3: Strain rate caused by thermal cycling of NiAl/10%ZrO_2 with ν = 15 hr^{-1}, T_l = 700°C, T_u = 1150°C compared to isothermal creep.

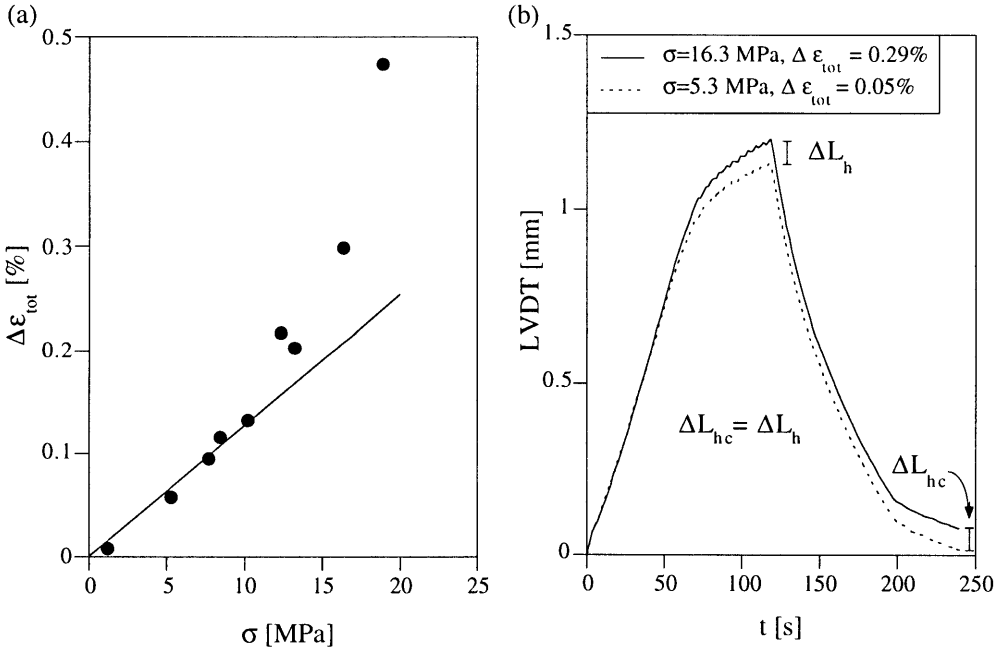

Figure 5.4: (a) Strain increment per cycle as function of the applied stress of NiAl/10%ZrO_2 for cycles with T_l = 700°C, T_u = 1150°C, ν = 15 hr^{-1}; linear model (line); (b) Total deformation of two cycles with two different stresses.

Chapter 6

Finite-Element Modeling of Transformation Superplasticity in Composites with Allotropic Particles

Abstract

A coupled thermal-mechanical finite-element model was developed to describe transformation superplasticity resulting from the biased relaxation of mismatch stresses produced by allotropic particles within a creeping matrix. The case of a NiAl matrix containing 10 vol.% zirconia allotropic particles was explored for a series of externally applied stress values. The instantaneous composite strain developed during the zirconia transformation is found to increase linearly with the applied stress, in agreement with continuum mechanics closed-form models for transformation superplasticity. This instantaneous strain is smaller than the total strain accumulated over a half temperature cycle, indicating that mismatch stresses produced during the transformation relax by matrix creep long after the particles have transformed. Also, the total composite strain after a full temperature cycle is in good agreement with strains determined experimentally on a NiAl/10% ZrO_2 composite. Finally, the internal stress distribution within the transforming composite is determined numerically and compared to simple analytical averages.

6.1 Introduction

When an uniaxial stress is applied on a polycrystalline material displaying internal mismatch stresses caused by an allotropic phase transformation, a strain increment occurs in the direction of the biasing stress. Strains in excess of 100% are obtained upon repeated thermal cycling around the allotropic temperature through accumulation of these strain increments each time a phase change occurs. This phenomenon is called transformation superplasticity and has been experimentally observed in metals (e.g. iron [69], titanium [26,39]), alloys (e.g. steel [35], Ti-6Al-4V [5]) and metal-matrix composites (e.g. Ti/TiC [26], Fe/TiC [108]). The transformation superplastic behavior of materials can be classified according to the accommodation mechanism of the induced internal strains and stresses. At a high homologous temperatures where the material deforms by creep, Greenwood and Johnson [39] derived an analytical expression based on continuum mechanics linking the transformation superplastic strain increment De caused by a phase transformation to the applied stress s:

$$\Delta\varepsilon = \frac{2}{3}\cdot\left|\frac{\Delta V}{V}\right|\cdot\frac{\sigma}{\sigma_0}\cdot\frac{5\cdot n}{(4\cdot n+1)}\ , \qquad (6.1)$$

where $|\Delta V/V|$ is the volume mismatch between the phases, σ_0 the average internal stress of the plastically deforming weaker phase and n the stress exponent of the creep law describing the plastic accommodation. Greenwood and Johnson [39] also modeled the case of ideal plastic yielding at low homologous temperatures where σ_0 in Eq. 6.1 is replaced by the yield stress σ_Y of the weaker phase and n tends to infinity.

Finite-element modeling is ideally suited for the study of transformation superplasticity, since it allows a much more detailed description of the stress- and strain spatial distribution and time evolution during the phase transformation. Zhang et al. [106] studied the related phenomenon of thermal mismatch superplasticity in an Al/SiC composite subjected to thermal cycling. Their plane-strain model assumed an ideally plastic matrix and the

mismatch was approximated by radially shifting nodes at the particle-matrix interface. Ganghoffer et al. [33] modeled in three dimensions transformation plasticity of steel (austenite-pearlite) assuming a yielding, strain-hardening material showing no creep. Levitas [52] also used finite-element modeling to investigate the related problem of plasticity induced by martensite formation in austenite.

In the present chapter, we use a coupled thermal-mechanical finite-element approach to model transformation superplasticity in the NiAl/ZrO_2 system (recently investigated experimentally by Zwigl and Dunand [110]) for which the intermetallic matrix is creeping and the ceramic reinforcement is allotropic.

6.2 Model

6.2.1 Finite Element Model

We used the finite-element code ABAQUS [41] with 4 node, plane-strain, coupled temperature displacement elements (TYPE = CPE4T) arranged in a domain shown in Fig. 3.1. The lower left corner of the mesh is fixed in space and the boundary conditions at the perimeter are set so that the domain remains rectangular. The round zirconia particle is modeled with 45 elements using multiple point constraints for the five elements near the origin while the NiAl matrix is discretisized with 160 elements. A radiative heat flux controlled by the applied temperature profile in the form of a square wave (with a lower temperature T_l and an upper temperature T_u) is entering the domain along the b-b edge while an external stress is applied at the a-a boundary. The final stress state at the end of each transformation (heating or cooling) was used as the initial state for the succeeding run using a user-defined routine to transfer the stresses. To minimize the distortions of the elements caused by repeated transformations, the original undistorted mesh was used as input geometry for each run. The composite strain was calculated as the ratio of the upper a-a

boundary displacement in the y-direction to the length of the domain (arbitrarily set to L_0 = 252 μm).

6.3 Physical Properties

The phase transformation of zirconia is assumed to take place at $T_{m/t}$ = 1076°C on heating and at $T_{m/t}$ = 894°C on cooling within a temperature interval of ±0.5°C, as observed experimentally in Ref. [110]. The density changes from ρ_m = 5.68 g·cm^{-3} for the low-temperature monoclinic (m) phase to ρ_t = 6.10 g·cm^{-3} for the high-temperature tetragonal (t) phase [11]. The corresponding allotropic density change $|\Delta V/V|$ = 7.5% was modeled as a discrete non-linearity of the thermal expansion $|\Delta V/V|$ = 2.5% at the phase transformation temperatures, as shown in Fig. 6.2. The coefficient of thermal expansion (CTE) of monoclinic zirconia increases non-linearly with temperature from $\alpha = 6.92 \cdot 10^{-6}$ K^{-1} at T = 700°C to $\alpha = 12.0 \cdot 10^{-6}$ K^{-1} at T = 1150°C [95]. Since CTE-data of tetragonal zirconia is scarce and contradictory, the CTE of monoclinic zirconia was also used to model the CTE of the tetragonal phase. The specific heat of zirconia is C_p = 0.63 J·g^{-1}·K^{-1} between T = 700°C and T = 1200°C [11] and the thermal conductivity increases from k = 1.7 W·m^{-1}·K^{-1} at T = 100°C to k = 2.1 W·m^{-1}·K^{-1} at T = 1300°C [11]. The elastic modulus of zirconia decreases linearly with temperature according to E[GPa] = 303.8 - 0.108·T[K] [84] and the Poisson's ratio is ν = 0.27 [1]. The heat of transformation is 48 J·g^{-1}[84].

The density of NiAl is ρ = 5.90 g·cm^{-3} [62], the coefficient of thermal expansion is increasing non-linearly from $\alpha = 1.45 \cdot 10^{-5}$ K^{-1} at T = 700°C to $\alpha = 1.55 \cdot 10^{-5}$ K^{-1} at T = 1200°C [62], the elastic modulus decreases according to E[GPa] = 199.8 - 0.04·T[K] [62] while the Poisson's ratio increases slightly from ν = 0.326 at T = 600°C to ν = 0.329 at T = 1300°C [62]. The specific heat increases slightly from C_p = 0.64 J·g^{-1}·K^{-1} at T = 527°C to C_p = 0.68 J·g^{-1}·K^{-1} at T = 727°C [57] and was assumed to remain at C_p = 0.68 J·g^{-1}·K^{-1} up to T = 1200°C. The thermal conductivity decreases non-linearly between T = 600°C and T

= 1200°C from k = 78.6 $W \cdot m^{-1} \cdot K^{-1}$ to k = 73.2 $W \cdot m^{-1} \cdot K^{-1}$ [18]. The creep of polycrystalline NiAl is described by a power-law:

$$\dot{\varepsilon} = A \cdot \exp\left(-\frac{Q}{RT}\right) \cdot \sigma^n \ , \tag{6.2}$$

where A = 90, Q = 318 $kJ \cdot mol^{-1}$, n = 3.9 and σ is expressed in MPa [110]. Absorptivity α and emissivity ε are assumed equal $\alpha = \varepsilon = 0.5$.

6.3.1 Thermal Modeling

6.3.1.1 Radiative Heat Transfer

As for the Biot number for conductive heat transport, a dimensionless number can be defined for radiative heat transfer [37]:

$$M = \frac{\sigma_B \cdot \alpha \cdot T_p^3 \cdot x}{k} \ , \tag{6.3}$$

where σ_B is the Stefan Boltzmann constant, α the absorptivity, T_p the phase transformation temperature and x is the diffusion distance, taken as L_0 for NiAl and R for ZrO_2 (Fig. 3.1). Eq. 6.3 gives M values smaller than 0.01 so that no thermal gradients are expected in the material and ratchetting, i.e. plastic deformation based on macroscopic thermal gradients, can thus be excluded as a deformation mechanism.

Under these conditions, an analytical expression for the temperature history can be obtained from the energy:

$$\rho \cdot C_p \cdot V \cdot \frac{dT}{dt} = -S \cdot \sigma_B \cdot \alpha \cdot (T^4 - T_f^4) \tag{6.4}$$

where V is the volume to be heated and S the surface area for heat transfer. Equation 6.4 is solved for the initial condition $T(t=0) = T_i$ giving:

$$\Delta t_r = \frac{\rho \cdot C_p \cdot V}{4 \cdot S \cdot \sigma_B \cdot \alpha \cdot T_f^3} \left\{ 2 \cdot arctan\left[\frac{T_f \cdot (T - T_i)}{T_f^2 + T \cdot T_i}\right] + ln\left[\frac{(T + T_f) \cdot (T_i - T_f)}{(T - T_f) \cdot (T_i + T_f)}\right] \right\} . \tag{6.5}$$

Equation 6.5 is used to predict the time to heat a material from an initial temperature T_i to a temperature T given an applied surface temperature T_f.

6.3.1.2 Phase Transformation

Under Newtonian conditions the time period Δt_p of the transformation is:

$$\Delta t_p = \frac{V \cdot \rho \cdot \Delta H}{S \cdot \sigma_B \cdot \alpha \cdot (T_f^4 - T_p^4)} , \tag{6.6}$$

where ΔH the enthalpy of transformation. For the numerical model, Eq. 3.7 is used to determine the time for completion of the phase transformation.

6.3.2 Creep Modeling

The general expression for the isothermal steady-state creep rate in the direction 2 (labeled y in Fig. 3.1) is given by [12]:

$$\dot{\varepsilon}_2 = \frac{3}{2} \cdot A \cdot K(T) \cdot \sigma_{eq}^{n-1} \cdot (\sigma_2 - \sigma_v) , \tag{6.7}$$

where K(T) describes the temperature-dependence of the constitutive equation, σ_{eq} the Mises equivalent stress and σ_v the volume average stress. For the case of plane-strain with an uniaxially-applied stress in the 2-direction (Fig. 3.1), the equivalent stress is $\sigma_{eq} = \sigma_2 \cdot (1 - \nu + \nu^2)^{1/2}$, the average stress is $\sigma_v = \sigma_2 \cdot (1+\nu)/3$. By taking $\nu = 0.5$, Eq. 7 reduces to:

$$\dot{\varepsilon}_2(\text{Plane Strain}) = \dot{\varepsilon}_2(\text{Uniaxial}) \cdot \left(\frac{3}{4}\right)^{\frac{n+1}{2}} . \tag{6.8}$$

6.3.3 Numerical Modeling

The numerical model is implemented in three steps: (i) heating from the lower cycle temperature T_l to the phase transformation temperature T_p; (ii) transformation at T_p over a temperature interval of $\Delta T = 1K$; and (iii) heating from T_p to the upper cycling temperature T_u. Equations 6.5 and 3.7 are used to predict the time for the onset and completion of the

phase transformation, where smaller temperature-, strain-, and time increments are used during the coupled temperature-displacement analysis (options DELTMX, CETOL and *CONTROLS, ANALYSIS = DISCONTINUOUS). The same three steps are repeated during the cooling section of the temperature cycle.

6.4 Results

Figure 6.3 shows the temperature history of the heating (3a, 3c) and cooling portions (3b, 3d) of the temperature cycle as measured at the upper left corner of the domain (Fig. 3.1). Upon heating, the temperature increases rapidly until the onset of the phase transformation of the zirconia particle. During the transformation (Fig. 3.c), some of the incoming heat is used for the transformation enthalpy of the particle, thus reducing the average rate of heating. After completion of the transformation, the final temperature increases again rapidly. Conversely, on cooling the heat released by the phase transformation reduces the rate of cooling until completion of the transformation (Fig. 3.d). The temperature difference between the center of the particle and the upper left corner of the matrix is at most $\Delta T = 0.1$ K during the phase transformation, consistent with low M values (Eq. 6.3) predicting low thermal gradients.

Figure 6.4 shows the strain histories of the composite for three different applied stress levels, as determined from the deformation of the upper edge of the domain. The initial elastic response of the composite is E = 187 GPa at T = 700°C, comparing well with E = 161 GPa for NiAl and E = 199 GPa for pure zirconia at that temperature. While the general shape of the curves follows the CTE elongation and contraction due to heating and cooling, the non-linearities at T = 1076°C and T = 894°C are caused by the m/t and t/m phase transformation, respectively. While the thermal expansion and contraction cancel over a full cycle, the strains caused by internal transformation stresses and the externally applied stress cause irreversible plastic deformation over a cycle.

The instantaneous composite strain occurring during zirconia transformation is given by the difference between the maxima and minima of the strain spikes visible in Fig. 6.4. These strains (as well as their sum) are plotted as a function of the applied stress in Fig. 6.5 for the t/m and m/t transformations. Figure 6.5 shows linear stress-strain relations for both the m/t-transformation (with slope, $d(\Delta\varepsilon_{m/t})/d\sigma = 0.053\ GPa^{-1}$) and the t/m transformation (with slope $d(\Delta\varepsilon_{t/m})/d\sigma = 0.015\ GPa^{-1}$) with similar intercepts.

Figure 6.6 shows the creep strain rate as a function of applied stress obtained at a temperature T = 1150°C for NiAl and the NiAl/10%ZrO_2 composite. For NiAl, plane-strain creep was simulated at σ = 10, 20, 40 MPa by using 4x4 plane-strain square elements with the same boundary conditions as in Fig. 3.1. The composite creep rate was determined from the deformation rate at upper cycling temperature T_u = 1150°C just before cooling occurred. Slightly smaller creep rates and stress exponent are observed for the composite as compared to unreinforced NiAl. Figure 6.6 also shows the analytical predictions by Eq. 6.8 which is in excellent agreement with the numerical results for NiAl.

Figure 6.7 shows Mises equivalent matrix stress contour plots before, during, and after the m/t phase transformation. As the zirconia particle shrinks, the maximum matrix equivalent stress found at the particle-matrix interface increases from σ = 68 MPa at the beginning of the transformation (Fig. 6.7c) to σ = 240 MPa at the end of the phase transformation (Fig. 6.7e). Upon subsequent creep (Fig. 6.7f), the matrix stresses relax rapidly and drop to values on the order of the applied stress (σ = 10 MPa). Similar stress distributions are obtained during cooling with higher maximum stresses (up to 800 MPa) because the matrix is stronger at the lower transformation temperature.

6.5 Discussion

The time interval to heat the domain from the initial temperature $T_i = T_l$ = 700°C to the beginning of the phase transformation (T = 1075.5°C), given an applied temperature of T_f =

T_u = 1150°C is estimated by Eq. 6.5 with the properties of NiAl as Δt_{r1} = 7.0 s, which compares well with the value found numerically Δt_{r1} = 7.1 s. Upon cooling from T_u = 1150°C to the t/m phase transformation temperature (T = 894.5°C), Eq. 6.5 predicts Δt_{r2} = 5.2 s, again in good agreement with the numerical result Δt_{r2} = 5.3 s. Furthermore, the time period for the allotropic phase transformation defined by the strain spikes in Fig. 6.4 are found as $\Delta t_{p,m/t}$ = 0.42 s and $\Delta t_{p,t/m}$ = 0.39 s, close to the values of $\Delta t_{p,m/t}$ = 0.32 s and $\Delta t_{p,t/m}$ = 0.26 s predicted by Eq. 3.7 using $V/S = \pi \cdot R^2/(4 \cdot L_0)$, i.e. heat entering along the b-b edge of the matrix is supporting the transformation of the particle (Fig. 3.1). The latter values are expected to be lower than the numerical values because the heat flow through the matrix is neglected.

The consistency of the model is further verified by comparing in Fig. 6.6 isothermal creep rates at T = 1150°C for NiAl obtained analytically (Eq. 6.8) and numerically. First, the slight reduction in the stress exponent for the composite may be due to the thermal history: the composite creep rate is determined at the upper cycling temperature after the phase transformation and may thus include some contribution from the relaxation of the transformation stresses. Second, as expected from load transfer from a creeping matrix to an elastic particle, the composite creeps more slowly than the unreinforced matrix.

Figure 6.5 displays the strain accumulated during the time of the transformation upon heating and upon cooling defined by the spikes in Fig. 6.4 (points c and e in Fig. 6.7a for heating). As expected, the intercepts for zero applied stresses $\Delta\varepsilon_{0,m/t}$ and $\Delta\varepsilon_{0,t/m}$ are the same within numerical error, i.e. the composite expands and contracts reversibly when no external stress is applied. The magnitude of this strain $\Delta\varepsilon_0$ = 0.30% can be compared to the effective volume mismatch in the composite:

$$\left(\frac{\Delta V}{V}\right)_{eff} = f \cdot (1-f) \cdot \left|\frac{\Delta V}{V}\right|, \qquad (6.9)$$

where f is the volume fraction of particles undergoing a phase transformation with volume mismatch $\Delta V/V$. With $f = 0.1$ and $|\Delta V/V| = 7.5$ %, the effective mismatch in the NiAl/ ZrO_2 composites is thus $(\Delta V/V)_{eff} = 0.675\%$. The corresponding uniaxial expansion or contraction are $(\Delta V/V)_{eff}/3 = 0.225$ % for an unconstrained material, and $(\Delta V/V)_{eff}/2 = 0.338$ % for a material fully constrained in one direction. While the strain $\Delta\varepsilon_0 = 0.30\%$ determined numerically under plane-strain conditions is close to the constrained value, the small discrepancy indicates that some elastic strains are stored in the material. In addition, internal stresses are caused by the CTE-mismatch between the particle and the matrix. However, the effect of these internal stresses is negligible because the allotropic mismatch ($(\Delta V/V)_{eff} = 0.675\%$) is much lager than the equivalent volumetric CTE-mismatch, given by $(\Delta V/V)_{eq,CTE} = 3 \cdot f \cdot (1-f) \cdot \overline{\Delta\alpha} \cdot (T_{m/t} - T_l) = 0.08\%$, where the average CTE-difference is $\overline{\Delta\alpha} = 7.7 \cdot 10^{-6}$ K^{-1} and the temperature difference is $T_{m/t} - T_l = 1076°C - 700°C = 376$ K [110].

In Fig. 6.5, the slope of the strain on heating $d(\Delta\varepsilon_{m/t})/d\sigma = 0.053$ GPa^{-1} is larger than on cooling $d(\Delta\varepsilon_{t/m})/d\sigma = 0.015$ GPa^{-1}. This is expected, as the transformation temperature is higher on heating ($T_{m/t} = 1076$ °C) than on cooling ($T_{t/m} = 894$ °C) and thus more elastic strains are stored on cooling, leading to lower plastic strains. Finally, the slope of the total strain per cycle in Fig. 6.5 $d(\Delta\varepsilon)/d\sigma = 0.068$ GPa^{-1} can be compared to the total strain accumulated over a complete cycle $d(\Delta\varepsilon)/d\sigma = 0.13$ GPa^{-1} determined experimentally for a NiAl/10%ZrO_2 composite [110]. Assuming that the plane-strain model accurately describes the transformation in the composite, the discrepancy of a factor of 2 can again be justified with the argument that the superplastic strain does not develop fully during the short interval of time corresponding to the transformation of zirconia, but that stored transformation elastic strains relax under the biasing effect of the external stress during the rest of the cycle.

To test this hypothesis, the total strain accumulated over a full cycle (Fig. 6.4) $\Delta\varepsilon_{tot}$, is compared in Fig. 6.8 to experimental data for a NiAl/10%ZrO_2 composite cycled between T_l

= 700°C and T_u = 1150°C [110]. The match between model and experiment is surprisingly good, especially since the experimental temperature was raised at a finite rate of $|\dot{T}|$ = 7.5 $K \cdot s^{-1}$ between the lower and upper temperatures, so that the experimental temperature profile was not a square wave as in the numerical calculations. However, the model predicts not only the correct slope $d(\Delta\varepsilon_{tot})/d\sigma$ but also the non-linear deviation occurring at high applied stresses, which corresponds to the onset of a significant contribution of creep during the high-temperature section of the cycle.

Within the linear range in Fig. 6.8 ($\sigma \leq 10$ MPa), where high-temperature creep can be neglected, $d(\Delta\varepsilon)/d\sigma$-slopes of the heating and cooling portion of the cycle can be evaluated separately giving $d(\Delta\varepsilon_h)/d\sigma$ = 0.127 GPa^{-1} on heating and $d(\Delta\varepsilon_c)/d\sigma$ = 0.051 GPa^{-1} on cooling. Because $\Delta\varepsilon_h$ and $\Delta\varepsilon_c$ incorporate stress relaxation over a much longer period, the resulting slopes are higher than those obtained from strain spikes (Fig. 6.5). With these slopes and the effective mismatch defined by Eq. (6.9), Eq. (6.1) can be used to determine the average internal stress σ_0 in the NiAl matrix during the transformation, giving values $\sigma_{0,h}$ = 42 MPa and $\sigma_{0,c}$ = 104 MPa for heating and cooling, respectively.

Alternatively, the average internal stress σ_0 can be calculated using the definition by Greenwood and Johnson [39]:

$$\sigma_0^n = \frac{2}{3} \cdot \left| \frac{\Delta V}{V} \right|_{eff} \cdot \left[A \cdot exp\left(-\frac{Q}{R \cdot T} \right) \cdot \Delta t^* \right]^{-1} \qquad (6.10)$$

where Δt^* is the time scale over which the phase transformation occurs. Assuming that internal stress relaxation occurs over the time periods of the m/t and t/m transformation given by the strain spikes (Fig. 6.4) due to the phase transformation, Eq. (11) yields internal stresses $\sigma_{0,m/t}$ = 142 MPa and $\sigma_{0,t/m}$ = 458 MPa. The rather broad ranges of internal stresses given by Eqs. (6.1) and (6.10) (42-142 MPa on heating and 104-458 MPa on cooling) correspond to averages over the whole matrix volume stress and over the complete relaxation occurring at a constant temperature. While they are thus not directly comparable

to the internal stresses determined numerically, Figs. 6.7c-e show that stresses of similar magnitude are found by finite-element modeling.

6.6 Conclusions

Transformation superplasticity (resulting from the biasing by an external stress of internal mismatch stresses produced by an allotropic transformation) was modeled by the finite-element method for a NiAl/10%ZrO_2 composite, where the ceramic reinforcement is allotropic and the intermetallic matrix deforms by creep. The following conclusions can be drawn:

1. The coupled thermal-mechanical formulation captures the temperature history expected for a transforming composite without thermal gradients.
2. Isothermal creep is faster for the unreinforced matrix than for the composite, and is in good agreement with analytical predictions.
3. The composite strain developed during the short interval over which the zirconia transforms is found to increase linearly with the applied stress in qualitative agreement with the analytical expression developed by Greenwood and Johnson [39] for transformation superplasticity. However, the predicted magnitude of the strain is too small by a factor of 2 when compared to experimental data, indicating that some of the elastic mismatch stresses are not relaxed.
4. The total composite strain accumulated over a full cycle increases linearly with stress for low stress values, as expected for transformation superplasticity, but becomes non-linear at high stresses because of the contribution of isothermal creep. The numerical predictions are in excellent agreement with experimental data in both the linear and non-linear regions.

5. The internal matrix stress distribution is determined before, during, and after the phase transformation. Large internal stresses are produced during the phase transformation, in agreement with average values determined analytically.

Figures of Chapter 6

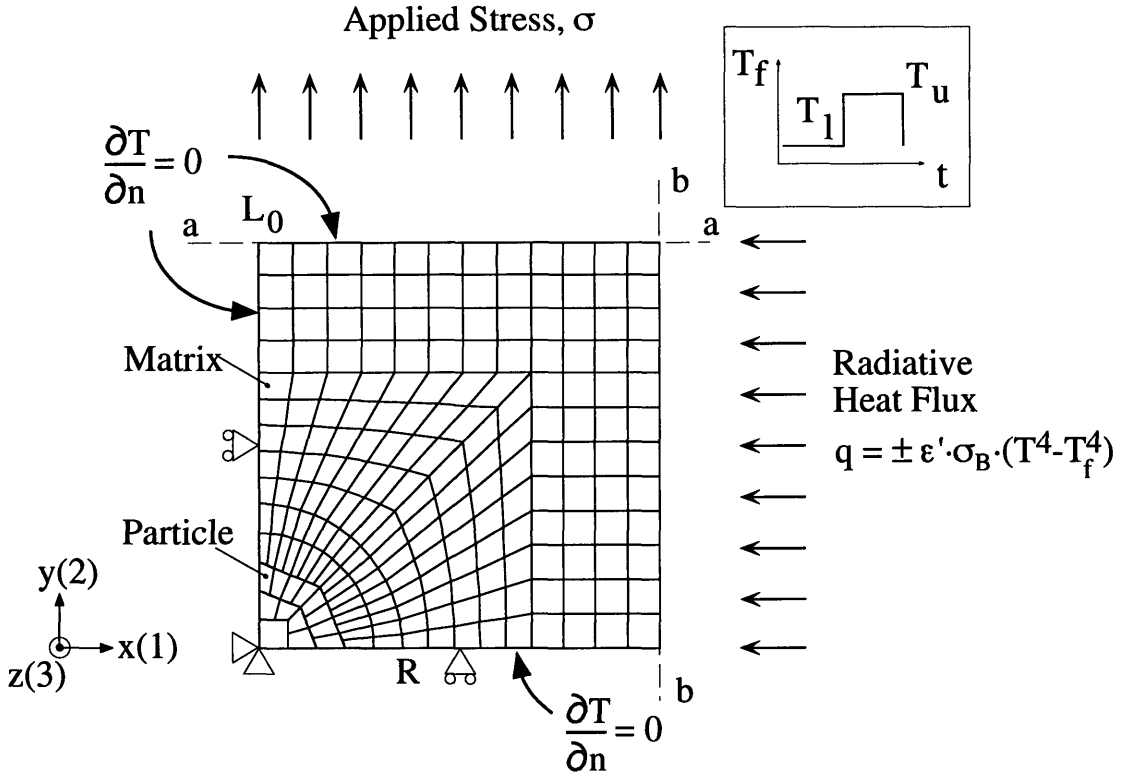

Figure 6.1: Finite-element mesh, boundary conditions, mechanical and thermal loads.

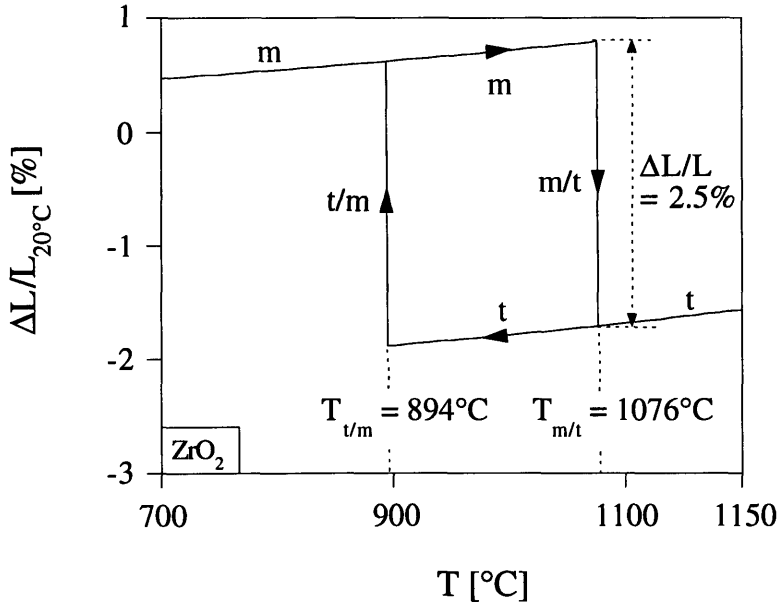

Figure 6.2: Transformation hysteresis of zirconia

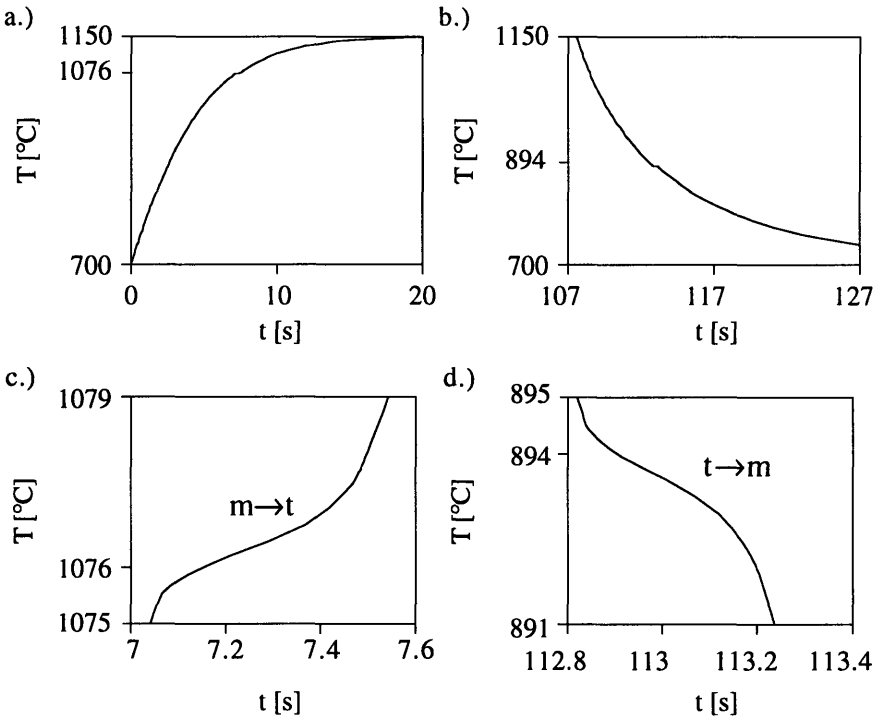

Figure 6.3: Temperature profiles on heating (a) and cooling (b) with detailed views of the m/t (c) and t/m (d) transformation.

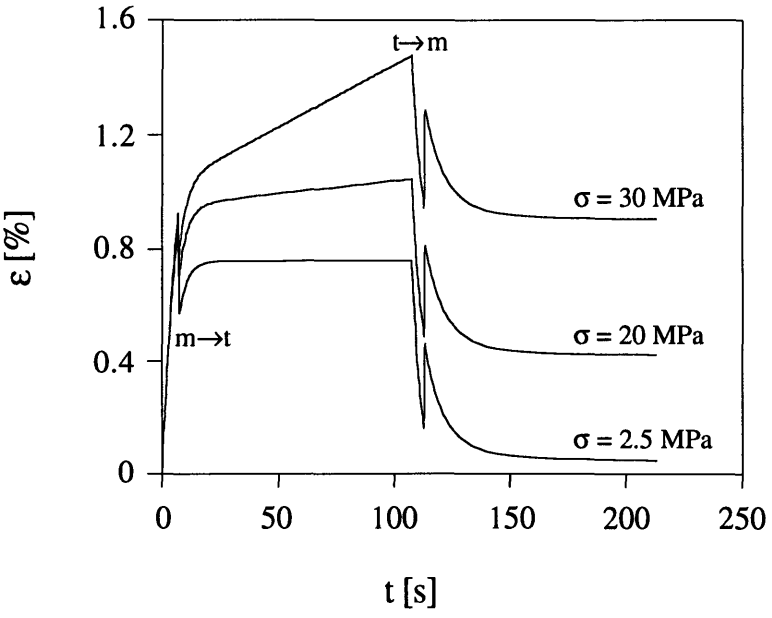

Figure 6.4: Strain histories of NiAl/10ZrO_2 composite at different applied stresses.

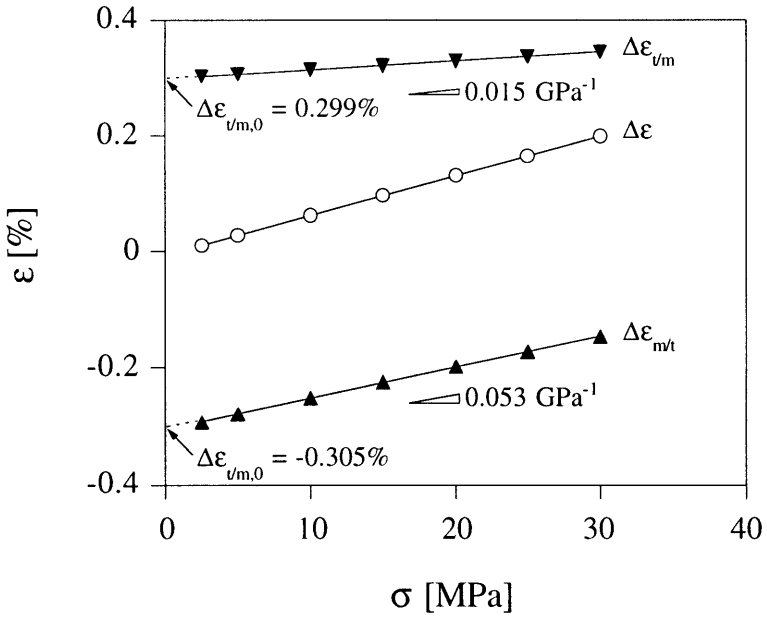

Figure 6.5: Instantaneous composite strain as a function of applied stress for the m/t, t/m and the m/t/m transformations.

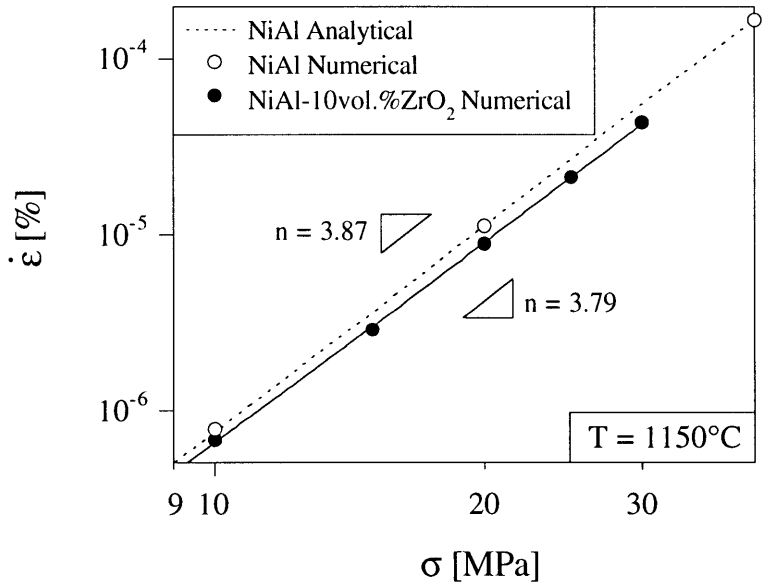

Figure 6.6: Isothermal creep rates of NiAl and NiAl/10%ZrO_2 composite.

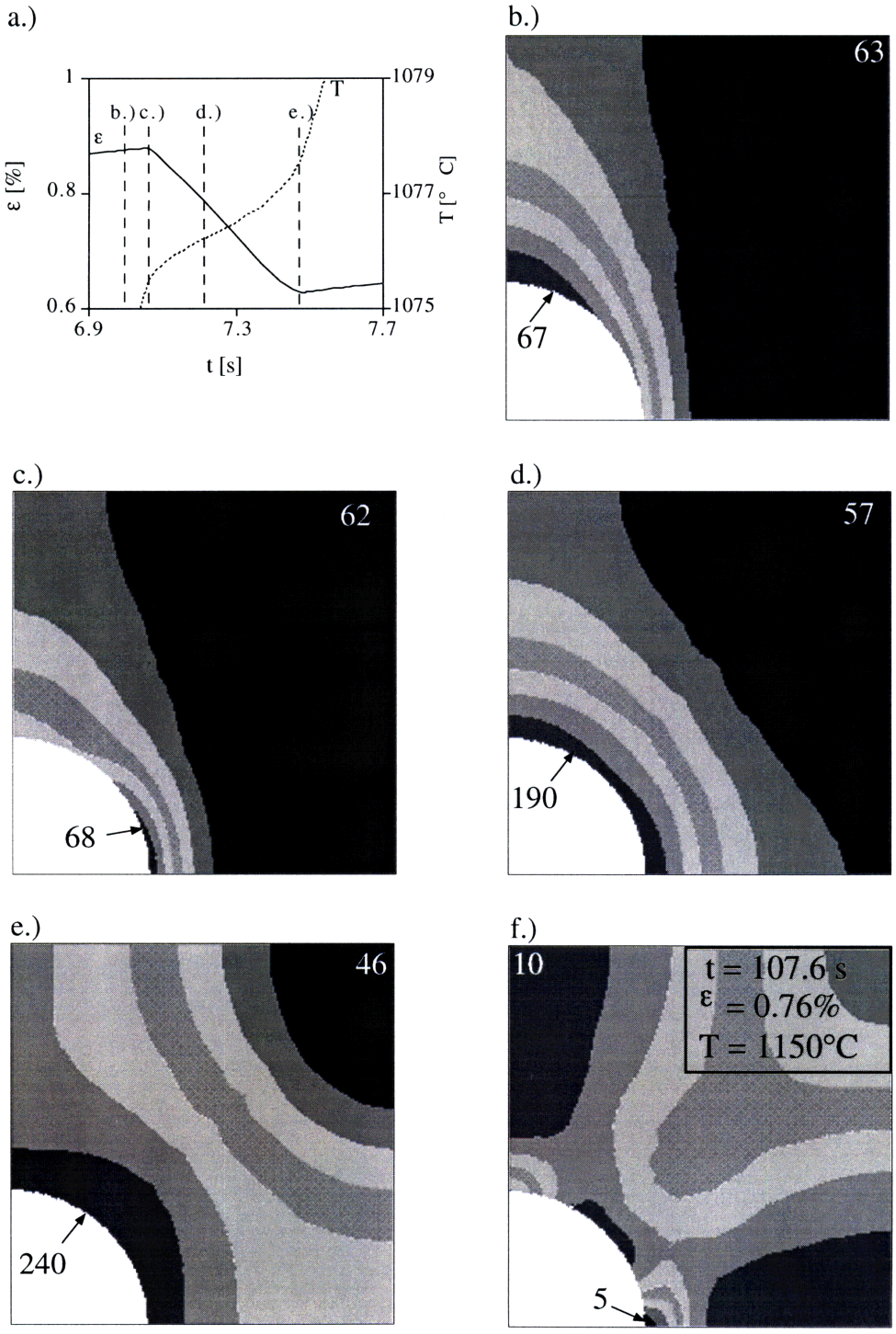

Figure 6.7: Mises equivalent matrix stress contours at different times before, during, and after the m/t transformation with a superimposed external stress of 10 MPa. Gray levels indicate approximately equidistant stress regions; maximum and minimum values are marked in units of MPa.

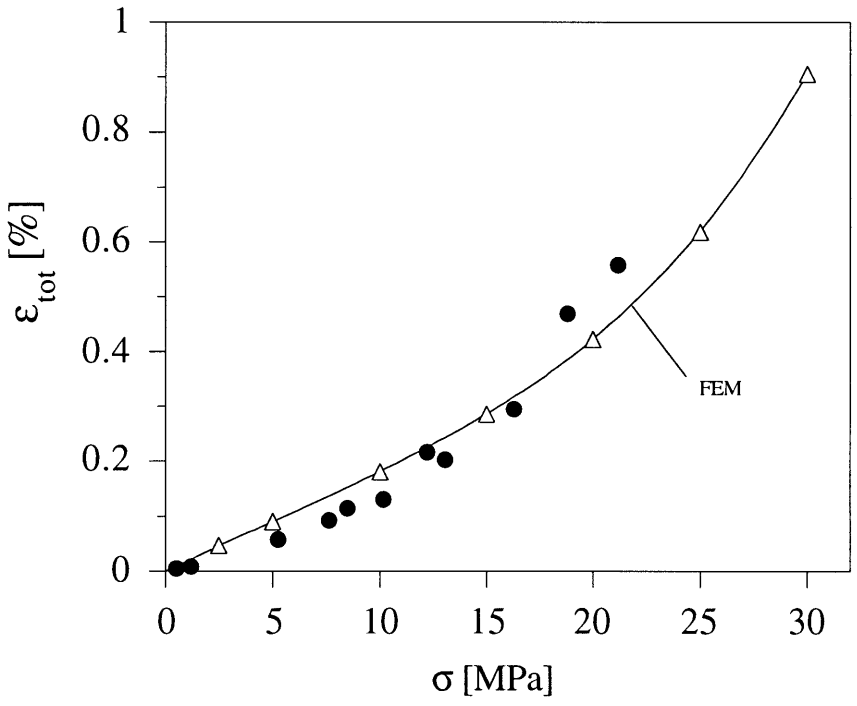

Figure 6.8: Total strain increment per transformation calculated by finite-element (triangles) and experimental data for a NiAl/10%ZrO_2 composite (circles) [110].

Conclusions

The deformation mechanism of transformation superplasticity was studied experimentally and theoretically. New methods and materials have been combined to investigate transformation superplasticity of the pure metals iron and zirconium, and of the metal matrix composites Fe-TiC and NiAl/ZrO_2. The experimental results are related to composition and microstructure and compared to predictions of analytical and numerical models.

The following general conclusions are drawn:

- Transformation superplasticity is a non-linear phenomenon with respect to stress but is independent of grain size. It can be described quantitatively by continuum mechanics closed-form solutions.
- Transformation superplasticity can be modeled numerically for single phase materials and composites. The immediate results show all characteristics of phase transformation superplasticity, thus allowing relative comparison between materials. Furthermore, upon incorporating model-specific assumptions, the numerical results are in quantitative agreement with experimental observations and analytical solutions.
- The thermo-mechanical coupling during the phase transformation can be used to control the time scale and the extend of the phase transformation.
- The magnitude of the strain caused by plastic mechanisms that occur simultaneously with phase transformation superplasticity (i.e. fine-structure superplasticity, thermal mismatch superplasticity, ratchetting, dislocation- and diffusional creep) have to be considered in the evaluation of transformation superplastic experiments.

The following material specific conclusions are drawn:

- Transformation superplasticity of iron is sensitive to traces of carbon. A correlation is found between the carbon and alloy concentration and the transformation superplastic behavior of iron and steels respectively. The superplastic effect within the linear portion of the applied stress vs. strain increment per cycle plot is 1.7 GPa^{-1} for iron containing 0.012% carbon. A total elongation of 450% without fracture demonstrates transformation superplasticity.
- The increase of yield strength due to a slight dissolution of TiC in iron reduces the transformation superplasticity in iron-TiC composites giving 0.37 GPa^{-1} and 0.20 GPa^{-1} for composites containing 10 vol.% and 20 vol.% TiC respectively. Superplastic strain rates of $2 \cdot 10^{-4}$ s^{-1} and fracture strains of 230% are obtained for iron with 10 vol.% TiC.
- Zirconium can be deformed to 270% without fracture and can sustain an average cycling strain rate of $1.3 \cdot 10^{-4}$ s^{-1}. An increased hydrogen concentration does not effect transformation superplastic behavior which was measured as 4.4 GPa^{-1}.
- Nickel aluminide (NiAl) containing 10 vol.% unstabilised zirconia particles shows strain rates upon thermal cycling about the phase transformation hysteresis of zirconia which are significantly higher than the isothermal creep rates of the composite and unreinforced NiAl at the upper cycling temperature. The total transformation superplastic effect is 0.13 GPa^{-1}. A fracture strain of 23% is below the superplastic limit, however the strain rate sensitivity of $m = 0.71$ shows transformation superplastic capabilities.

Bibliography

1. *Engineering Property Data on Selected Ceramics - Single Oxides*, . 1981, Dept. of Def. Inform. Analysis Center.
2. *Metals Handbook: Properties and Selection: Iron, Steels and High Performance Alloys*. Vol. 1. 1990, Metals Park, OH: American Society for Metals.
3. *Metals Handbook: Properties and Selection: Nonferrous Alloys and Pure Metals*. Vol. 2. 1979, Metals Park, OH: American Society for Metals. 826-831.
4. Anderson, R.G. and J.F.W. Bishop. *The Effect of Neutron Irradiation and Thermal Cycling on Permanent Deformations in Uranium under Load*. in *Paper presented at Inst. of Metals Symp. on Uranium and Graphite*. 1962. London.
5. Arzt, E., *Creep of Dispersion Strengthened Materials: A Critical Assessment*. Res Mechanica, 1991. **31**: p. 399-453.
6. Baker, H., *Alloy Phase Diagrams*. ASM Handbook. Vol. 3. 1992, Metals Park, OH: American Society for Metals.
7. Barin, I., *Thermochemical Properties of Inorganic Substances*. 1975, Purdue: Purdue Univ. Press.
8. Basinski, Z.S., W. Hume-Rothery, and A.L. Sutton, *The lattice expansion of iron*. Proc. R. Soc. Lond., 1955. **229**: p. 459-467.
9. Bedell, C.M., *Creep and Thermal Cycling Behavior of Titanium and Titanium/Titanium Carbide Metal Matrix Composites*. M.S. Thesis, Mat. Sci. & Eng. Dept., Massachusetts Institute of Technology: Cambridge, MA. 1993.
10. Bendixen, J. and A. Mortensen, *Particle/Matrix Bonding in Alumina-Steel Composites*. Scripta metall. mater., 1991. **25**: p. 1917-1920.
11. Bever, M.B., ed. *Encyclopedia of Materials Science and Engineering*. . Vol. 7. 1986, Pergamon Press: Oxford. 5543.
12. Boyle, J.T. and J. Spence, *Stress Analysis for Creep*. 1983, London: Butterworths.
13. Brandes, E.A. and G.B. Brook, *Smithells Metals Reference Book*. 7 ed. 1992, Oxford: Butterworth-Heineman. 14-2.
14. Chaix, C. and A. Lasalmonie, *Transformation Induced Plasticity in Titanium*. Res Mechanica, 1981. **2**: p. 241-249.
15. Chen, Y.-C., G.S. Daehn, and R.H. Wagoner, *The Potential for Forming Metal Matrix Composite Components via Thermal Cycling*. Scripta metall., 1990. **24**: p. 2157-2162.

16. Clark, R.W. and J.D. Whittenberger. *Thermal Expansion of Binary CoAl, FeAl and NiAl Alloys*. in *Thermal Expansion 8*. 1981. Gaithersburg: Plenum Press.
17. Clinard, F.W. and O.D. Sherby, *Strength of Iron during Allotropic Transformation.* Acta metall., 1964. **12**: p. 911-919.
18. Darolia, R., *NiAl Alloys for High Temperature Structural Applications.* JOM, 1991. **43**(3): p. 44-49.
19. de Jong, M. and G.W. Rathenau, *Mechanical Properties of an Iron-Carbon Alloy during Allotropic Transformation.* Acta metall., 1961. **9**: p. 714.
20. de Jong, M. and G.W. Rathenau, *Mechanical Properties of Iron and some Iron Alloys while Undergoing Allotropic Transformation.* Acta metall., 1959. **7**: p. 246-253.
21. Denis, S., S. Sjöström, and A. Simon, *Coupled Temperature, Stress, Phase Transformation Calculation Model Numerical Illustration of the Internal Stress Evolution during Cooling of a Eutectoid Carbon Steel Cylinder.* Met. Trans. A, 1987. **18A**: p. 1203-1212.
22. Diani, J.M., H. Sabar, and M. Berveiller, *Micromechanical Modelling of the Transformation Induced Plasticity (TRIP) Phenomenon in Steels.* Int. J. Engng. Sci., 1995. **33**(13): p. 1921-1934.
23. Dieter, G.E., *Mechanical Metallurgy*. 2 ed. 1976, New York: McGraw-Hill Book Company.
24. Dôgan, Ö.N. and J.A. Hawk, *Abrasion Resistance of In Situ Fe-TiC Composites.* Scripta metall. mater., 1995. **33**(6): p. 953-958.
25. Dunand, D.C. *Transformation Superplasticity in Metals, Alloys and Composites*. in *Thermec'97*. 1997. Wollongong: TMS.
26. Dunand, D.C. and C.M. Bedell, *Transformation-Mismatch Superplasticity in Reinforced and Unreinforced Titanium.* Acta metall. mater., 1996. **44**(3): p. 1063-1076.
27. Dunand, D.C. and B. Derby, *Creep and Thermal Cycling*, in *Fundamentals of Metal Matrix Composites*, S. Suresh, A. Mortensen, and A. Needleman, Editors. 1993, Butterworth-Heinemann, Boston MA. p. 191-214.
28. Dunand, D.C. and S. Myojin, *Biaxial Deformation of Ti-6Al-4V and Ti-6Al-4V/TiC Composites by Transformation-Mismatch Superplasticity.* J. Mat. Sci. Eng., 1997. **A230**: p. 25-32.
29. Edington, J.W., K.N. Melton, and C.P. Cutler, *Superplasticity.* Progress Mater. Sci., 1976. **21**(2): p. 61-158.

30. Fischer, F.D., *A Micromechanical Model for Transformation Plasticity in Steels.* Acta metall. mater., 1990. **38**(8): p. 1535-1546.
31. Frost, H.J. and M.F. Ashby, *Deformation-Mechanism Maps: The Plasticity and Creep of Metals and Ceramics.* 1982, New York: Pergamon Press. 60-68.
32. Furushiro, N., H. Kuramoto, Y. Takayama, and S. Hori, *Fundamental Characteristics of the Transformation Superplasticity in a Commercially-pure Titanium.* Trans. ISIJ, 1987. **27**: p. 725-729.
33. Ganghoffer, J.F., S. Denis, E. Gautier, A. Simon, and S. Sjöström, *Finite element calculation of the micromechanics of a diffusional transformation.* Eur. J. Mech., A/Solids, 1993. **12**(1): p. 21-32.
34. Gautier, E. and A. Simon. *Transformation plasticity mechanisms for martensitic transformation of ferrous alloys.* in *Phase Transformations '87.* 1987. Univ. of Cambridge: Inst. Met.
35. Gautier, E., A. Simon, and B. Beck, *Plasticite de Transformation durant la Transformation Perlitique d'un Acier Eutectoide.* Acta metall., 1987. **35**(6): p. 1367-1375.
36. Geiger, D.R. and G.H. Poirier, *Transport Phenomena in Materials Processing.* 1994, Warrandale, PA: TMS. 407.
37. Geiger, G.H. and D.R. Poirier, *Transport Phenomena in Metallurgy.* Addison-Wesley Series in Metallurgy and Materials, ed. M. Cohen. 1973, Reading, MA: Addison-Wesley. pp. 290-304 and 260.
38. González-Doncel, G., S.D. Karmarkar, A.P. Divecha, and O.D. Sherby, *Influence of Anisotropic Distribution of Whiskers on the Superplastic Behavior of Aluminum in a Back Extruded 6061 Al-20% SiCw Composite.* Composites Science and Technology, 1989. **35**: p. 105-120.
39. Greenwood, G.W. and R.H. Johnson, *The Deformation of Metals Under Stress during Phase Transformations.* Proc. R. Soc. Lond., 1965. **283**: p. 403-422.
40. Hart, J.L. and A.C.D. Chaklader, *Superplasticity in pure ZrO_2.* Mater. Res. Bull., 1967. **2**: p. 521-526.
41. Hibbet, Karlsson, and Sorensen, ABAQUS (Version 5.5), Providence RI.
42. Huang, C.Y. and G.S. Daehn, *Densification of Composite Powder Compacts in pressure Cycling.* Acta mater., 1996. **44**: p. 1035-1045.
43. Huang, C.Y. and G.S. Daehn. *Superplastic Forming of Metal Matrix Composites by Thermal and Pressure Cycling.* in *Superplasticity and Superplastic Forming 1995.* 1996: TMS, Warrendale PA.

44. Iguchi, N., Y. Oka, and Y. Saotome, *Transformation Superplasticity in Pure Iron under Rapid Heating.* J. Japn. Inst. Met., 1974. **38**(8): p. 725-730.
45. Iguchi, N., Y. Oka, and Y. Saotome, *Transformation Superplasticity in the Commercial Low Carbon Steel under Rapid Heating.* J. Japn. Inst. Met., 1975. **39**(4): p. 357-361.
46. Johnson, C.A., R.C. Bradt, and J.H. Hoke, *Transformational Plasticity in Bi_2O_3.* Journal of the American Ceramic Society, 1975. **58**: p. 37-40.
47. Johnson, R.H. and G.W. Greenwood, *Deformation of Uranium during Alpha/Beta Cycles under Small Stresses and a Quantitative Interpretation of the Mechanical Weakness of Metals undergoing Phase Transformations.* Nature, 1962. **195**: p. 138.
48. Jouanny-Tresy, C., M. Vardavoulias, and M. Jeandin, *Using Coated Ceramic Particles to Increase Wear Resistance in High-Speed Steels.* 1995. **47**(4): p. 26-30.
49. Kattamis, T.Z. and T. Suganuma, Mater. Sci. Eng., 1990. **A128**: p. 241-252.
50. Kot, R.A. and V. Weiss, *Transformation Plasticity in Iron-Nickel Alloys.* Metall. Trans., 1970. **1**: p. 2685-2693.
51. Lee, D.C., *Part A: The Mechanical Properties of Iron and Steel at Various Temperatures and their Relation to the Thermal Critical Ranges.* Doctor of Science Thesis, Harvard University, 1923. **May 1, 1923**.
52. Levitas, V.I., E. Stein, and A.V. Idesman, *Phase Transitions in Elastic-Plastic Materials: Thermodynamical Theory and Numerical Simulations.* Journal de Physique IV, 1996. **6**: p. C1 309-314.
53. Lide, D.R., ed. *CRC Handbook of Chemistry and Physics.* 76 ed. . 1995, CRC Press: Boca Raton. 4.63-12.172.
54. Lobb, R.C., E.C. Sykes, and R.H. Johnson, *The Superplastic Behavior of Anisotropic Metals Thermally Cycled under Stress.* Metal Science J., 1972. **6**: p. 33-39.
55. Lozinsky, M.G., *Grain Boundary Adsorption and "Superhigh Plasticity".* Acta metall., 1961. **9**: p. 689-694.
56. Maiti, H.S., K.V.G.K. Gorhale, and E.C. Subbarao, *Kinetics and Burst Phenomenon in ZrO_2 Transformation.* Journal of the American Ceramic Society, 1972. **55**: p. 317-322.
57. Miracle, D.B., *The Physical and Mechanical Properties of NiAl.* Acta metall. mater., 1993. **41**: p. 649-684.
58. Mitter, W., *Umwandlungsplastizität und ihre Berücksichtigung bei der Berechnung von Eigenspannungen.* 1987, Berlin: Gebr. Bornträger. 40-44.

59. Myojin, S., *Biaxial Deformation of the Titanium Alloy Ti-6Al-4V by Transformation Superplasticity*. B.S. Thesis, Dept. of Mech. Eng., Massachusetts Institute of Technology: Cambridge, MA. 1995.
60. Nieh, T.J., J. Wadsworth, and O.D. Sherby, *Superplasticity in Metals and Ceramics*. 1997, Cambridge: Cambridge University Press.
61. Nishihara, T., K. Asami, and N. Iguchi, *On the Viscoelastic Behavior under Transformation Superplasticity*. J. Japn. Inst. Met., 1977. **41**: p. 188-193.
62. Noebe, R.D., R.R. Bowman, and M.V. Nathal, *Physical and Mechanical Properties of the B2 Compound NiAl*. International Materials Reviews, 1993. **38**: p. 193-232.
63. Nozaki, H., Y. Uesugi, Y. Nishikawa, and I. Tamura, *Analysis of Phase Transformation Superplasticity by using Continuum Mechanics*. J. Japn. Inst. Met., 1986. **50**(1): p. 56-63.
64. Nozaki, H., Y. Uesugi, Y. Nishikawa, and I. Tamura, *On the Phase-Transformation Superplasticity in Steels due to Temperature Cycling*. J. Japn. Inst. Met., 1985. **49**(4): p. 260-266.
65. Oelschlägel, D. and V. Weiss, *Superplasticity of Steels during the Ferrite <-> Austenite Transformation*. Trans. ASM, 1966. **59**: p. 143-154.
66. Olson, G.B., J. Physique IV, 1996. **6**: p. C1-407-418.
67. Orlans, P., L. Montanaro, J.P. Lecompte, B. Guilhot, and A. Negro. *Physico-Chemical Methods to Control Zirconia Powders*. in *Zirconia '88*. 1988. Bologna, Italy: Elsevier Applied Science.
68. Padmanabhan, K.A. and G.J. Davies, *Superplasticity*. Materials Research and Engineering, ed. B. Ilsschner. Vol. 2. 1980, London: Springer Verlag.
69. Petsche, S. and F. Stangler, *Umwandlungsplastizität (dynamische Superplastizität) bei Eisen*. Z. Metallkde., 1971. **62**(8): p. 601-605.
70. Pickard, S.M. and B. Derby, *The Behaviour of Metal Matrix Composites During Temperature Cycling*. Materials Science and Engineering, 1991. **A135**: p. 213-216.
71. Pickard, S.M. and B. Derby, *The Deformation of Particle Reinforced Metal Matrix Composites During Temperature Cycling*. Acta metall. mater., 1990. **38**(12): p. 2537-2552.
72. Pickard, S.M. and B. Derby, *The Influence of Microstructure on Internal Stress Superplasticity in Polycrystalline Zinc*. Scripta metall., 1991. **25**: p. 467-472.
73. Poirier, J.P., *On Transformation Plasticity*. J. Geophys. Res., 1982. **87**(B8): p. 6791-6797.

74. Porter, L.F. and P.C. Rosenthal, *Effect of Applied Tensile Stress on Phase Transformations in Steel.* Acta metall., 1959. **7**: p. 504-514.
75. Raghunath, C., M.S. Bhat, and P.K. Rohatgi, *In Situ Technique for Synthesizing Fe-TiC Composites.* Scripta metall., 1995. **32**(4): p. 577-582.
76. Rammerstorfer, F.G., F.D. Fischer, H.J. Böhm, and W. Daves, *Computational Micromechanics of Multiphase Materials.* Computers & Structures, 1992. **44**(1/2): p. 453-458.
77. Roberts, A.C. and A.H. Cottrell, *Creep of Alpha Uranium during Irradiation with Neutrons.* Phil. Mag., 1956. **1**: p. 711-717.
78. Rühle, M. and W.M. Kriven. *Analysis of Strain around Tetragonal and Monoclinic Zirconia Inclusions.* in *Solid→Solid Phase Transformations.* 1981. Pittsburgh, PA: Met. Soc. of AIME.
79. Saidi, A., A. Chrysanthou, J.V. Wood, and J.L.F. Kellie, *Characteristics of the Combustion Synthesis of TiC and Fe-TiC Composites.* J. Mat. Sci., 1994. **29**: p. 4993-4998.
80. Sargent, P.M. and M.F. Ashby, *Deformation Maps for Titanium and Zirconium.* Scripta metall., 1982. **16**: p. 1415-1422.
81. Sato, E. and K. Kuribayashi, *A Model of Internal Stress Superplasticity based on Continuum Micromechanics.* Acta metall., 1993. **41**(6): p. 1759-1767.
82. Sauveur, A., *Explanation of Red Shortness When Rolled at Certain Temperatures--New Theories and Hasty Conclusions--Work by Henry M. Howe.* Iron Age, 1924. **113**: p. 581-583.
83. Scheil, E., *Über die Umwandlung des Austenits in Martensite in Eisen-Nickellegierungen unter Belastung.* Z. anorg. u. org. Chem., 1932. **207**: p. 21-40.
84. Shackelford, J. and W. Alexander, *The CRC Materials Science and Engineering Handbook.* 1992, Boca Raton, FL: CRC Press. 268.
85. Sherby, O.D., D.L. Bly, and D.H. Wood. *Plastic Flow and Strength of Uranium and its Alloys.* in *Physical Metallurgy of Uranium Alloys.* 1976. Columbus.
86. Stobo, J.J., *Alpha-Beta Cycling of Uranium.* J. Nuc. Mater., 1960. **2**: p. 97-109.
87. Stringfellow, R.G., D.M. Parks, and G.B. Olson, *A Constitutive Model for Transformation Plasticity Accompanying Strain-Induced Martensitic Transformations in Metastable Austenitic Steels.* Acta metall. mater., 1992. **40**(7): p. 1703-1716.
88. Takayama, Y., N. Furushiro, and S. Hori. *Transformation Superplasticity in a Commercial Pure Titanium.* in *Titanium Science and Technology.* 1985. Munich: Deutsche Gesellschaft für Metallkunde.

89. Taylor, A.K., *Solubility Products for Titanium-, Vanadium-, and Niobium-Carbide in Ferrite.* Scripta metall. mater., 1995. **32**(1): p. 7-12.
90. Terry, B.S. and O.S. Chinyamakobvu, *In Situ Production of Fe-TiC Composites by Reactions in Liquid Iron Alloys.* J. Mat. Sci. Letters, 1991. **10**: p. 628-629.
91. Tiemann, H.P., *Iron and Steel.* 2 ed. 1919, New Yrok: McGraw-Hill. 265.
92. Touloukian, Y.S., ed. *Nonoxides and their Solutions and Mixtures, Including Miscellaneous Ceramic Materials.* Thermophysical Properties of High Temperature Materials. Vol. 5. 1967, The McMillan Company: New York.
93. Touloukian, Y.S., ed. *Thermal Conductivity of Metallic Elements and Alloys.* Thermophysical Properties of High Temperature Materials. Vol. 1. 1970, IFI/Plenum: New York.
94. Touloukian, Y.S., R.K. Kirby, R.E. Taylor, and P.D. Desai, eds. *Thermal Expansion: Metallic Elements and Alloys.* Thermophysical Properties of Matter. Vol. 12. 1975, IFI/Plenum: New York.
95. Touloukian, Y.S., R.K. Kirby, R.E. Taylor, and T.Y.R. Lee, eds. *Thermal Expansion: Nonmetallic Solids.* Thermophysical Properties of Matter. Vol. 13. 1975, IFI/Plenum: New York.
96. Vandervoort, R.R., A.K. Mukherjee, and J.E. Dorn, *Elevated-Temperature Deformation Mechanisms in β'-NiAl.* Trans. ASM, 1966. **59**: p. 931-944.
97. Villars, P., A. Prince, and H. Okamoto, eds. *Handbook of Ternary Alloy Phase Diagrams.* . Vol. 5. 1995, ASM International. 6838.
98. Wassermann, G., *Einfluß der α–γ-Umwandlung eines irreversiblen Nickelstahls auf Kristallorientierung und Zugfestigkeit.* Archiv für das Eisenhüttenwesen, 1933. **6**(8): p. 347-351.
99. Wassermann, G., *Untersuchungen an einer Eisen-Nickel-Legierung über die Verformbarkeit während der γ–α- Umwandlung.* Archiv für das Eisenhüttenwesen, 1937. **10**(7): p. 321-325.
100. Wolten, G.M., *Diffusionless Phase Transformations in Zirconia and Hafnia.* J. Amer. Cerm. Soc., 1963. **46**(9): p. 418-422.
101. Wu, M.Y., J. Wadsworth, and O.D. Sherby, *Internal Stress Superplasticity in Anisotropic Polycrystalline Zinc and Uranium.* Metall. Trans. A, 1987. **18A**: p. 451-462.
102. Yanwen, W., F. Zezhou, and S. Shangchen. *Transformation Superplasticity Solid-State Bonding in Steels.* in *Superplasticity and Superplastic Forming.* 1988: MRS.

103. Young, A.G., K.M. Gardiner, and W.B. Rotsey, *The Plastic Deformation of Alpha-Uranium.* J. Nucl. Mater., 1960. **2**(3): p. 234-246.
104. Zamora, M. and J.P. Poirier, *Experiments in Anisotropic Transformation Plasticity: the case of Cobalt. Geophysical Implications.* Mechanics of Materials, 1983. **2**: p. 193-202.
105. Zhang, H., G.S. Daehn, and R.H. Wagoner, *Simulation of the Plastic Response of Whisker Reinforced Metal Matrix Composites under Thermal Cycling Conditions.* Scripta metall. mater., 1991. **25**: p. 2285-2290.
106. Zhang, H., G.S. Daehn, and R.H. Wagoner, *The Temperature Cycling Deformation of Particle Reinforced Metal Matrix Composites - A Finite Element Study.* Scripta metall. mater., 1990. **24**: p. 2151-2155.
107. This thesis, Chapter 2, p. 45.
Also published as:
Zwigl, P. and D.C. Dunand, *A Non-Linear Model for Internal Stress Superplasticity.* Acta mater., 1997. **45**(12): p. 5285-5294.
108. This thesis, Chapter 1, p. 16.
Also to be published:
Zwigl, P. and D.C. Dunand, *Transformation Superplasticity of Iron and Iron/TiC Metal Matrix Composites.* Met. Mat. Trans. A, in print.
109. Zwigl, P. and D.C. Dunand. *Transformation Superplasticity of Iron: Modeling and Experimental Evidence.* in *Thermec'97.* 1997. Wollongong, Australia: TMS.
110. This thesis, Chapter 5, p. 123.
Also published as:
Zwigl, P. and D.C. Dunand. *Transformation-Mismatch Plasticity in NiAl/ZrO_2 Intermetallic Matrix Composite.* in *Thermec'97.* 1997. Wollongong: TMS.